Plasmonic-based Label-free Detection and Imaging of Molecules

by

Xiaonan Shan

A Dissertation Presented in Partial Fulfillment
of the Requirements for the Degree
Doctor of Philosophy

Approved July 2011 by the
Graduate Supervisory Committee:

Nongjian Tao, Chair
Junseok Chae
Jennifer Blain Christen
Mark Hayes

ARIZONA STATE UNIVERSITY

August 2011

ABSTRACT

Obtaining local electrochemical (EC) information is extremely important for understanding basic surface reactions, and for many applications. Scanning electrochemical microscopy (SECM) can obtain local EC information by scanning a microelectrode across the surface. Although powerful, SECM is slow, the scanning microelectrode may perturb reaction and the measured signal decreases with the size of microelectrode. This thesis demonstrates a new imaging technique based on a principle that is completely different from the conventional EC detection technologies. The technique, referred to as plasmonic-based electrochemical imaging (PECI), images local EC current (both faradaic and non-faradaic) without using a scanning microelectrode. Because PECI response is an optical signal originated from surface plasmon resonance (SPR), PECI is fast and non-invasive and its signal is proportional to incident light intensity, thus does not decrease with the area of interest.

A complete theory is developed in this thesis work to describe the relationship between EC current and PECI signal. EC current imaging at various fixed potentials and local cyclic voltammetry methods are developed and demonstrated with real samples. Fast imaging rate (up to 100,000 frames per second) with $0.2 \times 3\,\mu m$ spatial resolution and 0.3 pA detection limit have been achieved. Several PECI applications have been developed to demonstrate the unique strengths of the new imaging technology. For example, trace particles in fingerprint is detected by PECI, a capability that cannot be achieved with the conventional EC technologies. Another example is PECI imaging of EC reaction

and interfacial impedance of graphene of different thicknesses. In addition, local square wave voltammetry capability is demonstrated and applied to study local catalytic current of platinum nanoparticle microarray.

This thesis also describes a related but different research project that develops a new method to measure surface charge densities of SPR sensor chips, and micro- and nano-particles. A third project of this thesis is to develop a method to expand the conventional SPR detection and imaging technology by including a waveguide mode. This innovation creates a sensitive detection of bulk index of refraction, which overcomes the limitation that the conventional SPR can probe only changes near the sensor surface within ~200 nm.

DEDICATION

To my beloved parents for nurturing and their selfless support.

To my wife for her never-ending love.

ACKNOWLEDGMENTS

First of all, I would like to thank my advisor Dr. Nongjian Tao for his continued guidance, encouragement and support for my past years. Not only did I gain knowledge studying under Dr. Tao, I also learned to find and solve important problems, and always have the big picture in mind.

I would like to thank other committee members, Dr. Junseok Chae, Dr. Jennifer Blain Christen and Dr. Mark Hayes, for their advice and help.

It has been such a valuable experience to work in Dr. Tao's group where I can learn from everyone in the group at anytime. Thanks to Dr. Nguyen Ly for leading me into the SPR field. Thanks to Dr. Erica Forzani and Dr. Shaopeng Wang for the help and good advice on the research. I would like to explicitly thanks Drs Francis Tsow, Kyle Foley, Wei Wang, Ismael Perez-Diez, Josh Hihath, Jilin Xia, Rodrigo.Lglesias, Peter Wiktor, Nagaraj Vinay Janthakahali, Lihua Zhang, Xiaojun Xian and Xiulan Li, as well as Mr. Urmez Patel, Mr. Christopher MacGriff, Mr. Jin Lu, Ms. Rui Wang, Ms. Yan Guan, Mr. Christopher Bruot, Mr. Shaoyin Guo, Mr. Thomas Hines, Mr. Cheng Chen, Mr. Tianle Gao, Mr. Liming Xiang. I will always remember the time working with you.

Thanks to staffs in CSSER for technical support and helpful suggestions.

TABLE OF CONTENTS

Page

CHAPTER Page

CHAPTER Page

CHAPTER Page

LIST OF FIGURES

Figure Page

Figure Page

Figure Page

Figure Page

CHAPTER 1

INTRODUCTION OF SURFACE PLASMON RESONANCE

1.1 Introduction to surface plasmon resonance

Surface plasmon resonance (SPR) is a label-free, real-time and highly sensitive optical surface sensing technique with numerous applications in a variety of disciplines. SPR can be used to probe refractive index changes that occur within the vicinity of a sensor surface. Thus, any physical phenomenon at the surface that alters the refractive index will lead to a response and can be studied.

Over the last two decades, SPR has attracted a great deal of attention. Many research reports have appeared describing advancements in SPR technology and its applications. SPR technology has been commercialized and become a widely accepted tool for characterizing and quantifying biomolecular interactions. Many applications of SPR technique have been developed already, and the list is expanding rapidly.

The rapid development of SPR is because the technology is label free, real time, versatile and highly sensitive, among which label-free detection is the most important advantage of SPR for detecting and studying biomolecular activities. This is because label-based technologies, such as fluorescence detection, is mainly end-point detection, which provides no kinetic information of a binding process, and the use labels may alter the native properties of the molecules.

In the next sections, a brief description of SPR detection and imaging principles is provided.

1.2 Surface plasmons

Surface plasmons are referred to collective oscillations of free or quasi-free electrons excited at the surface of a solid (like metal or semiconductor). The plasmons represent the quanta of the oscillations of surface charges, which are excited by an external electric field, such as light. Typically, the solid material has negatively dielectric constant (real part), and it is either exposed to vacuum or a dielectric material with a positive real dielectric constant. Under appropriate conditions, the surface plasmons can be set to resonate with light, which results in the absorption of light.

For large wave vectors (K_x) the plasmon waves behave like real surface waves, and the associated electromagnetic field is concentrated near the surface within a region of the order of $1/K_x$. For small wave vectors the field is less localized to the surface, and it extends far into space and the plasmon waves resemble more like optical waves propagating along the boundary.

When an external electric field acts on a plasma boundary (one side is semi infinity air, the other side is semi infinity plasma, for example metal), it will produce surface charges like a step function within the screening length of a few Å (Figure 1.1). That is due to the discontinuity of the normal component of the electric field at the boundary between the two media with the dielectric functions ε_0 and ε_1[1]. Because the electric displacement is continuous across the boundary,

while the electric field component perpendicular to the boundary differs if the media differ in permittivity. This will result in the creation of a surface charge density at the boundary and in turn allows for excitation of surface plasmons.[2]

$$\left(\vec{D}_2 - \vec{D}_1\right) \cdot \vec{z} = 4\pi\sigma \qquad (1)$$

In which $\vec{D}$ is the dielectric displacement and σ is the surface charge density. Equation (1) indicates surface plasmons can only be excited at an interface where the dielectric displacement $\vec{D}$ has a component normal to the surface so that it can induce a surface charge density σ.

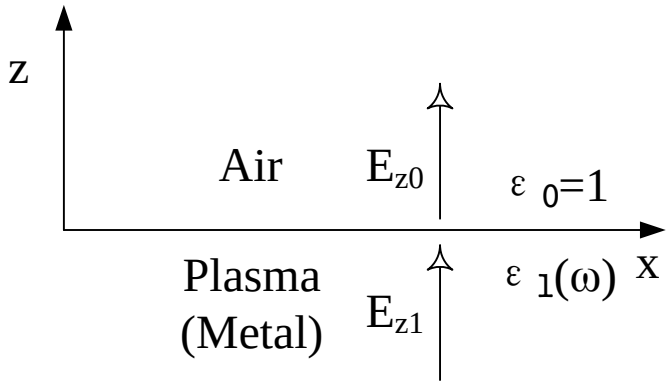

Figure 1.1. The discontinuity of D_z will generate surface charges.

Surface charge density waves are associated with the surface plasmon waves along the surface by

$$\sigma(x,t) = \sigma \exp i(K_x x - \omega t), \quad (2)$$

which is shown in Figure 1.2. The surface wave on a boundary of a semi-infinite plasmon is called a p-polarized wave when the E field oscillates in the (x,z) plane. The surface charge oscillations are localized in the z direction within the Thomas-

Fermi screening length of about 1 Å, and are accompanied by a mixed transversal and longitudinal electromagnetic field. The field is described by[3]

$$E = E_0 \exp\left[+i(k_x x \pm k_z z - \omega t)\right] \qquad (3)$$

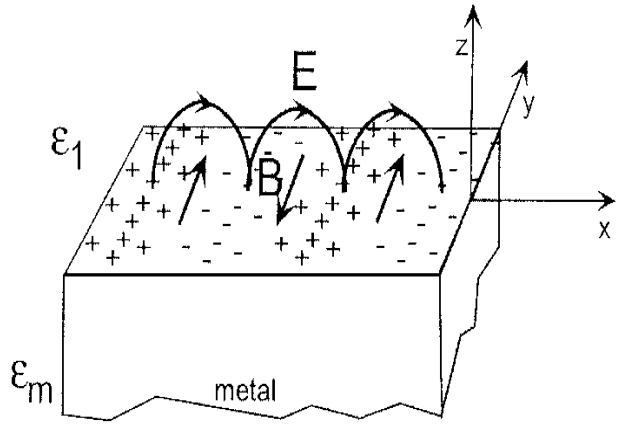

Figure 1.2. Surface plasmon waves and associated surface charge density waves.[2]

1.3 Total internal reflection and evanescent wave

The most popular method to excite surface plasmons is to use light in a total internal reflection mode where evanescent wave can be generated. Newton discovered evanescent wave around four hundred years ago, but a full theoretical description of evanescent wave was not established until the 19th century, when Maxwell's electromagnetic wave theory was developed. Let's consider two dielectric media with refractive indices n_1 and n_2 respectively. A plane wave strikes the boundary between the two media at an angle α, as shown in Figure1.3. Where k_i is the wave vector of incident light, k_r is the wave vector of the reflective light, k_t is the wave vector of refractive light (or transmitting light), and α, β and γ are incident, reflective and refractive angles of light respectively.

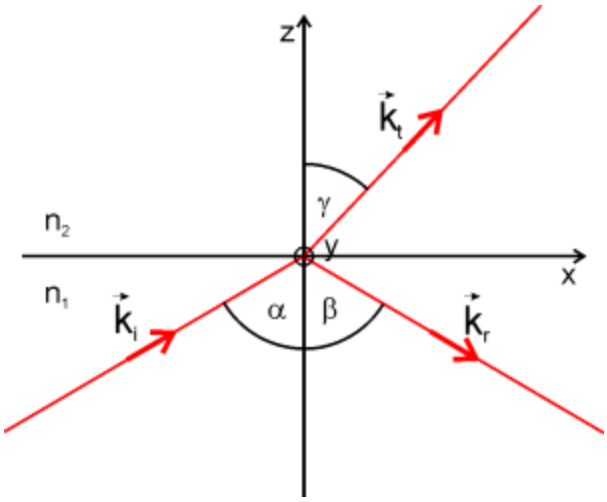

Figure 1.3. Wave vector on the interface. Light is incident on the boundary between two dielectric materials with refractive indices, n_1 and n_2, partially transmitted from medium 1 to medium 2, and partially reflected to medium 1.

By applying boundary conditions one obtains:

$$k_{ix} = k_{rx} = k_{tx} \qquad (4)$$

$$k_i \sin\alpha = k_r \sin\beta = k_t \sin\gamma \qquad (5)$$

$$k_i = \frac{\omega}{c} n_1, \quad k_r = \frac{\omega}{c} n_1, \quad k_t = \frac{\omega}{c} n_2 \qquad (6)$$

where ω and c are the angular frequency and speed of light, and n_1 and n_2 are refractive indices of media 1 and 2. If n_1 is greater than n_2, total internal reflection occurs when the incident angle is increased to a certain value, referred to as critical angle, θ_c.

Based on Snell's law:

$$n_1 \sin\alpha = n_2 \sin\gamma \ , \ (7)$$

from which the angle of refracted light can be determined as

$$\sin\gamma = \frac{n_1}{n_2}\sin\alpha \quad (10)$$

or

$$\cos\gamma = \sqrt{1-\frac{n_1^2}{n_2^2}\sin^2\alpha} \quad . \ (11)$$

It is clear based on Equation 11 when the incident angle, α, reaches the critical angle given by

$$\theta_c = \arcsin(\frac{n_2}{n_1}) \quad (8)$$

all the incident light is reflected. When $\alpha > \theta_c$, $\frac{n_1^2}{n_2^2}\sin^2\alpha$ is greater than 1, and $\cos\gamma$ becomes an imaginary number. In this case, Equation 1 can be rewritten as

$$\cos\gamma = \pm i\sqrt{\frac{n_1^2}{n_2^2}\sin^2\alpha - 1} \quad (12)$$

which leads to evanescent wave.

The refractive wave can be in general written by

$$E_t = E_{0t}e^{i(\vec{K}\cdot\vec{r}-\omega t)} \quad . \ (13)$$

For simplicity, the interface can be assumed lying in the y = 0 plane and thus the y direction is normal to the interface. In this case:

$$\vec{K}_t = (K_{tx}, 0, K_{tz}) = (K_t \sin\gamma, 0, K_t\cos\gamma), \ \vec{r} = (x, 0, z) \quad . \ (14)$$

Consequently the refracted light wave is given by

$$E_t = E_{0t} e^{i(K_t \sin\alpha x - \omega t)} e^{i K_t \cos\alpha z} = E_{0t} e^{i(K_t \sin\alpha x - \omega t)} e^{-\sqrt{(\frac{n_1^2}{n_2^2}\sin^2\alpha - 1)}\cdot z} \quad (15)$$

In Equation 15, term

$$e^{-\sqrt{(\frac{n_1^2}{n_2^2}\sin^2\alpha - 1)}\cdot z} \quad (16)$$

is an exponential decay function, which corresponds to evanescent wave (Figure 1.4).

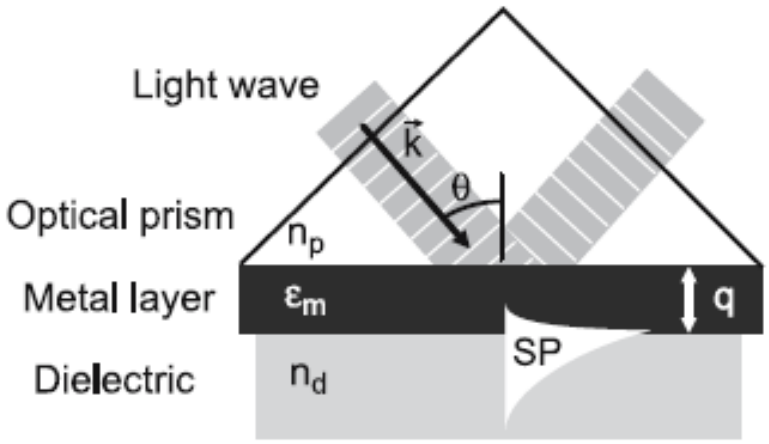

Figure 1.4. Principle of evanescent wave.[4]

1.4 Excitation of surface plasmon

Dispersion relation $\omega(k_x)$:

The eigenfrequency ω of surface Plasmon waves and the wave vector (k_x) in Equation 2 are related by a dispersion relation, $\omega(k_x)$, which can be derived

using Maxwell's equations together with the continuity conditions for D (electrical displacement) and H (magnetic field).

For a thin metal film, which is popular method to create surface plasmons, the dispersion relations are given by

$$K_{x1} = \frac{\omega}{c}\sqrt{\frac{\varepsilon_1\varepsilon_0}{\varepsilon_1+\varepsilon_0}} \quad (17)$$

$$K_{x2} = \frac{\omega}{c}\sqrt{\frac{\varepsilon_1\varepsilon_2}{\varepsilon_1+\varepsilon_2}} \quad (18)$$

These equations describe the conditions at which one can excite the surface plasmons at the metal surface.

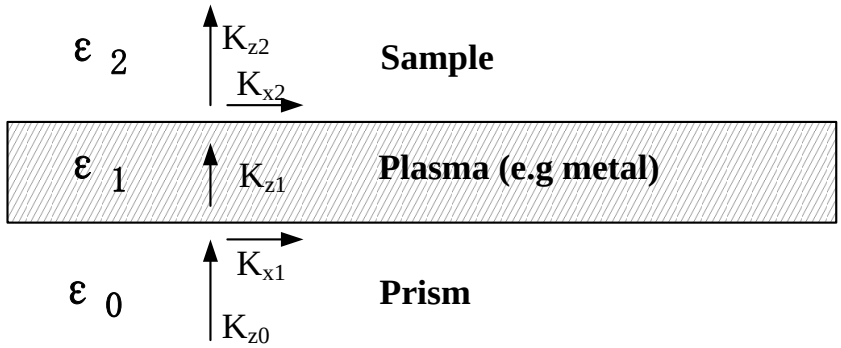

Figure 1.5. Wave vector of surface plasmon.

Basic SPR setup: Kretschmann configuration:

Two well-known optical configurations have been developed for the excitation of surface plasmons. One is the Otto configuration [5] and the other one is the Kretchmann configuration [6], respectively. As the latter one shown in Figure 1.6 is more convenient for most biosensor applications and adapted in most SPR setups, it will be introduced in details.

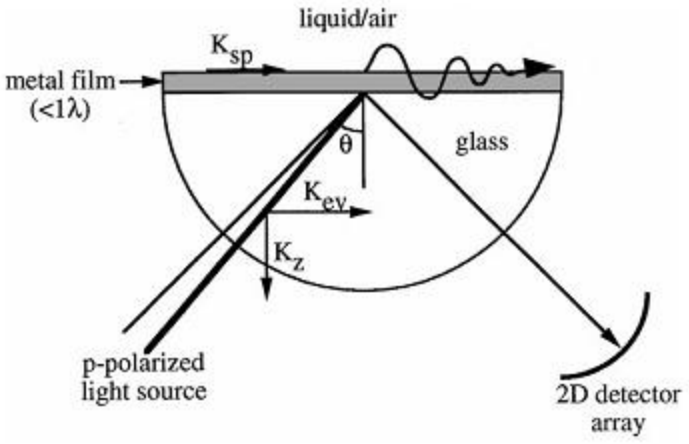

Figure 1.6. Kretchmann configuration.[7]

To excite the surface plasmons p-polarized light is needed because this particular polarization has the electric field vector oscillating normal to the plane that contains the metal film. This is sometimes referred as the transverse magnetic (TM) polarization, in reference to its magnetic field vector orientation. The s-polarized, transverse electric (TE) polarization, cannot couple into the plasmon mode since its electric field vector is oriented parallel to the metal film. This is quite useful because it can be used as a reference beam since it undergoes simple reflection only at the metal surface.

In Kretchmann configuration (Figure 1.6), p-polarized light passes through a prism and incident on the interface between the prism and a sensor chip, made of a glass slide coated with a thin metal film (Figure 1.5). The thickness of metal film has to be smaller than the wavelength, so that the evanescent wave generate by the incident light can reach the metal/sample interface (plasma boundary). The Kretchmann configuration (Figure 1.6) relies on total internal reflection as

elaborated earlier. The intensity of the reflected light can be detected and imaged by a two dimensional array of photodiodes or charge coupled detectors (CCD).

Excitation of SPR: (Wave vector matching)

When the incident angle is bigger than critical angle, although incident light is totally internally reflected, a component of this light, which is called evanescent wave, will generate and penetrates into the less dense medium. The evanescent wave will travel along the surface, which is expressed in Eq.(15). The wave vector of the evanescent field along the x direction is given by combining Eq.(14) and Eq.(5):

$$K_{ev} = K_i \sin\theta = \frac{\omega_0}{c} n_g \sin\theta \quad (19)$$

Where K_i is the wave vector of incident light, ω_0 is the frequency of incident light, n_g is the refractive index of the dense medium (glass), θ is the angle of incidence of the light. From the Eq.(18), the wave vector of a surface plasmon (K_{sp}) can be expressed as

$$K_{sp} = \frac{\omega_0}{c} \sqrt{\frac{\varepsilon_m \varepsilon_s}{\varepsilon_m + \varepsilon_s}} \quad (20)$$

Where ε_m is the dielectric constant of the metal film and ε_s is the dielectric constant of sample.

The evanescent wave of incoming light is able to couple with the free oscillating electrons (plasmons) in the metal film at a specific angle of incidence when $K_{sp} = K_{ev}$, then the condition at which angle surface plasmon resonance will be excited can be obtained:

$$\sin(\theta_R) = \sqrt{\frac{\varepsilon_m \varepsilon_s}{(\varepsilon_m + \varepsilon_s)\varepsilon_g}} \qquad (21)$$

where θ_R is the angle to excite the surface plasmon resonance in Kretschmann configuration.

This excitation is known as wave vector matching. This causes energy from the incident light to be lost to the metal film resulting in a reduction in the intensity of reflected light. SPR cannot be achieved by direct illumination of a suitable support surface with light. Wave vector matching does not occur in this situation because the light wave vector is always smaller than the wave vector that describes the surface plasmon (SP). The prism is used to increase the light wave vector so that wave vector matching is possible.

1.5 SPR response at different refractive index

The surface plasmon is affected by changes in the dielectric permittivity of materials in contact with the metal film. The dielectric permittivity, ε, is a dimensionless quantity that is proportional to the square of the refractive index of the sample. As the refractive index of sample region changes, it will alter the coupling efficiency of the light into the plasmon mode, which can be monitored by observing the SP coupling angle, θ_R, the incident beam angle giving maximum SP coupling.

If the angle of incidence for the light beam is scanned throughout a range of values, a distinct minimum in reflectivity will be observed at a discrete angle (Figure 1.7). At this particular angle of incidence, for a given set of dielectric values and the reflection from the metal film is most attenuated. Sensing is carried

out by relating θ_R changes to the refractive index of the sample. As shown in Figure 1.7, a computer program, Winspall, is used in calculating the SPR curves. The simulation structure is a three layers system, which has prism on the bottom, a thin gold layer (47nm) on top of prism and sample is above the gold. When the refractive index of sample region changes from 1.33 to 1.35, the coupling angle θ_R will shift. By measuring the shifts of the coupling angle, the refractive index change can be known.

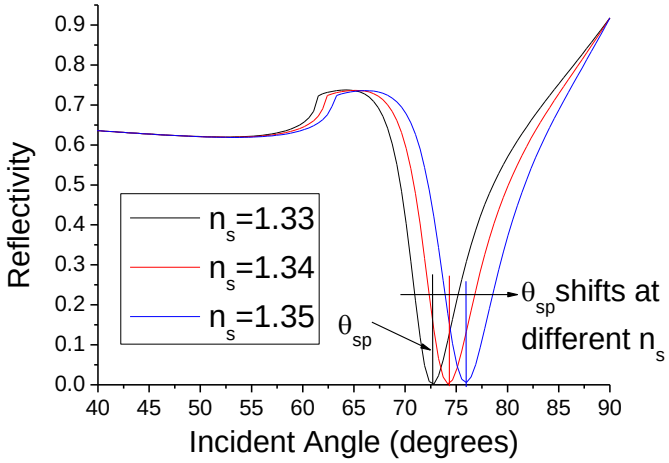

Figure 1.7. SPR curves. Different refractive index have different resonance angle

1.6 Penetration depth and propagation length

Eq.(20) gives the dispersion relation of $\omega(K_x)$.[3] Actually, ε_m is always complex numbers. K_{sp} describes a SPR if the real part of ε_m is negative and its absolute value is smaller than ε_s. Beside a real ω and ε_s if $\varepsilon_m'' < \left|\varepsilon_m'\right|$ (which $\varepsilon_m = \varepsilon_m' + i\varepsilon_m'$), a complex will be obtained $K_{sp} = K_{sp}' + iK_x''$ with

$$K_{sp}^{'} = \frac{\omega_0}{c}\sqrt{\frac{\varepsilon_m^{'}\varepsilon_s}{\varepsilon_m^{'}+\varepsilon_s}} \qquad (22)$$

$$K_{sp}^{''} = \frac{\omega_0}{c}\left(\frac{\varepsilon_m^{'}\varepsilon_s}{\varepsilon_m^{'}+\varepsilon_s}\right)^{3/2}\frac{\varepsilon_m^{''}}{2\left(\varepsilon_m^{'}\right)^2} \qquad (23)$$

For real K_{sp}' one needs $\varepsilon_m^{'} < 0$ and $\left|\varepsilon_m^{'}\right| > \varepsilon_s$, which can be fulfilled in a metal and also in a doped semiconductor near the eigen frequency. And the real and imaginary parts of the wave vector K_{sp} describe spatial periodicity and attenuation of an SPR wave in the direction of propagation[8].

Propagation length:

The intensity of SPs propagating along a smooth surface decreases as $e^{-2K_{sp}^{''}x}$ with $K_{sp}^{''}$ from Eq.(23). The length L_i after which the intensity decreases to 1/e is then given by

$$L_i = \left(2K_{sp}^{''}\right)^{-1} \qquad (24)$$

The absorbed energy heats the film, and can be measured with a photoacoustic cell.

Penetration depth:

As mentioned above, the field amplitude of the SPs decreases exponentially as $\exp(-|k_{zi}||z|)$(which is shown in Eq.16), normal to the surface. The value of the penetration depth at which the field falls to 1/e, becomes

$$d_p = \frac{1}{|k_{zi}|} \qquad (25)$$

In the sample region with ε_s: $d_p = \frac{\lambda}{2\pi}\left(\frac{\varepsilon_m^{'} + \varepsilon_s}{\varepsilon_s^2}\right)^{1/2}$

In the metal region with ε_m: $d_p = \frac{\lambda}{2\pi}\left(\frac{\varepsilon_m^{'} + \varepsilon_s}{\varepsilon_1^{'2}}\right)^{1/2}$

Figure 1.8 is the distribution of the magnetic field intensity for an SPW at the interface between gold and dielectric (n_s=1.32) in the direction perpendicular to the interface calculated for two different wavelengths.

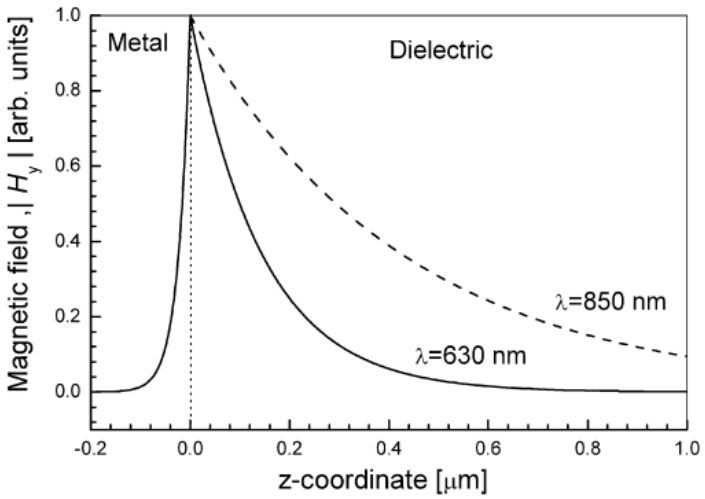

Figure 1.8. Penetration depth in metal and dielectric layer.[9]

The surface plasmon resonance angle mainly depends on the properties of the metal film, the wavelength of the incident light and the refractive index of the media on either side of the metal film. Because the refractive index is sensitive to temperature, it is important to perform the measurements at defined temperatures.

The metal must have conduction band electrons capable of resonating with the incoming light at a suitable wavelength. Metals that satisfy to this condition are silver, gold, copper, aluminum, sodium and indium. In these metals, silver and gold are two most common used metals. Silver exhibits a sharper resonance peak

than gold and provides a more precise measurement of coupling angle.[10] The different widths of the resonance peaks are due to intrinsic damping of the surface plasmon oscillations on the metal films. All the SP support materials will tend to dampen SP oscillations to varying degrees due to scattering of the electric field of the excitation light. The indicator of damping is the imaginary part of the dielectric value of the material. Damping increases with larger imaginary dielectric values. Gold and silver have imaginary dielectric values that are 20 times lower than any other support metal, with silver having a slightly lower value than gold.[11, 12]

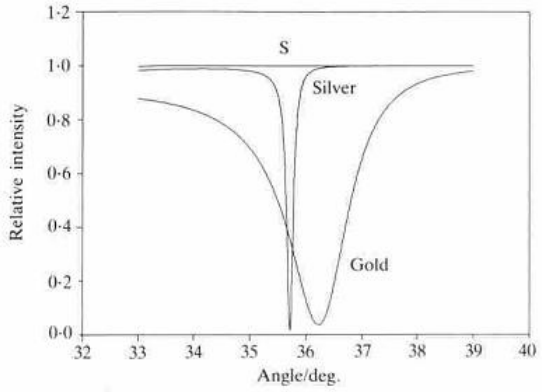

Figure 1.9. Resonance peak at different metal film.[13]

Although silver exhibits better optical properties for coupling light into the SP mode, it has several disadvantages which make the gold more popular using as the SP support film. First, silver will form oxides when exposured to air, and this can cause a resonance point shift and broaden the peaks. Secondly, the silver is more reactive than gold. The drawback of gold is the adhesion of gold to glass is not very good. It can be solved by add a very thin film Cr as adhesion layer.

1.7 SPR imaging

By fixing the detector at a specific angle along the resonance dip's linear regime, the reflcted beam intensity can be monitored as a linear function of refrative index change in the testing sample, called fixed angle SPR (Figure1.10).

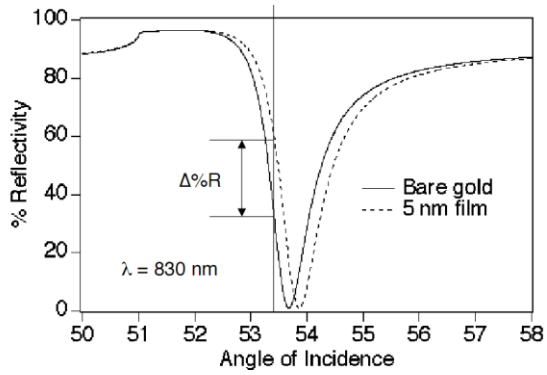

Figure 1.10 SPR fixed angle response.

Local information of SPR can also be extracted. This is called SPR imaging (SPRi), and this imaging capability make SPRi popular for higher throughput applications[14, 15]. SPRi images are typically extracted from a fixed angle response. This means the detector is held constant so that localized changes in refractive index near the surface can be observed as localized changes in the reflected intensity. When combined with biomolecule patterning on the sensor surface, this technique can essentially perform many SPR experiments in parallel (Figure 1.11). SPRi is very powerful technique for imaging the surface, and it is also the base of the methods developed in this thesis.

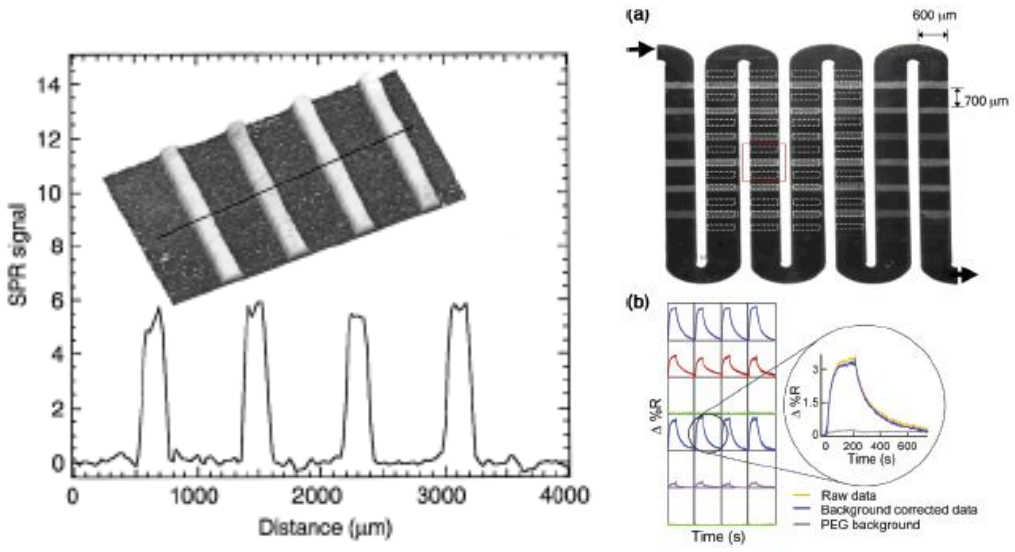

Figure.1.11. A typical SPR imaging response.[14, 15]

CHAPTER 2

PRINCIPLE OF PLASMONIC-BASED ELECTROCHEMICAL IMAGING (PECI) TECHNIQUE

2.1 Introduction

Electrochemistry is one of the most successful methods in analytical chemistry. It has very high sensitivity to detect the current which caused by reaction on the working electrode. Since the current is due to electron exchange on the whole of electrode, the normal electrochemical method is lack of ability to image local current distribution. Although scanning electrochemical microscope (SECM) has ability to image local current distribution, but the throughput of this method is low and it need complicated instrument. Therefore, a high throughput current imaging technique is needed and developed in this thesis which is called plasmonic-based electrochemical imaging (PECI) technique.

SPR technique is highly sensitive to various processes taking place on a metal film. It has been proved as a powerful label-free method to study protein-protein binding process taking place on a surface. And many applications have been developed in the SPR based biosensor field. SPR imaging (SPRi) technique is an optical method which can image and observe the local refractive index change near or on the sensing surface. PECI technique is a technique utilized advantage of SPRi (fast imaging ability) onto electrochemistry method. It can image the local electrochemical current and impedance on the electrode at a very

high throughput (the throughput equal to the frame rate, about 1000 frame per second (fps) for normal camera it can increase up to 1 million fps).

There are some efforts already been done in the EC-SPR fields. One of the first SPR studies of electrochemical reactions was based on detecting local surface potential.[16] Other approaches include detection of surface bound redox species,[17-23] redox-induced conformational changes in surface bound proteins,[21] potential-controlled DNA melting, electrochemical polymerization,[24, 25] and anodic stripping and detection of metal ions.[18] In general, SPR signal responses to 1) refractive index change on the metal film, 2) bulk refractive index changes near the metal film, and 3) dielectric property changes of the metal film. These studies mentioned before are mainly focused on adsorption/desorption processes on sensing surface or changes in the adsorbed species.

When an electrochemical potential applied onto the SPR surface, two effects will contribute to SPR signal: first is refractive index change due to the faradaic reaction. When EC reaction happens, the refractive index near the gold surface will change, which is due to the concentration of redox molecule changes. This process will generate SPR signal. Second, SPR also is sensitive to the charge density in the metal film. Due to the double layer charging effect, a potential change will cause surface charge density varies which will also give SPR signal. This part of SPR signal corresponds to charging process (non-faradaic process) and represents the electrochemical impedance information of the surface. To understand and get further information of this method, a quantitative relationship

between the SPR signal and the current and impedance measured by conventional electrochemical methods should be established.

In this chapter, first part is to describe the relationship between SPR signal caused by EC reaction and the EC current, and then method and process are given to calculate the EC current from SPR signal. Second part is the theory of PECI impedance which describes the relationship between SPR signal caused by surface charge density and surface impedance. Last part is the combine of these two effects.

2.2 Theory part 1: from SPR signal to faradaic current

In this section, a quantitative relationship between the PECI signal and the faradaic current measured by conventional electrochemical methods is established. As an example, the formalism is applied to the most widely used electrochemical method, potential-sweep measurements. Furthermore, by considering diffusion-controlled reversible redox reactions, explicit expressions of the PECI signal in terms of important electrochemical parameters is obtained as a function of potential and time. Finally, the equation and the process to calculate EC faradaic current from PECI signal is described.

2.2.1 Electrochemical reactions

An important family of electrochemical reactions is considered, in which neither reactants nor products bind to the electrode surface. In this case, SPR measures the reaction-induced changes in the bulk refractive index near the

electrode. The SPR response (e.g., resonance angle shift) can be described in terms of the reactant and product concentrations, C_O and C_R, and given by

$$\theta(t) = B\int_0^\infty [\alpha_O C_O(z,t) + \alpha_R C_R(z,t)]e^{-z/l}d(z/l) \ , \qquad (1)$$

where α_O and α_R are the changes in the local refractive index per unit concentration for the oxidized and reduced molecules, respectively. The constant, B, in Eq. 1 measures the sensitivity of the SPR angle to a change in the bulk index of refraction, which can be calibrated for a given SPR setup and reaction species. The exponential term in the integral is the decay of the evanesce field from the metal into the solution phase, where the decay length, l, is on the order of 200 nm. Note that, in principle, l is also a function of C_O and C_R, but to a first order of approximation one can regard l as a constant.

For a given set of boundary and initial conditions, C_O and C_R can be readily determined by solving the diffusion/rate equations. If the electrochemical reaction is the rate-limited process, then C_O and C_R are determined by the reaction rate. On the other hand, if the reaction is diffusion limited, C_O and C_R can be determined from the diffusion equation. So SPR measures local reaction kinetics, and this unique capability is ideal for studying heterogeneous chemical reactions, taking advantage of the spatial resolution of SPR imaging.

Eq. 1 can be simplified if the time scale of measurement is slower than the diffuse time of the reaction species over a distance of l ~200 nm. In this case, Eq. 1 is replaced by

$$\theta(t) \approx B\left[\alpha_O C_O(z,t)|_{z=0} + \alpha_R C_R(z,t)|_{z=0}\right] , \qquad (2)$$

where $C_O(x,y,z,t)|_{z=0}$ and $C_R(x,y,z,t)|_{z=0}$ are the concentrations of the oxidized and reduced molecules near the electrode. For most ions and molecules in dilute solutions, with diffusion coefficient in the range of 10^{-9} to $10^{-11}m^2/s$,[26] the diffusion time given by $l^2/(2D)$ is less than a millisecond, so Eq. 2 holds well for most electrochemical measurements. According to Eq. 2, SPR directly measures the local concentrations of oxidized and reduced species on the electrode surface.

In contrast, conventional electrochemical methods measure current density vs. potential or time, which is related to C_O and C_R according to[27]

$$I = nFD_O \frac{\partial C_O}{\partial z}\Big|_{z=0} = -nFD_R \frac{\partial C_R}{\partial z}\Big|_{z=0} \quad , \quad (3)$$

where n is number of electrons transferred per reaction, F is Faraday constant, and D_O and D_R are the diffusion coefficients of the reaction species. Comparing Eqs. 1 and 3, both SPR and current measurements are related to the concentrations of the reactant and product, but they are not identical. SPR is detecting the concentration changes near the working electrode surface, while current measures the concentration gradient. In this respect, SRP signal reflects more direct information about reaction than concentration gradient which is measured by current.

A quantitative relationship between SPR signals and the current is developed in the next section, and then consider a more specific example, reversible redox reactions.

2.2.2 Relationship between current and SPR signals

Let's consider a redox reaction,

$$O + ne \underset{k_b}{\overset{k_f}{\Leftrightarrow}} R$$

where k_f and k_b are forward and backward reaction rates. If assuming one-dimensional (along z-axis) and semi-infinite geometry, the diffusion equation of O is,

$$\frac{\partial C_O}{\partial t} = D_0 \frac{\partial^2 C_O}{\partial z^2} \qquad (4)$$

where $C_O(z,t)$ and D_O are the concentration and diffusion coefficient of O.

Performing Laplace transform on Eq. 4:

$$s\tilde{C}_O(z,s) - C_O^0 = D_0 \frac{\partial^2 \tilde{C}_O(z,s)}{\partial z^2} \qquad (5)$$

where $\tilde{C}_O(z,s)$ is the Laplace transform of $C_O(z,t)$ and C_O^0 is the initial concentration of O, which is assumed to be a constant. The solution of Eq. 5 is

$$\tilde{C}_O(z,s) = s^{-1}C_O^0 + A(s)\exp[-(s/D_O)^{1/2} z] \qquad (6)$$

where A(s) is a function to be determined from boundary conditions at the electrode surface. To relate the concentrations to current density, Laplace transform is performed on Eq. 3 and it is conbined with Eq. 6, which leads to

$$\tilde{C}_O(0,s) = s^{-1}C_O^0 - (nFD_O^{1/2})^{-1} s^{-1/2}\tilde{I}(s) \qquad (7)$$

Inverse Laplace transform of Eq. 7,[27] gives

$$C_O(0,t) = C_O^0 - [nF(\pi D_O)^{1/2}]^{-1} \int_0^t i(t')(t-t')^{-1/2} dt' \qquad (8)$$

Using the same procedure, the concentration for the reduced species, R, is obtained on the electrode surface, given by

$$C_R(0,t) = C_R^0 + [nF(\pi D_R)^{1/2}]^{-1} \int_0^t i(t')(t-t')^{-1/2} dt' \qquad (9)$$

Substituting Eqs. 8 and 9 into Eq. 2:

$$\theta(t) = \theta_0 + B(\alpha_R D_R^{-1/2} - \alpha_O D_O^{-1/2})(nF\pi^{1/2})^{-1} \int_0^t i(t')(t-t')^{-1/2} dt' \qquad (10)$$

where $\theta_0 = \alpha_O C_O^0 + \alpha_R C_R^0$ is the SPR signal at t=0. Eq. 10 can be written in a more convenient form as

$$\Delta\theta(t) = B(\alpha_R D_R^{-1/2} - \alpha_O D_O^{-1/2})(nF\pi^{1/2})^{-1} \int_0^t i(t)(t-t)^{-1/2} dt \qquad (11)$$

where $\Delta\theta = \theta(t) - \theta_0$, measures the shift in the SPR signal. Eq. 11 provides a quantitative relation between the PECI signal and the electrochemical current density measured by conventional electrochemical methods.

It is important to note that the SPR signal is a convolution function of current, according to Eq. 11. Saveant and co-workers [28] have developed convolution voltammetry by numerically computing the convolution integral in Eq. 11. Compared with the more traditional voltammetry that is based on the analysis of peak currents and potentials, the convolution voltammetry has many advantages but is not directly measured and thus less convenient[27]. An important conclusion from the above analysis is that SPR measures the

convolution voltammetry directly without the need of performing numerical computation.

From Eq. 11, i(t) can be also expressed in terms of (t), given by,

$$i(t) = (B\alpha_R D_R^{-1/2} - B\alpha_O D_O^{-1/2})^{-1} nFL^{-1}\{s^{1/2}\Delta\theta(s)\} \qquad (12)$$

Eq. 12 allows to determine the current density from the SPR signal.

2.2.3 Relationship between SPR signal and applied potential for reversible reactions

Eqs. 11 and 12 provide a quantitative relationship between SPR and current signals. Now a more explicit expression of the SPR signal in terms of important diffusion, thermodynamic and kinetic parameters, as a function of potential and time is needed. This requires one to define the boundary conditions. The semi-infinite geometry implies that the concentrations of O and R far away from the electrode surface are fixed at the initial values. At the electrode surface, flux balance (steady state) requires that

$$D_O \frac{\partial C_O(0,t)}{\partial z} = -D_R \frac{\partial C_R(0,t)}{\partial z} \qquad (13)$$

Combining the Laplace transform of Eq. 13 with the solutions of the diffusion equations (Eq. 6 for O and a similar express for R):

$$\xi C_O(0,t) + C_R(0,t) = \xi C_O^0 + C_R^0 \qquad (14)$$

where $\xi=(D_O/D_R)^{1/2}$. In order to determine the SPR signal using Eq. 2, both $C_O(0,t)$ and $C_R(0,t)$ are needed, which requires another boundary condition at the electrode surface.

By assuming that the reaction is fully reversible, the forward and backward reaction rates will be large, and the Nernst law,

$$\frac{C_O(0,t)}{C_R(0,t)}=\exp[\frac{nF}{RT}(E(t)-E^0)], \qquad (15).$$

holds, where R is the molar gas constant, T is temperature and E^0 is the standard potential.

Combining Eqs. 14 and 15, $C_O(0,t)$ and $C_R(0,t)$ can be determined and substituting them into Eq. 3:

$$s\Delta\theta(E)=\frac{\xi S(E)\alpha_O C^0}{1+\xi S(E)}+\frac{\xi\alpha_R C^0}{1+\xi S(E)}, \qquad (16)$$

where $S(E)=\exp[\frac{nF}{RT}(E-E^0)]$.

2.2.4 Linear potential sweep measurements

Similar to cyclic voltammetry (CV), one can measure SPR response while cycling the electrode potential. The SPR signal vs. potential is given by Eq. 16 by simply replacing E in the equation with

$$E(t)=E_i-vt \text{ for } 0 < t < (E_f-E_i)/v \qquad (17)$$

and

$$E(t)=E_f+vt \text{ for } (E_f-E_i)/v < t < 2(E_f-E_i)/v, \qquad (18)$$

where E_i and E_f are the upper (initial) and lower limits of the potential, and v is the potential sweep rate. According to Eq. 16, the PECI signal is independent of the potential sweep rate. If C_R^0=0, then the PECI signal is simply proportional to the initial concentration of O.

2.2.5 Potential step measurements

Potential step techniques measure SPR response vs. time after stepping the electrode potential to a fixed value. In this case, the SPR signal is also given by Eq. 16 by replacing E(t) with

$$E(t) = \begin{cases} 0, & t < 0 \\ E, & t > 0 \end{cases}.$$

It is clear that the PECI signal is a constant (t > 0), and the value is determined by S(E), the relative concentrations of the reaction species. The PECI value is also proportional to the initial concentration of O if the initial concentration of R is zero.

Note that Eq. 16 was obtained assuming that t >> l^2/D. For potential-step measurements, if one is interested in the initial time scale < l^2/D, Eq. 1 should be used. In this case, one needs to determine the complete concentration profiles of O and R, which can be obtained by solving the diffusion equations (Eq. 4 for O and a similar equation for R) together with the initial and boundary conditions (Eqs. 14 and 15). The results are:

$$C_O(z,t) = C^0 - \frac{C^0}{1+\xi S(E)} erfc[\frac{z}{2(D_O t)^{1/2}}] \qquad (19)$$

$$C_R(z,t) = \frac{\xi C^0}{1+\xi S(E)} erfc[\frac{z}{2(D_R t)^{1/2}}] \qquad (20)$$

where the erfc-terms are error functions. Substituting Eqs. 19 and 20 into Eq. 1, one can calculate potential-step SPR response, including the very initial process during the diffusion of reaction species over the thin SPR measurable layer (l~200 nm). For t >> $l^2/(2D_O)$, $l^2/(2D_R)$

$erfc[\frac{z}{2(D_O t)^{1/2}}] \sim erfc(0) = 1,$ and

$erfc[\frac{z}{2(D_R t)^{1/2}}] \sim erfc(0) = 1,$ and consequently, the PECI signal returns to Eq. 16.

2.2.6 Process to calculate faradaic current from SPR signal

Relationship between SRP signal and faradaic current has been discussed in previous section, which has shown ability to calculate the local current from SPR signal pixel by pixel. Therefore the current intensity map of the working electrode surface can be measured and calculated from SPR imaging response. Note that so far only the SPR response caused by faradaic reaction is considered, charging effect will also give SPR signal which will be discussed next.

To calculate current from SPR signal, the Eq.(12) should be applied to the SPR signal. But there is no reverse Laplace transform functions in time domain

which correspond with the function: $s^{(1/2)}$, therefore it is difficult to do reverse Laplace transform for function ($s^{(1/2)}\Delta\theta$) by convolution integral. This does not mean current cannot be calculated from SPR signal, it just means there is no formulated equation that can be used directly to calculate current from SPR signal.

Eq. (11) describes the relationship between faradaic current and SPR signal. SPR signal can be calculated from current and also current can be calcualted from SPR by Eq.(11). In practice, the integral in Eq.(11) can be expressed by the sum, the Eq.(11) can be rewrote by

$$\Delta\theta(t_N) = \beta \sum_{0}^{t_N} i(t_n)(t_N - t_n)^{-\frac{1}{2}}\Delta t \qquad (21)$$

where $= B\left(\alpha_R {D_R}^{-\frac{1}{2}} - \alpha_O {D_O}^{-\frac{1}{2}}\right)$. Since SPR signal is measured by experiment, thus the $\Delta\theta(t_n)$ is know for the whole reaction process from $t=t_0$ to $t = t_N$. If the current at each time point from $i(t_0)$ to $i(t_{N-1})$ is known, i_N can be calculated from Eq.(21). For most situation, the $i(t_0)=0$, therefore recursion method can be used to calculate the current from SPR signal for the whole reaction process.

2.3 Theory part 2: from SPR signal to impedance and charging current

2.3.1 Electrical double layer of the surface

When solid surface, for example electrodes like gold, contacts an aqueous solution including electrolyte, the solid surface becomes charged due to the different of electron (or ion) affinities between the solid surface and the solution

or the ionization of surface groups. In general, protonation, deprotonation, adsorption and other reaction equilibria define a net charge density on the surface. This charge density creates an electric field, drawing oppositely charged ions towards it and driving like-charged ions away. This layer will shield the surface charge on the interface between solid and aqueous solution. The shielding layer is commonly known as a Debye layer or electrical double layer (EDL).

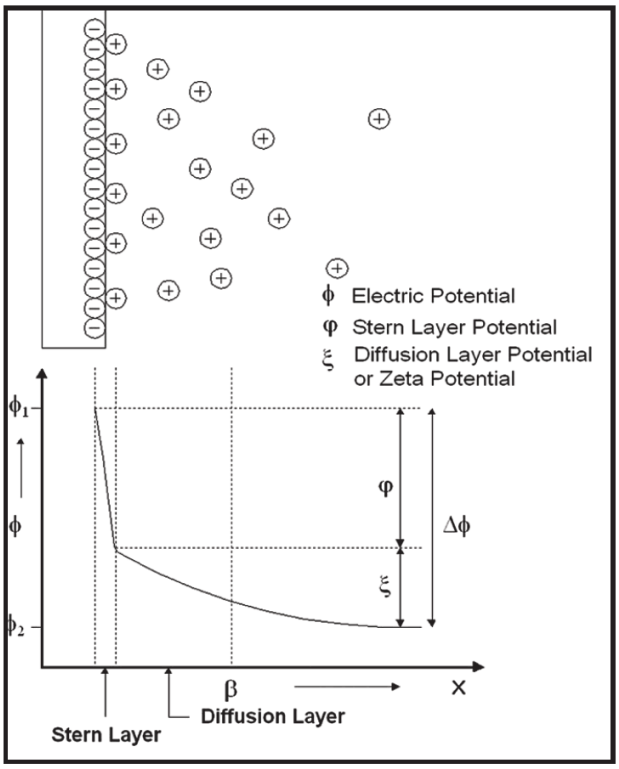

Figure 2.1. Electric double layer. From ref. [29].

Most double layer models are based on Gouy-Chapman-Stern (GCS) model. The GCS model consists of two layers: Stern layer and diffuse layer as shown in Figure 2.1. The Stern layer is the region next to the surface, and ions in the Stern layer are bound near the surface due to specially adsorbing and Coulomb interactions. The diffusion layer is the region next to the Stern layer and

ions in the diffusion layer can move freely in any direction. Within Stern layer, there are two planes, the inner Helmholtz plane (IHP) and the outer Helmholtz plane (OHP). Whole surface charge system can be considered as a capacitor, while the EDL includes high concentration of same charged ion which surve as one electrode of surface capacitor, and the solid surface (Au surface in our situation) which has couterions can be considered as another electrode.

2.3.2 SPR signal of Double layer charging contribution: surface impedance

The above discussion did not consider the potential-induced change in the dielectric properties of the metal film. The EDL and the electrode can be considered as a capacitor, when the potential changes the charge density in EDL and metal film change and thus the surface plasmon resonance frequency also changes.

By measuring SPR in an electrolyte, interfacial impedance can be obtained by applying a potential modulation to the sensor surface. This is because the potential modulation causes a surface charge modulation which changes the surface plasmons in the metal film. By measuring the amplitude and phase of the resonance angle, interfacial impedance information can be obtained. A modulation in the resonance angle smaller than 10^{-6} deg can be measured[30] has been demonstrated before, so an accurate imaging of surface impedance is possible based on SPR detection. More importantly, by operating SPR in imaging mode an image of the impedance of the entire electrode surface can be obtained.

A quantitative relation between SPR signal (angle modulation) and interfacial impedance can be derived based on the following analysis. First, the resonance angle, θ_R, depends on the dielectric constant of the metal film according to[31]

$$\sin(\theta_R) = \sqrt{\frac{\varepsilon_1 \varepsilon_m}{(\varepsilon_1 + \varepsilon_m)\varepsilon_2}}, \qquad (22)$$

where ε_1 and ε_2 are the dielectric constants of the buffer solution and prism, respectively, and ε_m is the real part of the dielectric constant of the metal film. ε_m depends on the surface charge density, which is the reason that the SPR resonance angle is sensitive to the surface charge density. An explicit relationship betweenε_m and surface charge density can be obtained based on the Drude model, a free-electron gas model for metals. According to the Drude model, ε_m of the metal film as a function of frequency, f, is given by

$$\varepsilon_m(f) = 1 - \frac{n_e e^2}{\varepsilon_0 m_e 4\pi^2 f^2} \quad , \qquad (23)$$

where e, m_e and n_e are the electron charge, mass and density, respectively, and ε_0=8.85x10^{-12} F/m. For a thin metal film of thickness d_m, a change in the surface charge, $\Delta\sigma$, gives rise to a change in the electron density and thus the dielectric constant of the metal according to

$$\Delta\sigma = -ed_m \Delta n_e = -\frac{ed_m n_e}{\varepsilon_m - 1}\Delta\varepsilon_m . \quad (24)$$

Relation between $\Delta\varepsilon_m$and $\Delta\theta_R$ can be obtained from derivative of equation square (22):

$$2\sin(\theta_R)\cos(\theta_R)\frac{\Delta\theta_R}{\Delta\varepsilon_m} = \frac{\varepsilon_1^2}{(\varepsilon_1+\varepsilon_m)^2\varepsilon_2} \qquad (25)$$

$$\Delta\varepsilon_m = \frac{\sin(2\theta_R)(\varepsilon_1+\varepsilon_m)^2\varepsilon_2}{\varepsilon_1^2}\Delta\theta_R \qquad (26)$$

Combining Eqs 24 and 26, a change in the surface charge ($\Delta\sigma$) causes a change in the resonance angle, $\Delta\theta_R$, and given by

$$\Delta\sigma = \alpha\Delta\theta \qquad (27)$$

where

$$\alpha = -\frac{ed_m n_e \varepsilon_2(\varepsilon_1+\varepsilon_m)^2\sin(2\theta_R)}{\varepsilon_1^2(\varepsilon_m-1)}. \quad (28)$$

In the present experiment, ε_1=1.77 (water), ε_2 =2.29 (BK7 prism), d_m=47 nm, n_e=5.9x10^{-28} m^{-3} and ε_m=-11.7 for the Au film, θ_R=72 ° according to Eq. 1, and α_{cal}=28 C.m^{-2}deg^{-1}. Finally since surface charge density is related to interfacial capacitance density (capacitance per unit area), c, by

$$\Delta\sigma = C_p(x,y)\Delta V_{int} \qquad (29)$$

where ΔV_{int} is the surface potential drop on the interface which can be modulated and controlled using a standard electrochemical setup. One can image the interfacial capacitance by monitoring the local SPR response due to the applied potential modulation by

$$C_p(x,y) = \frac{\alpha\Delta\theta(x,y)}{\Delta V_{int}} \qquad (30)$$

The above analysis establishes a simple relation between potential-modulated local SPR and local interfacial capacitance, which is the basic principle of interfacial impedance imaging technique. The Drude model provides a semi-

quantitative description of our experimental data. When the Drude free electron gas model is replaced with a more sophisticated theory, the above conclusion still holds except that α will change.

One assumption made in deriving the above relation is that the resistance of the electrolyte or buffer solution is negligible. While this assumption is reasonable in many cases, a more complete model (e.g., Randles equivalent circuit model[32]) treats the metal-solution interface by a capacitor, C_p, in parallel with a resistor, R_p, and the solution phase resistance by a resistor, R_s (Figure 2.2). This extra resistance introduces a phase shift between the resonance angle modulation, $\Delta\theta_R(x,y)$, and the potential modulation, ΔV. In this case, both amplitude and phase images of the surface can be obtained. Using the Randles model, for a given applied modulation, ΔV_{app}, the actual potential modulation across the metal-solution interface is given by

$$\Delta V_{\text{int}eface} = \frac{Z_{(R_p // C_p(x,y))}}{Z_{tot}} \Delta V_{app} = \frac{R_p}{R_p + R_s + j2\pi f R_p R_s C_p(x,y)} \Delta V_{app} \quad , (31)$$

where C_p is the total capacitance of the metal-solution interface and is location dependent (see Eq. 31), and Z_{tot} is the total impedance of the whole system, $Z_{(R_p // C_p(x,y))}$ is the impedance of R_p parallel with C_p. The local resonance angle is obtained by replacing ΔV_{int} in Eq. 30 by Eq. 31, which takes the form of

$$\Delta\theta_R(x,y) = \frac{C_p}{\alpha} \frac{Z_{(R_p // C_p(x,y))}}{Z_{tot}} \Delta V_{app} = \frac{R_p C_p(x,y)}{\alpha(R_p + R_s + j2\pi f R_p R_s C_p(x,y))} \Delta V_{app} . \quad (32)$$

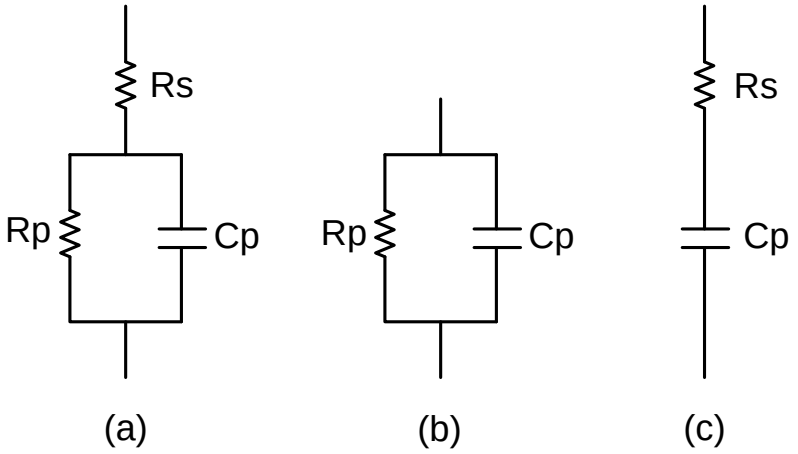

Figure 2.2. Equivalent circuits used in modeling surface impedance. (a) Randles equivalent circuit, (b) 2 component model with parallel resistor and capacitor and (c) 2 component model with serial resistor and capacitor.

When there is no reaction on surface, the surface resistor R_p is infinite, that's true in most of cases, therefore R_P can be set to ∞ in Eq(32) then relationship between $\Delta\theta_R(x,y)$ and ΔV_{app} when there is no surface reaction happens will be obtained.

$$\Delta\theta_R(x,y) = \frac{C_p(x,y)}{\alpha(1+j2\pi f C_P(x,y)R_s)}\Delta V_{app} \qquad (33)$$

The equation can be also be expressed in terms of impedance Z_{tot}, which $Z_{tot} = R_s + \frac{1}{j\omega C_P}$.

$$\Delta\theta_R(x,y) = \frac{C_p(x,y)}{\alpha}\Delta V_{int} = \frac{C_p(x,y)}{\alpha}\frac{\frac{1}{j\omega C_p(x,y)}}{R_s + j\omega C_p(x,y)}\Delta V_{app}$$

$$= \frac{1}{\alpha}\frac{\frac{1}{j\omega}}{Z_{tot}}\Delta V_{app} \qquad (34)$$

$$\frac{\Delta\theta_R(x,y)}{\Delta V_{app}} = \frac{1}{j\alpha\omega Z_{tot}(x,y)} \qquad (35)$$

Eq.(35) shows the signal measured by SPR is really reverse of the impedance of whole system Z which multiplied by frequency and α. Only when the solution resistance R_s is small enough to compare with $\frac{1}{j\omega C_p}$, the equation (35) simplify to $\frac{\Delta\theta_R(x,y)}{\Delta V_{app}} = C_p(x,y)/\alpha$, so SPR signal amplitude is proportional to the capacitor. Therefore from Eq.35 impedance of whole system $Z_{tot}(x,y)$ can be calculated from SPR response $\Delta\theta_R(x,y)$.

2.3.3 Relationship between charging current and SPR signal

Last section is focused on how to express impedance of whole system by SPR signal. Since SPR signal represent the surface charge density, charging current can also be expressed by SPR signal. The equation to calculate faradaic current from SPR signal has been already derived. Here the equation to calculate charging current from SPR signal will be derived. This will complete the relationship between EC current and SPR signal which will be discussed in the next section.

From Eq.27 the relationship between SPR signal and charging current can be simply expressed as:

$$\Delta\theta = \frac{1}{\alpha}\Delta\sigma = \frac{1}{\alpha}\int_0^t i_d(t)dt \qquad (36)$$

Where $i_d(t)$ is the polarization or double layer charging current. Actually the SPR signal $\Delta\theta$ has x and y two dimension, therefore the Eq.36 can be rewrote as:

$$\Delta\theta(x,y,t) = \frac{1}{\alpha}\int_0^t i_d(x,y,t)dt \qquad (37)$$

Therefore,

$$i_d(x,y,t) = \alpha\frac{d\theta(x,y,t)}{dt} \qquad (38)$$

Eq.(38) shows that PECI also measures the double layer charging current, and the time derivative of the SPR signal is directly proportional to the double layer charging current. Other techniques seldom use i(x,y,t), because the conventional current method always measures the average effect of certain area. On the other hand, since SPR is an optical method, from Eq.(38) the local charging current density at any location (x,y) can be calculated from SPR image response $\Delta\theta(x,y,t)$.

2.4 Theory part 3: the whole picture, relationship between SPR signal and total current (including faradaic and charging current)

The relationship between SPR signal and faradaic and charging current has been discussed in last two sections, and also derived equations to calculate both faradaic current and charging current from SPR signal. If the PECI process has both faradaic current and charging current component, Eq. 11, which represent the faradaic current response, will combine with Eq.37, which correspond to charging current response, to get the total equation for relationship between SPR signal and total EC current (faradaic and charging current):

$\Delta\theta(x,y,t) = \Delta\theta_f(x,y,t) + \Delta\theta_d(x,y,t)$

$$= B\left(\alpha_R D_R^{-\frac{1}{2}} - \alpha_O D_O^{-\frac{1}{2}}\right)(nF\pi^{1/2})^{-1}\int_0^t i_f(x,y,t')(t-t')^{-1/2}dt' +$$

$$\frac{1}{\alpha}\int_0^t i_d(x,y,t)dt$$

$$= \beta\int_0^t i_f(x,y,t')(t-t')^{-1/2}dt' + \frac{1}{\alpha}\int_0^t i_d(x,y,t)dt \quad (39)$$

Where i_f is faradaic current, i_d is double layer charging current, β is constant which equal to $\left(\alpha_R D_R^{-\frac{1}{2}} - \alpha_O D_O^{-\frac{1}{2}}\right)(nF\pi^{1/2})^{-1}$.

If the background buffer or solution concentration is low, the double layer charging effect is relatively small compared with the bulk index of refraction changes arising from the redox reactions. In this situation, SPR signal due to charging effect can be ignored, and the total SPR signal should mostly due to faradaic current. Second part of the Eq. 39 can be dropped off. The local faradaic reaction current can be calculated and mapped from SPR image. This allows our SPREC imaging technique to observe heterogeneous reaction of surface. The application of this situation will be discussed in the next chapter.

If there is no EC reaction on the surface happened during the EC-SPR process, the SPR signal will be purely due to the charging effect. Therefore the first part of Eq.39 can be dropped off. SPR signal represents the integration of charging current and impedance of whole system (from Eq.35). This allows our SPREC imaging technique to measure the local impedance.

If the buffer concentration is not low and also faradaic reaction happens during the EC process, both parts in Eq.39 cannot be ignored. In this situation, if the faradaic reaction information is needed, reference region or control

experiment can be used to subtract out the charging effect from SPR signal. Another solution is to apply square wave voltammetry on the EC reaction, the charging effect will be minimized.

CHAPTER 3

IMAGING LOCAL ELECTROCHEMICAL CURREN BY PECI TECHNIQUE

3.1 Introduction

Electrochemical detection is a powerful analytical method that has been used for a wide range of applications, including trace chemical analysis, glucose and neurotransmitter monitoring, DNA and protein detections, and electrocatalysis studies. Measuring the total electrochemical current or other related electrical quantities of an electrode does not directly provide local reaction information of the electrode surface that is critically needed for many applications, such as heterogeneous reactions, local activities of cells, and protein and DNA microarrays. Scanning electrochemical microscopy (SECM)[33], which probes local electrochemical current by scanning a microelectrode across the surface, can overcome this limitation and has found numerous applications [34]. However, the sequential scanning of the microelectrode limits its speed and the scanning probe may perturb the local electrochemical processes under study. The current measured by the microelectrode in SECM scales with the size of the microelectrode, making it increasingly difficult to improve the spatial resolution by shrinking the microelectrode.

In this chapter a method called plasmonic-based electrochemical imaging technique is developed to image local electrochemical current without using a scanning probe or a microelectrode. Instead of measuring the current with an

electrode, it determines the electrochemical current density from an optical signal of the electrode surface generated from a SPR[35, 36]. Important benefits of this approach include fast and non-invasive electrochemical current imaging of the surface. In addition, the measured local current signal is proportional to the incident light intensity, which does not scale with the area of a region of interest.

3.2 The principle and the experiment setup

An electrochemical reaction taking place on an electrode always involves electron transfer between the electrode and the reactant, which is measured as an electrochemical current or related electrical signal in the conventional electrochemical methods. The electron transfer process is also always accompanied by a conversion of chemical species between oxidized and reduced states, so one may determine the electrochemical current by monitoring the conversion of the chemical species on the surface, which is the principle of the present imaging technique. SPR is extremely sensitive to the species generated (or consumed) on the electrode surface (Figure 3.1A) compared to other optical detection methods, such as phase-measurement microscopy[37] that have been used to study local molecular binding events and electrochemical reactions on surfaces[38, 39].

In the chapter 2 section 2.2, it has been shown that the concentration of the species is directly related to the electrochemical current via Fick's law of diffusion[40], and more importantly, the electrochemical current density, $i(t)$, can be easily calculated from the local SPR signal, according to[41]

$$i(t) = bnFL^{-1}\left\{s^{1/2}\Delta\tilde{\theta}_{SPR}(s)\right\} \quad (1)$$

where $b = \left[B(\alpha_R D_R^{-1/2} - \alpha_O D_O^{-1/2}\right]^{-1}$, n is number of electron involved in the redox reaction, F is the Faraday constant, L^{-1} stands for inverse Laplace transform, and $\Delta\tilde{\theta}_{SPR}(s)$ is the Laplace transform of the SPR signal. In the expression for b, α_R and α_O are the changes in the local refractive indices per unit concentration for the oxidized and reduced molecules, D_O and D_R are the diffusion coefficients of the oxidized and reduced molecules, and B measures the sensitivity of the SPR signal to a change in the bulk index of refraction, which can be calibrated independently.

To obtain b, SPR angular shifts per unit concentration for the oxidized and reduced forms of the ruthenium complex were determined using an independent SPR system (BI-2000 from Biosensing Instruments, www.biosensingusa.com). First, the ruthenium complex in the oxidized state at each concentration was injected into the flow cell, and the SPR response was determined and used to calculate $B\alpha_O$. Second, in order to determine $B\alpha_R$, the ruthenium complex is converted to the reduced state by applying a negative electrode potential value (-0.3 V). $B\alpha_R$ and $B\alpha_O$ were found to be 2.5 mDeg/mM and 5 mDeg/mM, respectively. From $b=[B(\alpha_R D_R^{-1/2} - \alpha_O D_O^{-1/2})]^{-1}$, and assume $D_R = D_O = 5.3*10^{-10} m^2/s$, $b = -9.21 \times 10^{-6}$ m mM $Deg^{-1}S^{-1/2}$.

As been pointed out in Chapter 2, it is difficult to find the formulated equation to calculate reverse Laplace transform for Eq.1, therefore, the Eq. 11 in section 2.2 will be used to calculate the EC current from SPR signal. In practice, the integration of Eq.11 will be changed to sum, and the recursion method is used

to calculate current at each pixel at each time point (Eq.21 in Chapter 2). The details process is described in section 2.2.6.

According to Eq. 1, the measured signal, $i(t)$, does not scale with the image area, which is in contrast to the conventional electrochemical detection methods. Note that double charging current also contributes to the SPR signal[42], which is, however, small[43] comparing to faradaic current.

Two optical configurations were used in the experiments. In the first configuration, the working electrode was an Au-coated glass slide, which was attached onto a prism via index matching fluid. On top of the Au electrode, an electrochemical cell made from Teflon was mounted. A Pt wire counter electrode and a $Ag|AgCl|KCl_{(sat.)}$ reference electrode, together with a potentiostat, were used to control the potential of the working electrode. A light emitting diode with a peak wavelength of 670 nm was used to excite the surface plasmons in the Au electrode, and a CCD camera was used to record the image. Calculating the current at each pixel from the image using Eq. 1 creates an electrochemical current image, and the current image vs. time or potential provides local amperometric and voltammetric measurements of the electrode. The second configuration, as shown in Figure 3.2A used a high numerical aperture (NA=1.65) oil immersion objective[44] to replace the prism, and a HeNe laser to replace the LED. In comparison to the first configuration, the second one provided higher spatial resolution.

Local electrochemical currents generated by heterogeneous surface reactions is imaged, traditional electrochemical detection methods can also be

performed by PECI, such as amperometry, cyclic voltammetry, and square-wave voltammetry locally—interrogating areas as small as 0.2 um by 3um with a current sensitivity of 0.3pA. Sensitive and selective trace analysis is also demonstrated with the technique.

Chapter 3 has shown below that 1) the electrochemical current determined using Eq. 1 is indeed equivalent to that obtained from the conventional electrochemical methods; 2) the new electrochemical imaging technique provides local electrochemical current (e.g. cyclic voltammograms) associated with heterogeneous surface reactions; 3) advantages of this imaging technique allow for sensitive and selective trace analysis; and 4) high current sensitivity, fast imaging rate, and good spatial resolution can be achieved with the new imaging technique.

3.3 Principle demonstration: redox molecules reaction with finger printed electrode

One of the most important applications of the new imaging technique is to image local electrochemical current associated with heterogeneous reactions. To demonstrate this capability, a fingerprint[45] on a Au electrode is created by touching it, which transferred the secretions from the friction skin ridges of the finger onto the electrode surface. Figure 3.1 A shows a SPR image of fingerprint residue on Au electrode surface. Note that only the center part of image has best and sharpest contrast, it is because the prism distorts the image and only can focus on a line instead the whole surface. Figure3.1B shows another region of

fingerprint, the red rectangular shows the location of the EC current image which is going to show in next figure.

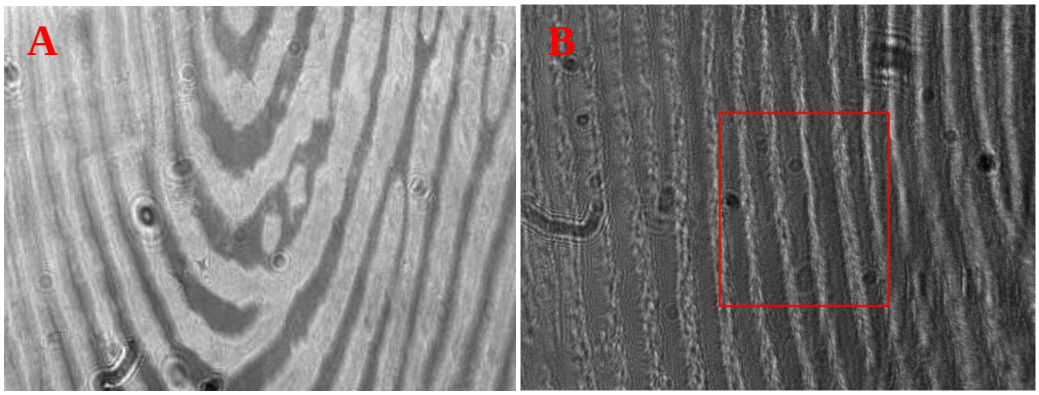

Figure 3.1. SPR image of fingerprint on Au. (A) SPR image of fingerprint residue on Au surface. (B) Another region of fingerprint, the red rectangular marks the region of EC current image area which is shown in Figure 3.2 C to F.

In order to demonstrate the imaging principle, the redox reaction of $Ru(NH_3)_6^{3+}$ complex has been studied by using conventional cyclic voltammetry and electrochemical imaging simultaneously. The conventional method measures the total electrochemical current of the entire electrode surface, and the voltammogram shows the characteristic redox peaks, corresponding to the reduction and oxidation of the ruthenium complex (red line, Figure 3.2B). The electrochemical imaging technique probes the local electrochemical current, so the current averaged over the entire surface vs. the potential (open circles, Figure 3.2B) is compared with the conventional voltammetry. The cyclic voltammograms obtained by the two methods are in good agreement with each other (overall deviation = 5.75%). Note that the parameter, *b*, in Eq. 1 was calibrated independently from a separate experiment,[41] so the agreement

between the voltammograms obtained with the conventional and present imaging method is quantitative and involves no adjusting parameters.

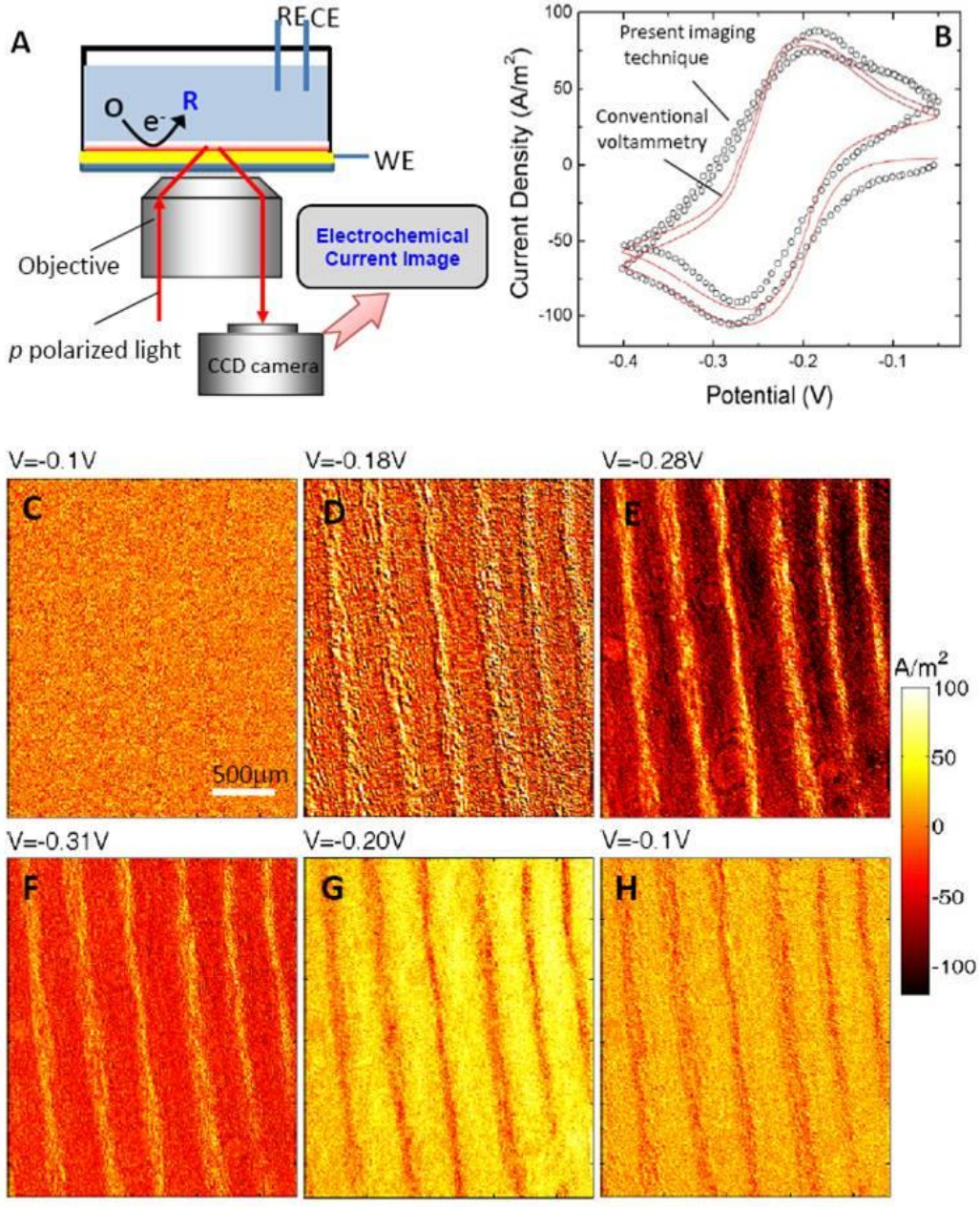

Figure 3.2. PECI image of fingerprint pattern. (A) Schematic illustration of an electrochemical current imaging technique. (B) Cyclic voltammograms measured by the conventional electrochemical method (red line) and by the electrochemical

current imaging technique (open circles) of a bare gold electrode. Note that for a close comparison between the two approaches the cyclic voltammogram from the imaging technique is averaged over the entire electrode surface. The electrolyte is 0.25M phosphate buffer containing 10 mM $Ru(NH_3)_6^{3+}$, and the potential sweep rate is 0.1 V/s. (C to F) Electrochemical current images of a fingerprint at different potentials recorded during continuous cycling of the electrode potential between -0.10V and -0.34V at a rate of 0.1V/s . The electrolyte is 0.25M phosphate buffer containing 10 mM $Ru(NH_3)_6^{3+}$.

Llocal electrochemical current of the surface is imaged by cycling the electrode potential in an electrolyte (0.25M phosphate buffer containing 10 mM $Ru(NH_3)_6^{3+}$). Figure 3.2, C to F, shows several snapshots of the electrochemical current video at different potentials. At -0.10 V, far away from the redox potential, almost no electrochemical reaction takes place and the image does not show any contrast (Figure 3.2C). As the potential decreases, reduction of $Ru(NH_3)_6^{3+}$ takes place and the contrast of the fingerprint begins to show up (Figure 3.2D). At -0.28V, the contrast reaches maximum, corresponding to the maximum reduction current (Figure 3.2E). As the potential cycles back towards positive potentials, the contrast is inverted (Figure 3.2G), which reflects a sign change in the electrochemical current (from reduction to oxidation). Finally, when the potential cycles back to -0.10 V, the contrast disappears nearly completely; the small remaining contrast is the result of residual electrochemical reactions at the potential, in agreement with the cyclic voltammetry, which shows a finite current when the potential returns to the starting value (Figure 3.2B).

The entire process was repeated by continuously cycling the potential. Note that the imaging speed is solely determined by the CCD imager, which was ~2000 frames/sec. in the present setup. It means to obtain the entire surface's current density only 0.5μS is needed which is much faster and easier than the SECM. And this speed can be further improved by using faster camera. The current data can be plotted by 2D image (like shown in Figure3.2(C-F)) and it also can be plotted in 3D surface plotting which may give better view of relative current density (shown in Figure3.3).

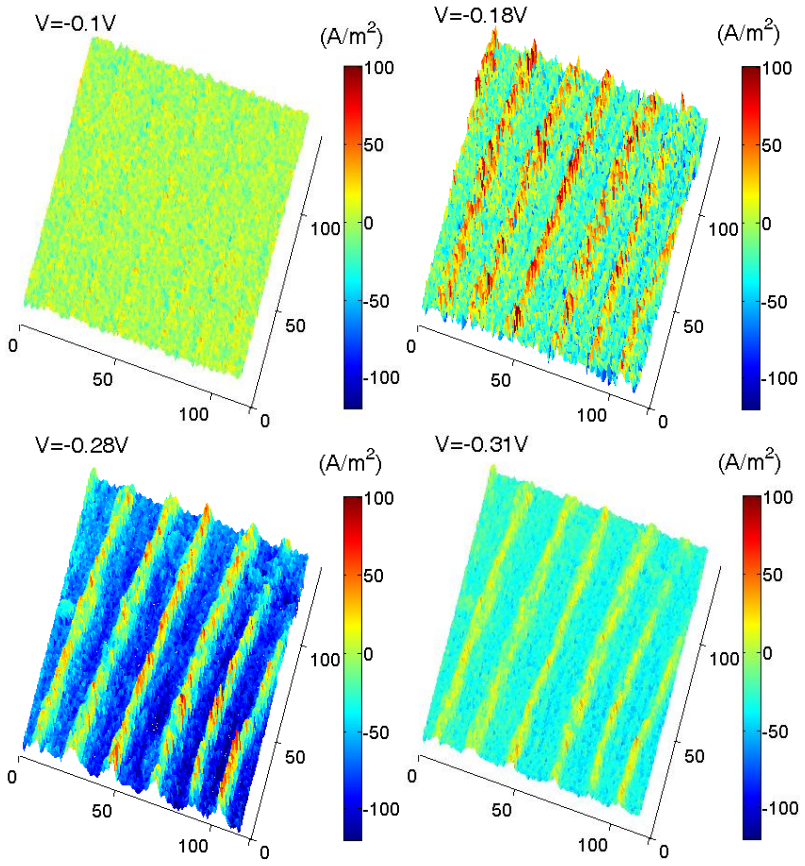

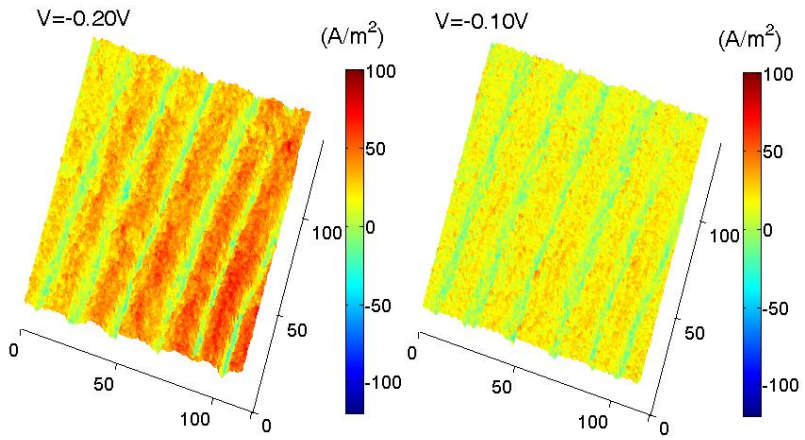

Figure 3.3. 3D PECI current image. Electrochemical current density map at different potentials. Replot of Figure 3.2 C-F.

The contrast of the fingerprint revealed by the electrochemical current images arises from the blockade of the electrochemical reactions in the regions covered by the secretions from the finger. This interpretation is directly confirmed by the conventional SPR image acquired on the same electrode by switching off the potential (Figure 3.1A). The regions covered with the secretions are shown as positive contrast in the SPR image, from which the average thickness of the fingerprint is estimated to be ~2.5 nm. This thin layer of molecules blocks the electrochemical reaction of the redox molecules. The fact that conventional SPR images can also be obtained using the same optics provides additional values to the present electrochemical current imaging technique.

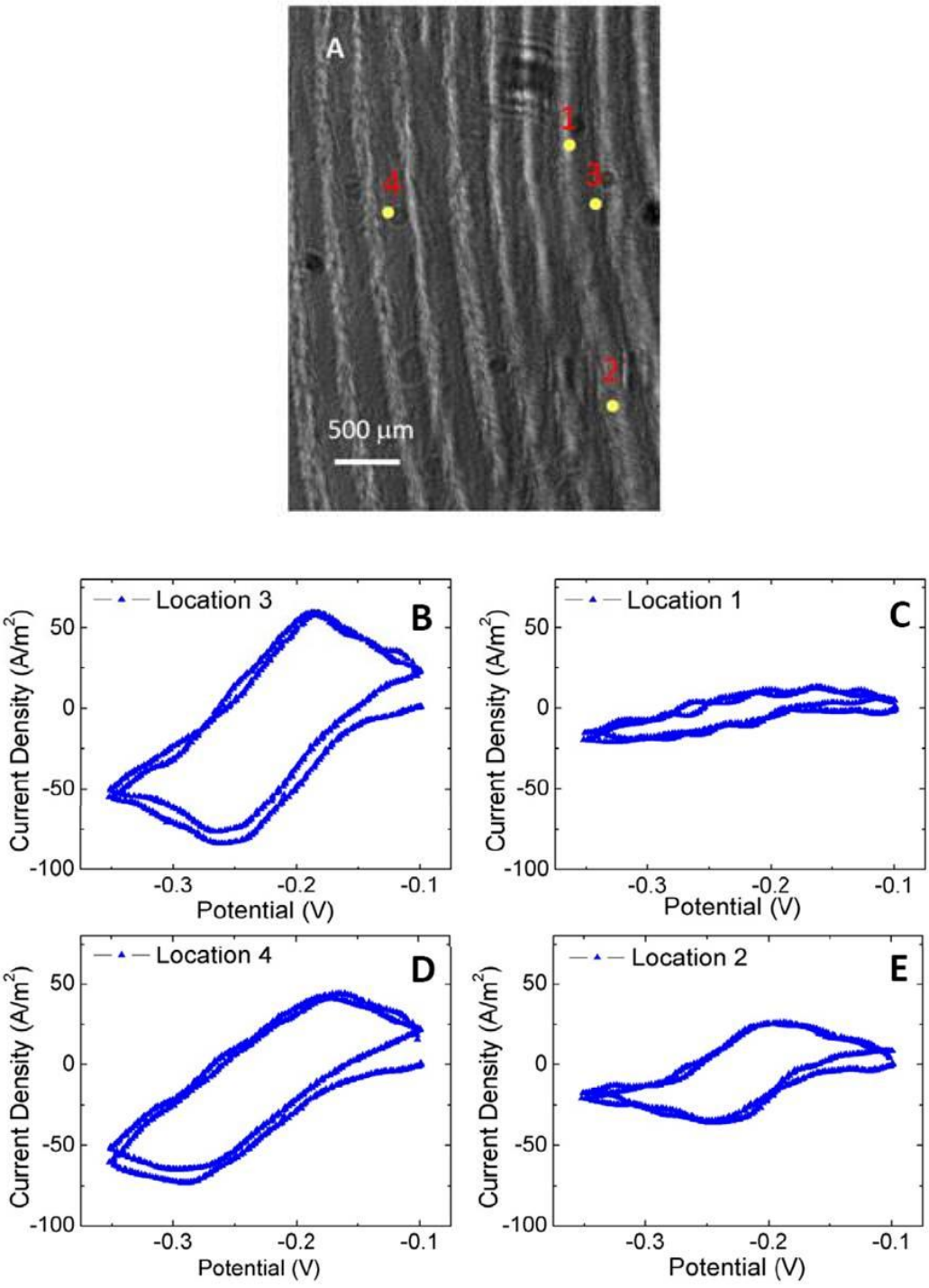

Figure 3.4. CV curves from different locations by PECI. (A) SPR image of a fingerprint. (B-E) Local cyclic voltammograms at different locations of the

surface. The electrolyte is 0.25M phosphate buffer containing 10 mM $Ru(NH_3)_6^{3+}$, and the potential sweep rate is 0.1 V/sec.

The snapshots in Figure 3.2, C to F, show only a small fraction of the information in the time and potential sequences of the electrochemical current image. At each point of the image, a local cyclic voltammogram can be readily obtained. Figures 3.4, B to E, show a few examples of local cyclic voltammograms at different locations marked on Figure 3.4 A. First, the voltammogram from a bare gold region shows a large electrochemical current with well-defined redox peaks (Figure 3.4B). In contrast, the voltammogram from a region covered with finger secretions shows only small background current with no obvious redox peaks (Figure 3.4C). Second, the voltammograms obtained from different regions of bare Au electrode also vary. For example, Figures. 3.4B and 3.4D are the voltammograms from two different Au regions. Although both display the well-defined redox peaks, the separations of the redox peaks are quite different, which is likely from the variation in the coverage of the secretions transferred from the finger. Finally, the voltammograms from different regions of the fingerprint are also different (Figures 3.4C and 3.4E), reflecting changes in the coverage of the finger secretions.

3.4 Trace particle analysis

The capability of imaging local electrochemical current has many applications, including trace analysis. As an example, the detection of traces of TNT has been demonstrated here[46]. TNT has a very low vapor pressure and

often presents in the form of particulates. A small TNT particle may be visualized with an optical microscope, but it is difficult to distinguish it from dusts or other airborne particulate matter. TNT is known to undergo electrochemical reductions at certain potentials, which has led to the detection of TNT using electrochemical method [47]. However, if the amount of TNT particulates is small, it is difficult to detect them using the conventional electrochemical detection methods that measure the total current from the entire electrode.

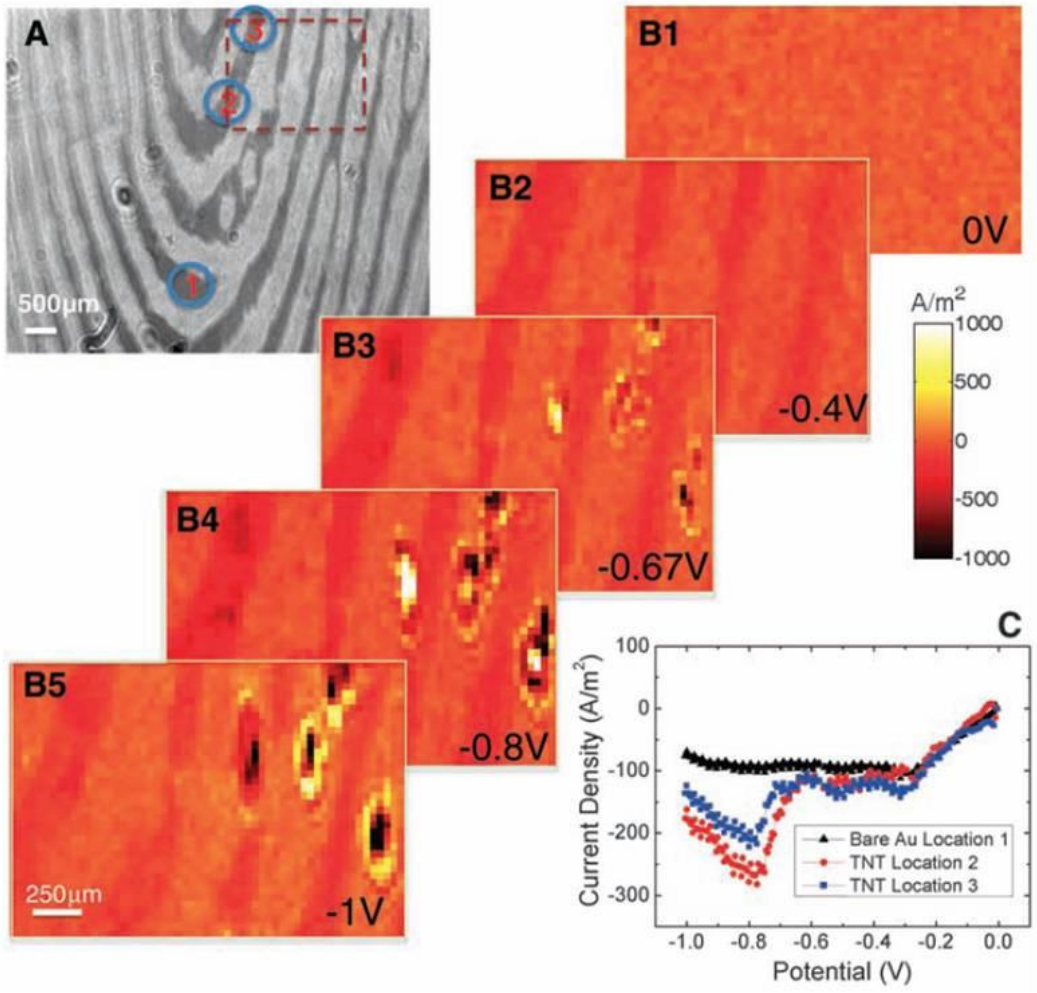

Figure 3.5. Detection of TNT traces on a fingerprint by PECI. (A) SPR image of a fingerprint. (B1-5) Snapshots recorded while sweeping the potential negatively

from 0 to -1.0 V at a rate of 0.05 V/sec. The appearance of the "spots" is due to the reduction of TNT particulates. (C) Local voltammograms of the regions with (blue and red dots) and without (black dots) TNT particulates. The electrolyte is 0.5 M KCl.

A sample including a fingerprint and TNT particulates on the electrode surface was prepared. Although the fingerprint is visible in the SPR image, the TNT particulates could not be resolved (Figure 3.5A). The electrochemical current image of the surface was recorded while cycling the potential. Figures.3.5 B1-B5 show several snapshots at different potentials. At 0 V, the electrochemical current image shows a uniform surface with no contrast for either the fingerprint or the TNT particulates because no electrochemical reactions takes place at this potential (Figure 3.5 B1). Sweeping the potential toward negative values, contrast of the fingerprint begins to show up (Figure 3.5 B2) from the reduction of dissolved oxygen gas in the electrolyte, which results in different electrochemical currents in the regions with and without the fingerprint secretions. At this point, it is still difficult to resolve features due to the TNT particulates. Lowering the potential further toward the reduction potential of TNT, "spots" in the electrochemical current image associated with the reduction of the TNT particulates begin to appear (Figures 3.5 B3-5), which allows me to detect and indentify the individual TNT particulates.

By selecting regions where "spots" appear, local voltammograms were obtained, showing peaks from the reduction of TNT (Figure 3.5 C). For comparison, a local voltammogram from a region without TNT is also shown

(black dots). Note that the TNT peak shapes and positions are not exactly the same as those in the cyclic voltammograms of TNT dissolved in an electrolyte as measured by the conventional electrochemical method.[48] The difference may arise from differences in the mass transport between two experiments. From the integrated area of the reduction current peak at -0.8 V shown in the local voltammograms (Figure 3.5 C), the mass of the corresponding TNT particulate is estimated to be as small as ~0.5 ng (for an area of 50 μm x 50 μm). Because the current detection limit is ~0.3 pA (see below), the estimated detection limit is 0.3 fg. 3D plots of electrochemical current images of fingerprint with TNT trace particles is shown in Figure3.6. It is really easy to distinguish the current difference between fingerprint and TNT trace particles. Each sharp peak locates one of TNT trace particle in Figure3.6 C and D.

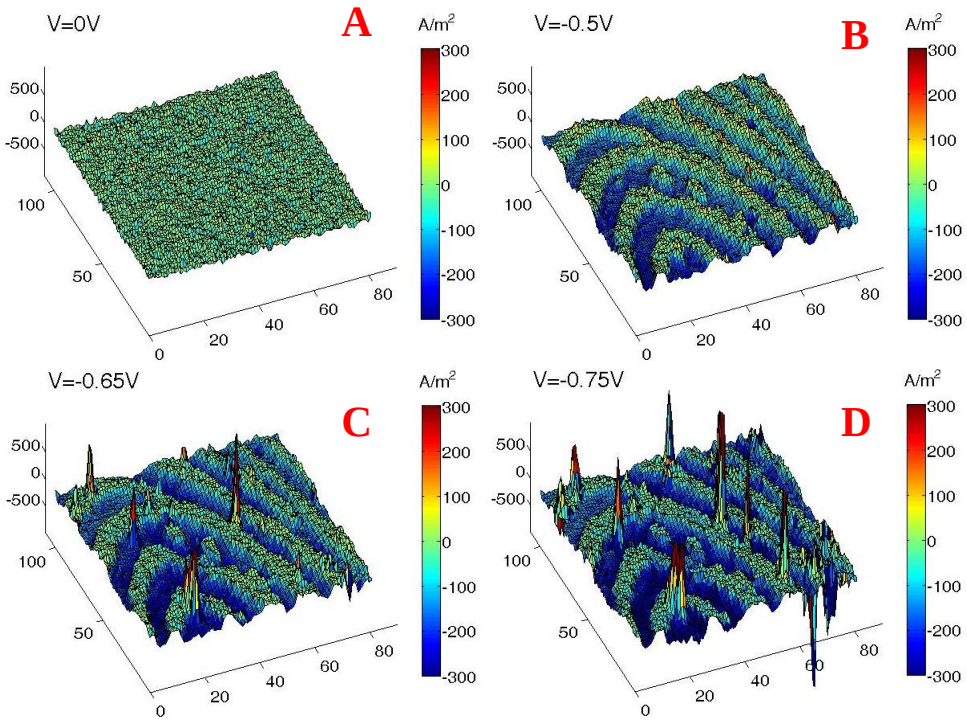

Figure 3.6. 3D plots of PECI images of TNT particles with fingerprint. The sharp peaks show the locations of trace particle.

The voltammogram of the surface was recorded by using the conventional electrochemical method and did not observe the distinctive reduction peaks of TNT (Figure 3.7); the TNT signal was washed out by the large background current from areas without TNT. In contrast, the present electrochemical imaging technique obtains the local voltammograms of the particulate regions, which eliminates the background current contribution from other regions to the measured signal. The capability of performing local electrochemical analysis on the regions of interest (determined by the image) also reduces potential interference in electrochemical analysis. For instance, the large electrochemical reduction peak of the dissolved oxygen, a known source of interference taking place over the entire electrode surface, does not substantially affect the local voltammogram of a small particulate region.

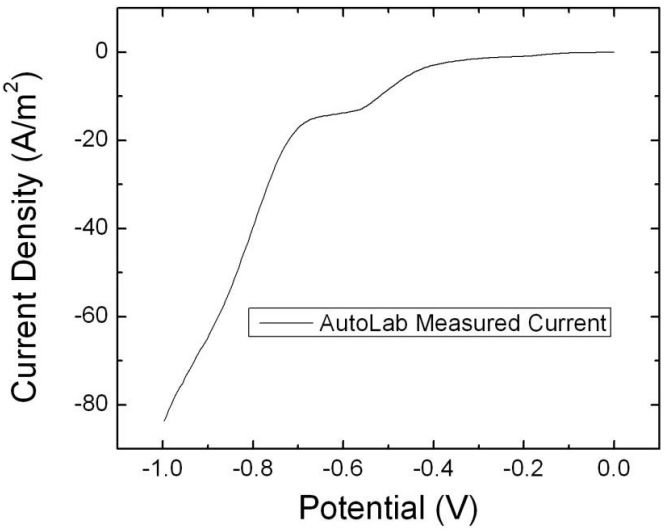

Figure 3.7. Conventional CV of TNT on fingerprint. The potential sweep rate: 0.05 V/sec. Electrolyte: 0.5 M KCl.

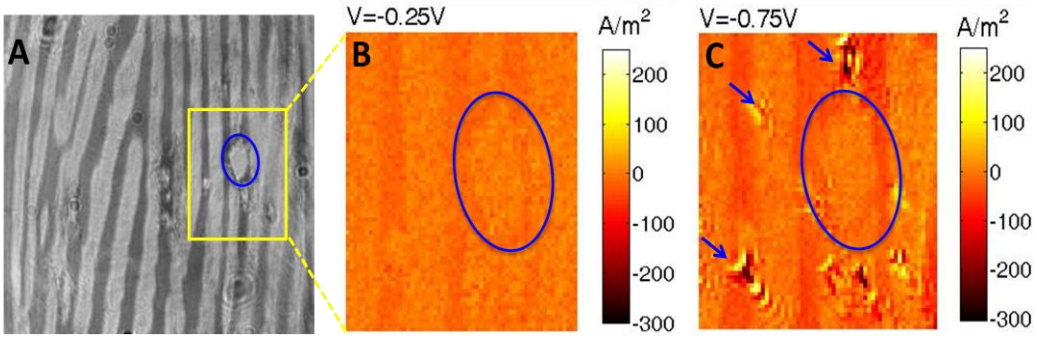

Figure 3.8. Detection of TNT particulates in the presence of wax particles. (A) SPR image of TNT + wax particulates (marked by a blue circle) on fingerprint. (B-C) Electrochemical current image at different potential (-0.25V and -0.7V).

Conventional optical imaging techniques, including SPR, can resolve small particles, but they usually cannot reveal the chemical identities of the particles. To further demonstrate the capability of trace chemical analysis with the imaging technique, other particulate matter is introduced, such as candle wax, onto the fingerprint in the presence of TNT particulates. The regions of the wax particulates show little contrast changes with the potential (marked by black arrows) while the regions containing TNT particulates show large and characteristic changes. The conventional SPR can image but cannot distinguish the two types of particles (Figure 3.8). However, the electrochemical current image shows the distinct contrast changes in the regions of TNT particulates associated with the electrochemical reduction.

3.5 Spatial resolution and current detection limit

The spatial resolution along the surface plasmon propagation direction is limited by the propagation length, which depends on the wavelength of light. For 638 nm, the length is ~3.1 μm, and for 532 nm, the length decreases to 0.2 μm.[44] In the direction perpendicular to the surface plasmon propagation, the resolution is limited by the optical diffraction limit, which is about 0.19 μm using an objective with numerical aperture of 1.65. An electrochemical current imaging of a 1-hexadecanethiol-patterned electrode created by PDMS (polydimethylsiloxane) contact print[49] is shown in Figure 3.9A, where the current contrast arises from the variation in the coverage of the self-assembled monolayer. The local voltammogram from a region (0.25 μm × 3 μm) covered with densely packed 1-hexadecanethiol Au area shows little current (black line Figure 3.9B). In contrast, the voltammogram from a region without covering of 1-hexadecanethiol (0.25 μm × 3 μm) shows well-defined redox peaks that are separated with ~60 mV, as expected for a reversible redox reaction (red line, Figure 3.9B). In contrast, the simultaneously recorded voltammogram with the conventional electrochemical method shows distorted redox peaks caused by averaging of different reactions over the entire electrode (Figure 3.9C).

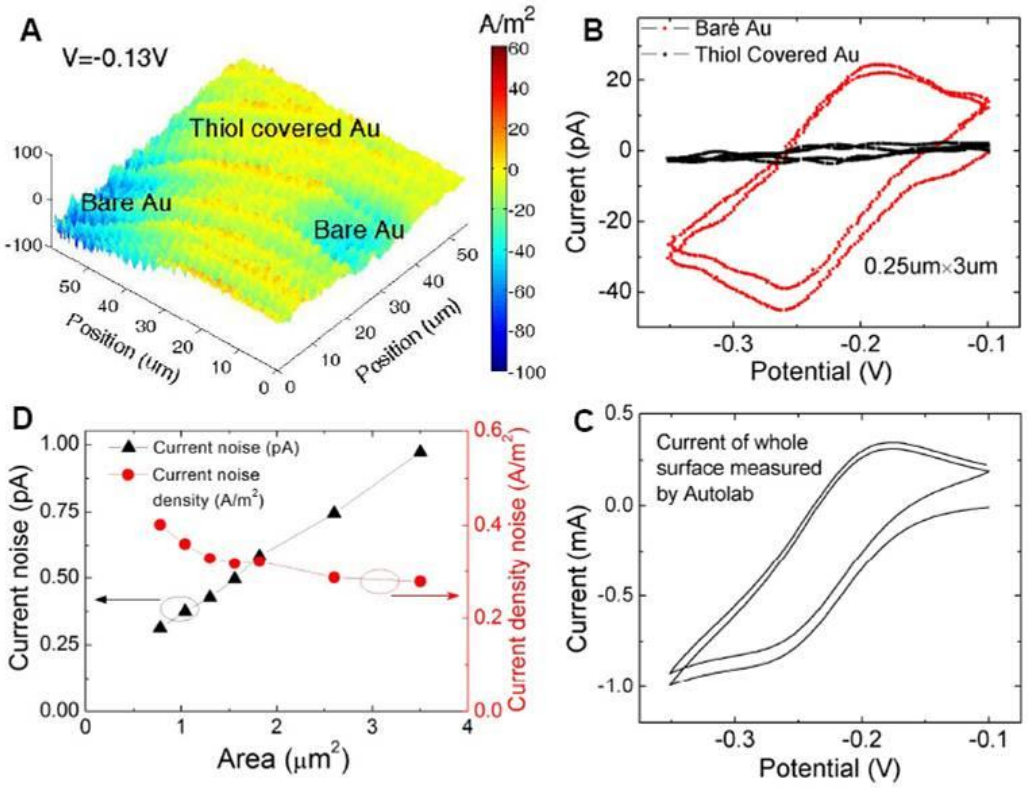

Figure 3.9. Spatial resolution and current detection limit of PECI. (A) Electrochemical current image of 1-hexadecanethiol self-assembled on a Au electrode in 0.25 M phosphate buffer containing 10 mM $Ru(NH_3)_6^{3+}$, where the blue regions (negative current) are due to the reduction of $Ru(NH_3)_6^{3+}$. (B) Cyclic voltammograms of regions covered with densely packed (black lines) and exposed gold (red lines) regions. (C) Cyclic voltammogram obtained with the conventional electrochemical method (that measured the current over the entire electrode surface). (D). Dependence of current and current density noises on the area of detection.

This imaging technique measures light intensity, corresponding to current density, which does not decrease with the size of an imaged area, so high spatial resolution does not compromise the current detection limit. As shown in Figure

3.9D, the noise level in the current density (red circles) does not change much with the area, so the noise in the current decreases with the area (black triangles). The smallest meaningful area is determined by the spatial resolution, which is about 0.2 um by 3 um. The noise from such a small region in our present setup is about 0.3 pA. This level of current noise is excellent comparing to other electrochemical detection methods, typically pA-nA, and could be further optimized by improving the light source and CCD detector. The electrode used here is gold, and other metal electrodes (e.g., Ag, Cu and Pt) can also be used. Just like the current-based electrochemical detections, an electrochemical reaction is always accompanied by a change in the chemical species, so the electrochemical current imaging technique described here is universal.

This chapter has shown that the electrochemical current microscopy described here provides more sensitive and selective trace analysis than conventional electrochemical methods. It is capable of providing local voltammetry, amperometry and other electrochemical techniques. This technique offers unique features to study various heterogeneous electrochemical reactions, including enzyme amplified biosensors, DNA and protein microarrays, and local activities of cells. In addition to non-invasive and fast parallel imaging, it also allows for simultaneous conventional SPR imaging, adding extra information to the interpretation of the data.

CHAPTER 4

ELECTROCHEMICAL IMAGING AND CHARACTERIZATION OF GRAPHENE BY PECI

4.1 Introduction

Graphene is a single-atom thick, two dimensional sheet of sp^2 bonded carbon atoms arranged in a honeycomb crystal lattice and can be thought of as composed of benzene rings stripped out from their hydrogen atoms. These freestanding two dimensional materials were presumed not to exist, until discovered experimentally in 2004[50]. Graphene is the building blocks for graphitic materials of all other dimensionalities (Figure4.1) [50]. In addition to its planar state (2D), graphene can be stacked into three dimensional (3D) graphite in which graphene layers are weakly coupled by van der Waals forces (means more than 10 layers normally), 'rolled' into one dimensional (1D) carbon nanotubes (CNTs), it can also be 'wrapped' into zero dimensional (0D) spherical buckyballs. A single layer graphene corresponds to single-walled carbon nanotube (SWCNT) while graphene nanoplatelets (consist of between two and ten graphene sheets stacked upon one another) are equivaqlent to the multi_walled carbon nanotubes (MWCNTs) whereby they are composed of a few layers.

Graphene captured the interest and imagination of physicist and chemists due to their unique electronics[51], optical[52], mechanical[53], thermal[54], and electrochemical (EC) properties[55]. It is the thinnest known material in the universe and the strongest ever measured[56]. The most explored area of

graphene is its electronic properties, and graphene exhibits many unique properties because it is a truly 2D electron system. Electrons propagate through the honeycomb lattice of graphene without any effective mass, which results in quansi-particles that are described by A Dirac-like equation rather than the Schrodinger equation[56, 57] and are therefore called Dirac Fermions. Grpahene's charge carriers have giant intrinsic mobility, with zero effective mass, can travel for micrometers without scattering at room temperature. To study and describe graphene's electronic properties, quantum electrodynamics (QED) must be applied. Many phenomena predicted by QED has been observed in graphene, such as non-zero minimum conductivity[58], anomalous Quantum Hall Effect[59] (QHE), the Klein Paradox[60], and $\pi\alpha$ white light adsorption[52], and many of them observed even in room temperature.

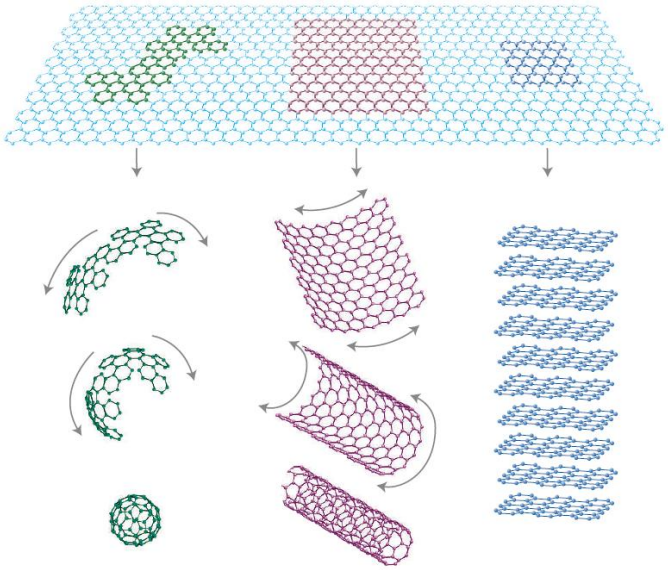

Figure 4.1. Graphene: the building block of all graphitic forms. (a) 0D fullerene; (b) 1D carbon nanotube; (c) 3D graphite. From ref. [50].

In addition to the unique electronic properties of graphene, it also holds great promise for many applications in the field of electrochemistry. One of the advantages of graphene as an electrode material is its big surface area, which is important in applications such as energy storage, biocatalytic devices, and sensors[61]. Theoretical calculated graphene surface area is 2630 m^2g^{-1}, which is two times larger than that of CNTs (1315 m^2g^{-1}), and much bigger than that of graphite (~10m^2g^{-1}). Furthermore, graphene has excellent conductivity (~64 mS cm^{-1}) which is approximately 60 times more than that of SWCNTs. Graphene sheets are flexible as opposite to brittle graphite. Electrochemical properties of graphene are similar to those of CNTs, however graphene has huge advantage over CNTs, that it does not contain heterogeneous materials like metal nanoparticle which will dominate the EC reaction.

Many electrochemical applications of graphene have been developed based on its unique properties. Graphene has made an impact within the application of energy storage. Electrochemical super-capacitors of graphene based materials have been demonstrated[55], which has potential for passive and static electrical energy storage devices for applications such as portable electronics and hybrid cars. Energy is stored in ultracapacitors because of the formation of electrical double layer at the interface of graphene[55]. It has shown huge theoretical and practical advantages, such as a high surface area, excellent conductivity and capacitance, relative low production costs. Also there are a number of techniques have been shown for sensing purpose by using graphene to modify electrode. For example, graphene modified electrodes have been used

within biosensing as a glucose sensor[62], dopamine detection[63] and immunosensor[64]. People also reported the electro-catalytic sensing of paracetamol using graphene electrode[65].

Most graphene used in electrochemistry are produced with chemical or thermal reduction of graphite oxide (GO), because it is mass-production method. Graphene from GO reduction usually has abundant structural defects, wrinkles and functional groups[66]. All the graphene sheets are curled and twisted together and formed small pieces and particles. Then this material is used to modify the electrode, which generates huge electrode surface area. Figure 4.2 shows the SEM and TEM pictures of graphene which is used as electrode materials, note that all the graphene in pictures is reduced from GO. By using graphene modified electrode, people can obtain high electrode surface which gives high energy storage density and high sensitivity.

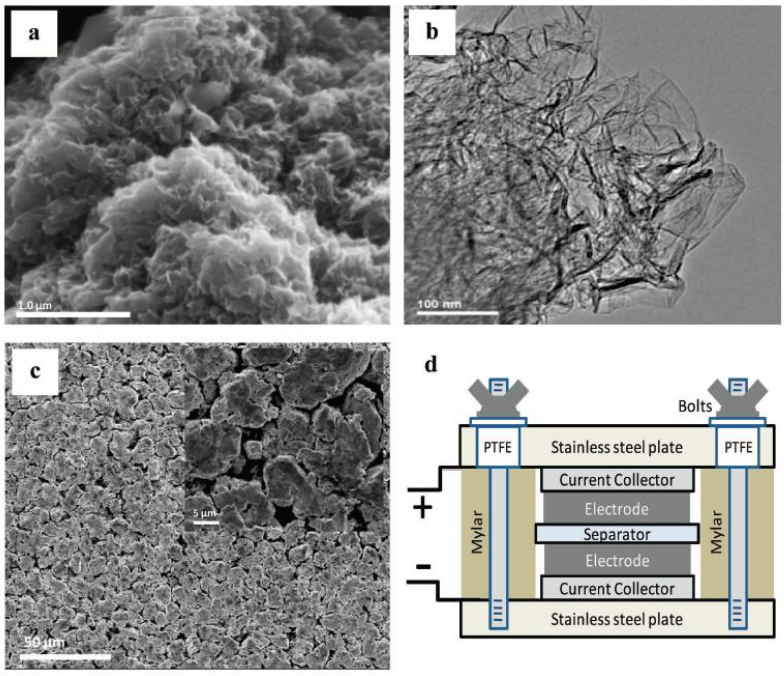

Figure 4.2. EC applications of graphene: super capacitor. (a)SEM image of chemical modified graphene (CMG) particle surface, (b) TEM image showing individual graphene sheets extending from CMG particle surface, (c) low and high (inset) SEM images of CMG particle electrode surface, (d) schematic of test cell. From ref. [55] .

In most of electrochemical applications of graphene, people use a large amount of graphene wrinkled clusters and particles as materials rather than a single piece of flat graphene sheet. The measurement result reflects an average effect of huge graphene surface area, it does not illuminate any local EC reaction information. To discover the intrinsic electrochemical properties of graphene, EC reaction current distribution of single piece graphene should be measured. Also it has been claimed that defects play an important role in the electrochemistry of highly oriented pyrolytic graphite (HOPG) electrode (Figure 4.3), where an increased density of exposed edge plain has been correlated with faster heterogeneous electron transfer kinetics[67, 68]. The electron transfer rate at HOPG edge plane is significantly faster than that at the basal plane, thus a few percent of edge plane defects will result in a significant change in EC reaction. Many efforts has been down on trying to prove this phenomenon, including covered the edge with passive material[69], laser activate[70] or electrochemical pretreat the electrode surface[71]. But all these methods are not directly measurements, since it is difficult to measure the heterogeneous current distribution through a single piece of conductive electrode surface. Therefore, a local electrochemical reaction current image is needed for a flat graphene piece.

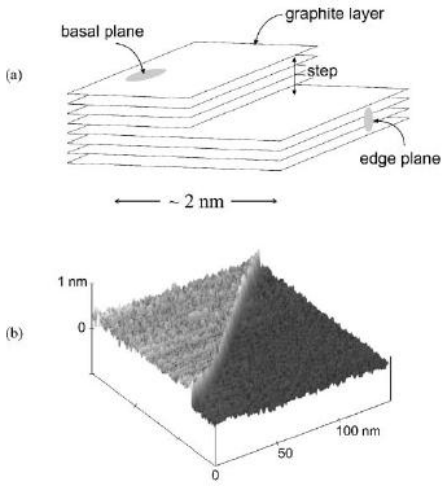

Figure 4.3. Edge effect of graphite. (a)Schematic diagram of a 4 layer step edge. (b) SEM image of a monolayer step on a HOPOG surface. From ref. [67].

As shown in Chapter 3, the EC SPR has ability to image local electrochemical reaction current in a very small area (spatial detection limit can be 0.2um by 0.2um under green light illumination). Therefore it is perfectly to use this technique for the research of graphene electrochemical properties. In this chapter, this method has been applied to thin graphene piece to measure the electrochemical current of graphene. First of all, SPR microscope is used to image the thin graphene layers (single and double) and characterize the thickness of graphene by scan SPR angle. This is first time to utilize SPR to image graphene, and this measurement reflects and verifies the refractive index of thin graphene material. Second, PECI method is used to measure the local electrochemical current distribution of graphene caused by redox couples $Fe(CN)_6^{3-/4-}$. Two voltage scan methods are applied, one is normal cyclic voltammetry (CV) scan,

another is to apply a periodic sine wave around standard electrode potential at different frequency.

4.2 Graphene thickness characterization by SPR

4.2.1 Existing technique to characterize graphene

Before doing any research of graphene, identification of layer number (single, double, or multilayer) of graphene and its location is extremely important. One of important reasons why researchers could not find graphene before 2004 is because they could not find an easy and suitable method to indentify single layer graphene. There are three types of methods using now to identify and characterize the graphene. First method is to use optical microscope image the graphene flake on top of 300nm or 90nm SiO_2/Si substrate, this method is based on the interference effect between thin graphene layer and substrate layer. Different layers of graphene will have different color and contrast, which is shown in Figure 4.4 (a).[72, 73] Secondly, Raman spectrum is a good and fast way to characterize the graphene because it allows one to infer the number of layers (up to the screening length) in a "fingerprint" fashion (Figure 4.4 (b-d)).[74] The main features of graphite and graphene's Raman spectrum are the G band at ~1584 cm^{-1} and 2D band at ~2700 cm^{-1}. The differences between G band and 2D band are: the 2D peak of single layer graphene can be fitted by a single peak, while that of double layer graphene cannot. The difference between double layer and thicker graphene is double layer graphene's 2D band has a significant secondary peak at ~2650 cm^{-1} (514nm).[74] The third method is scanning prove microscope,

including atomic force microscopes (AFMs)[75], scanning tunneling microscopy (STM)[76] and transmission electron microscope (TEM)[77] (Figure 4.4 (e) (f) and (g)).

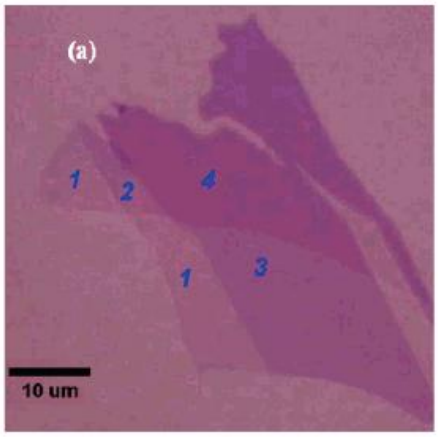

(a)

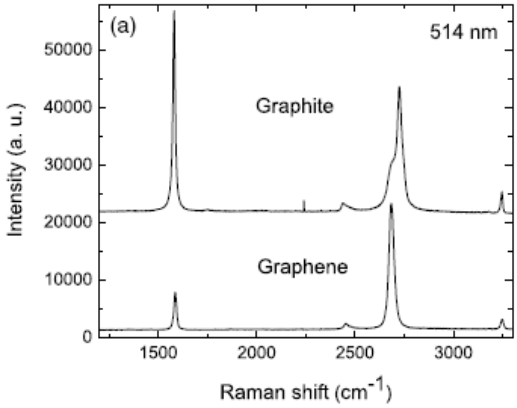

(b)

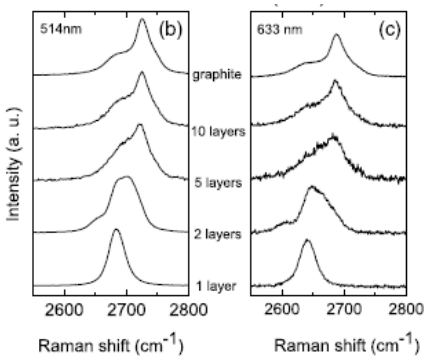

(c)

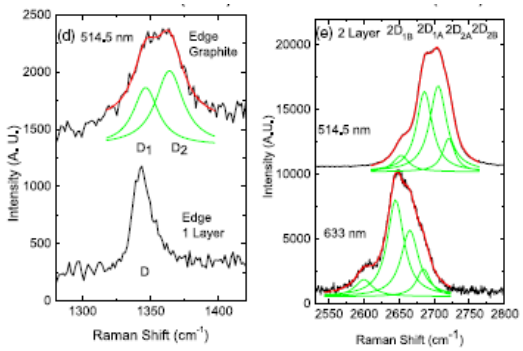

(d)

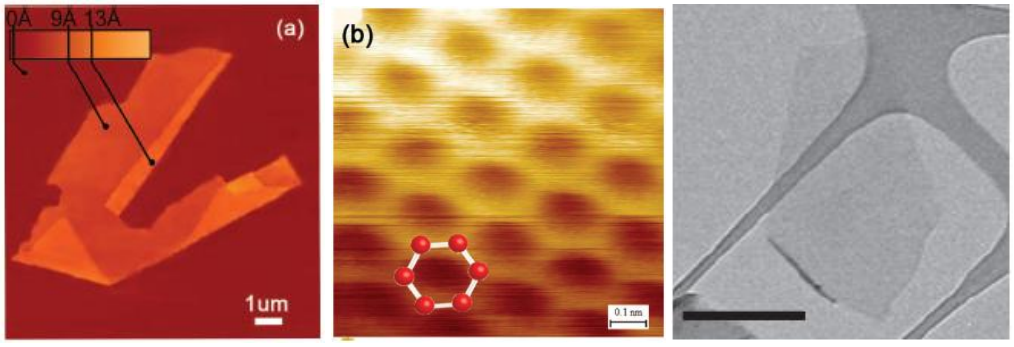

(e) (f) (g)

Figure 4.4. Regular methods to characterize graphene. (a) graphene image on top of 300nm SiO_2/Si substrate. [72, 73] (b) Raman spectrum of graphite and graphene. [74] (c) 2D band of different layers graphene.[74] (d) Raman spectrum of single and double layer graphene. [74] (e) AFM image of graphene. [75] (f) STM image of graphene. [76] (g) TEM image of graphene. [77]

Although the graphene characterization and identification methods are well developed, they still have drawbacks. The optical microscope method is good to identify the graphene and help researcher have a rough idea of layers of graphene. Raman spectrum is needed to assure the thickness of graphene. For Raman method, the difference between 3 layers to 10 layers and up is not very obviously and to obtain the Raman image of graphene piece need long time and speed is slow. The third method SPM also has relative slow throughput, and they are neither destructive nor need special sample preparation.

Since SPR is a technique have very high sensitivity for the refractive index (RI) change near surface (less than about 200nm for red light 632nm), it should be sensitive to detect and image the thin graphene layer on Au surface. Most method measure or characterize graphene on 300nm SiO2/Si substrate, they are difficult to measure the graphene on top of electrode. While SPR gives an alternative choice which it can measure the RI change on the Au electrode.

4.2.2 Graphene characterization by SPR microscope

To observe graphene thin flake there are two main challenge: first, thin graphene flake generated by mechanical exfoliation is relative small. Size of graphene is typical about 5 to 20μm, although people have obtained up to 100μm

size graphene by mechanical exfoliation, but it is really difficult and need many practices and some luck. Based on 5μm to 20μm size, it is impossible to be observed by prism SPR setup since the maximum zoom of prism setup is only 10X. Second challenge is graphene does not have good contrast on top of Au surface (SPR surface). Normally graphene was mechanically exfoliated on top of 300nm SiO_2/Si subtrate which will give good contrast to different layer of graphene. For the first challenge the SPR microscope setup is imploied which has been explained in Chapter 3 and Chapter 8 (Figure 8.1). For SPR microscope setup, the spatial resolution can be defraction limit (~0.2μm) on perpendicular direction to the plane of incident. Along the incident light direction the spatial resolution could be about 0.2μm for green light and ~3μm for red light (670nm).

47nm thick Au with 1.5nm thick Cr adhesion layer was evaporate in cleanroom under high vacuum (3e-6 Torr). Before the sample preparation, the Au chips were cleaned by H_2 flame and this also make the Au surface hydrophilic which was good for graphene's adhesion to Au surface. Then the standard mechanical exfoliation process was applied to bare Au chip. A blue tape with thin graphene flake by peeling off thick graphite piece multiple times was press on Au surface. By carefully separating the blue tape with Au substrate, some thin graphene pieces would stay on Au surface. Then the Au chip was cleaned 3 times by ethanol and water. Nitrogen flow was used to dry the Au chips. By using upright microscope, thin graphene pieces were located and then Raman spectroscopy was used to indentify the thickness of graphene layer. Finally, the

Au chips with thin graphene flake was move to SPR microscope setup and angle scan and electrochemical SPR experiments were carried out.

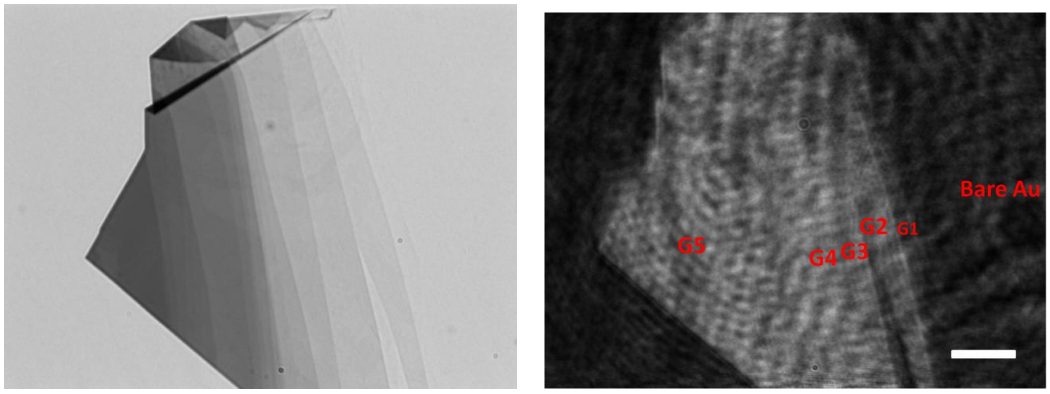

(a) (b)

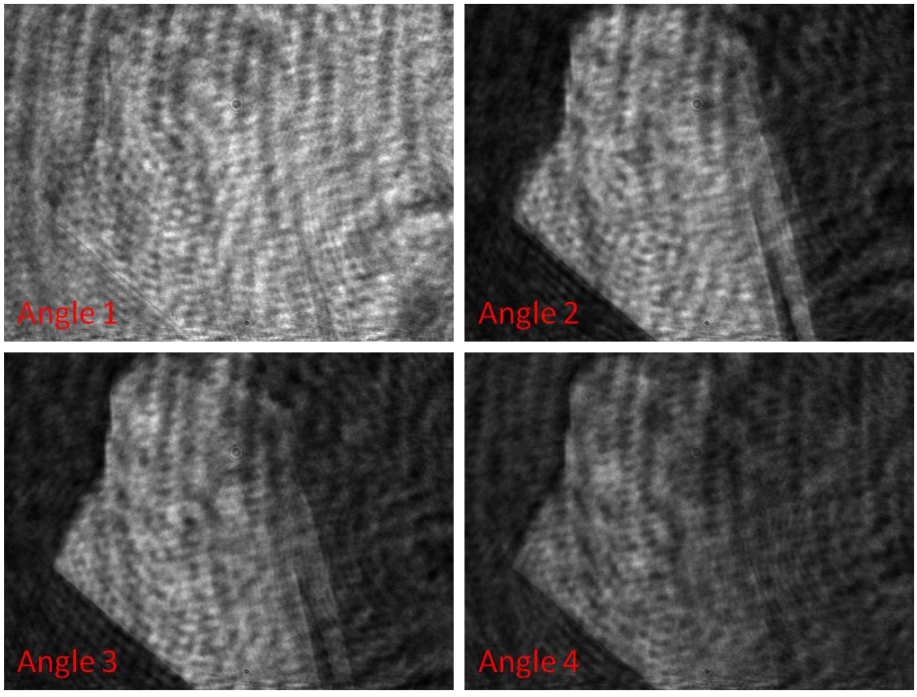

(c)

Figure 4.5. SPR images of different layers graphene. (a) Transmitted image of thick graphene layer on top of Au surface. (b) SPR image of same piece of graphene with (a) illuminated by green light (534.5nm). G1 to G5 are locations of

different thickness of graphene and with bare Au they are correspond to the Figure 4.6 (a) and (c)'s SPR response curves. The scale bar in the image is 10μm. (c) SPR image of same graphene with (a) and (b) at different angle. Angle 1 to 4 is labeled in the Figure 4.6 (a).

Figure 4.5 (a) shows a transmitted image of a thick graphene layer, it has different thickness at different locations. The SPR image of same piece graphene with Figure 4.5(a) is shown in Figure 4.5(b), the illumination light is green light with 534.5nm wavelength. Thick graphene piece is in the air that means no solution or water is on top of graphene. In the image, G1 to G5 are labeled for different graphene location (different thickness), and bare Au is also labeled in the image. There is big contrast between bare Au and graphene layers. Most part of graphene has similar intensity which is because SPR reponse of graphene G3 to G5 are saturated with the angle I chose, it can be explained better with Figure 4.6 (a). When SPR angle is scaned, the contrast between different thick graphene areas and bare Au area should change. Figure 4.5(c) includes four different SPR images at different angles. Angle 1 to 4 are pointed out in Figure 4.6 (a). Note that the SPR images show many fringes due to the interference on the optical path way of microscope. And it will change when the angle is scanned since angle will change the optical pathway while some wave length (red light) have smaller effect and some have bigger effect (green light), which will be shown next.

Figure 4.6 (a) exhibits the SPR response (reflectivity) of different thickness graphene and bare Au when the incident light angle scans from 40 degree to 52 degree. Green light is used and graphene is illuminated in air.

Location G1 to G5 and bare Au are pointed out in Figure 4.5 (b). In this figure, the bare Au response (black line) matchs with simualted bare Au response (green line) quite well. Thinest graphene area G1 (red line) is the curve that is most close to the bare Au response. As graphene thickness increases, the reflectivity curve more and more shallow. “1” to “4” marks the angles corresponding with SPR images of Figure 4.5 (c). At angle “1”, reflectivity does not have difference for all the locations of graphene and bare Au, thus the image in Figure 4.5(c) angle 1 shows no contrast at all. At angle “2”, bare Au and graphene area G1 and G2 have big difference on reflectivity, but rest of area G3 to G5 does not have obvious difference. Therefore the image in Figure 4.5(c) Angle 2 shows good contrast on bare Au and G1 G2 areas, does not show many contrast among G3 to G5. At angle “3”, reflectivity difference between G1 and bare Au is really small, so bare Au cannot be distinguished with G1 in angle “3” image. At angle “4”, G1 to G3 and bare Au have similar reflectivity, while the image of angle “4” shows they cannot be distinguished among these areas.

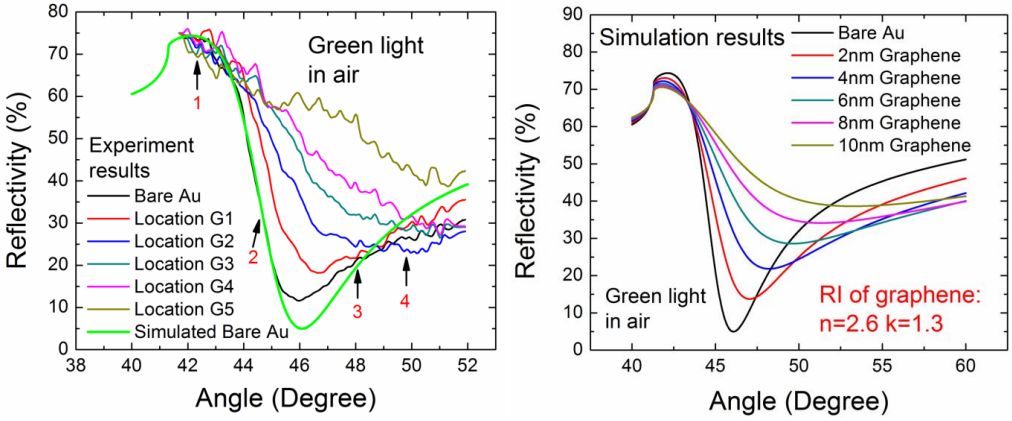

(a) (b)

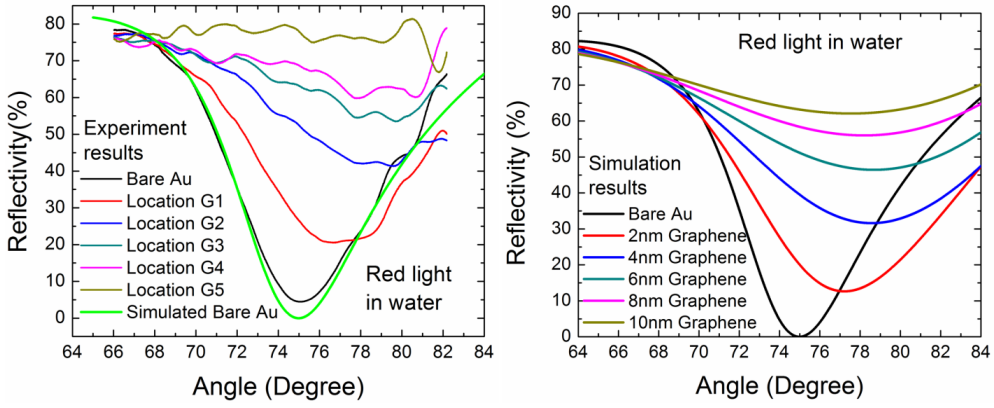

(c) (d)

Figure 4.6. SPR reflectivity of different layers graphene. (a) SPR response (reflectivity) of different thickness graphene (G1 to G5) and bare Au at different angles. The incident light is green light and graphene is in the air. Locations of G1 to G5 and bare Au are illuminated in Figure 4.5 (b). "1" to "4" are the angles corresponding with SPR images of Figure 4.5 (c). (b) Simulation curves of SPR response of different thickness graphene (from 0 to 10nm at 2nm step) at different angles. (c) SPR response at different angles of graphene in red light in water. (d) Simulated graphene (0nm to 10nm at 2nm step) SPR response at different angles with red light in water.

Simulation results of different thickness of graphene on Au chip was calculated by Winspall (an SPR response simulation software). Although the acturally thickness of graphene can not be measured by Raman spectrum, the thickness of graphene has been estimated and 5 values is chosen from 0nm to 10nm at 2nm step. Since graphene is semi metal, therefore the refractive index of graphene has imaginary part, the value used in simulation is n = 2.6 and k =1.3 [73]. By comparing Figure 4.6 (b) with (a), the experiment results match with

simulation results very well. First the minimum dip angle shift to the right with thicker graphene and the curves become shallower with increasing thickness. Second the curves start at same point and finish at similar reflectivity at ~ 52 degree, this also correspond very well with simulation results. Third, the relation of different curves in region from 48 degree to 52 degree also similar to the simulation results. Note that there are many small kinks in some of the experiment curves which is due to the interference pattern (fringes) moves when the incident angle is changing. This proves our SPR measruement is reasonable and does reflect the refractive index of graphene. Figure 4.6 (c) and (d) are similar with (a) and (b) except the incident light is red (680nm) and sample graphene is in the DI water with a PDMS well to hold the solution. Basically same phenomenon was observed, the simulation results match with experiment results very well.

As shown before, the spatial resolution of SPR depends also on the incident light wavelength. Figure 4.7 shows the difference of SPR image for same piece graphene at different wavelength. Figure 4.6 (a) and (c) are illuminated by red light (680nm) while (b) and (d) are illuminated by green light (534.5nm). (a) and (b) are same area and (c) and (d) are same piece of graphene. Image Figure 4.7 (a) and (c) exhibit very long tails along the incident light direction (from bottom to top of image) which is due to the propagation length of surface plasmon oscillation. (a) is even longer than (c) which is because image (a) is taken in air which has longer tail while (c) is taken in water (which has shorter tail). At same time, since the green light has much shorter propagation length (~0.25μm), the image Figure 4.7 (b) and (d) are much sharper than (a) and (c) especially along

the incident light direction (from bottom to top). Many details can be resolved through green light image, for example image Figure 4.7 (d) can display small features of graphene which cannot be seen from (c).

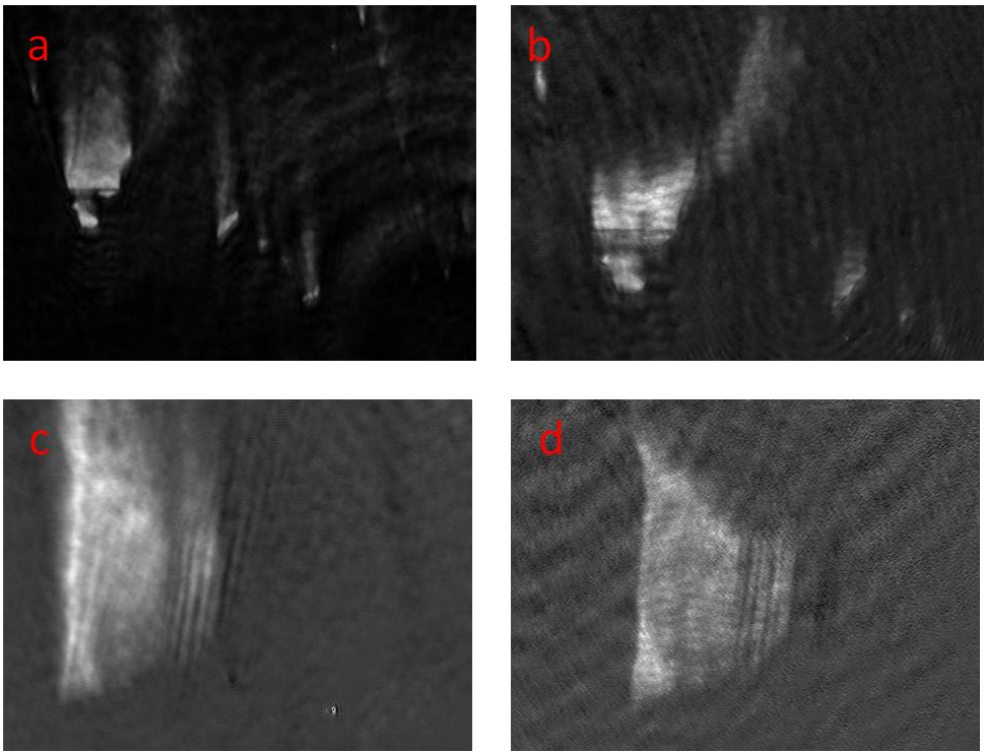

Figure 4.7. SPR image of single and double layer graphene. (a) SPR image of graphene illuminated by red light (680nm) in air. (b) SPR image of same graphene with (a) illuminated by green light (534.5nm) in air. (c) (d) Same piece of graphene illuminated by red light in water and green light in air respectively.

Figure 4.8 shows single layer of graphene on top of Au surface. Figure 4.8 (a) and (b) are both transmitted image taken by upright microscope, while the image (b) is enhanced contrast of image (a). Single layer graphene piece is pointed out by the red color arrow in the figures. SPR image of same piece of graphene are shown in Figure 4.8 (c) and (d), image (d) was obtained by

subtraction of (c) from another substrate area which does not have graphene but have similar interference pattern. The most important part of fringe source is from the optical pathway rather than the interface between oil immersed microscope objective and substrate and the moving of substrate does not affect the interference pattern a lot. Therefore, the Figure 4.8 (d) has much clearly boundary than Figure 4.8 (c). Figure 4.8 (d) shows that SPR image technique has enough sensitivity or contrast to distinguish single layer graphene from substrate.

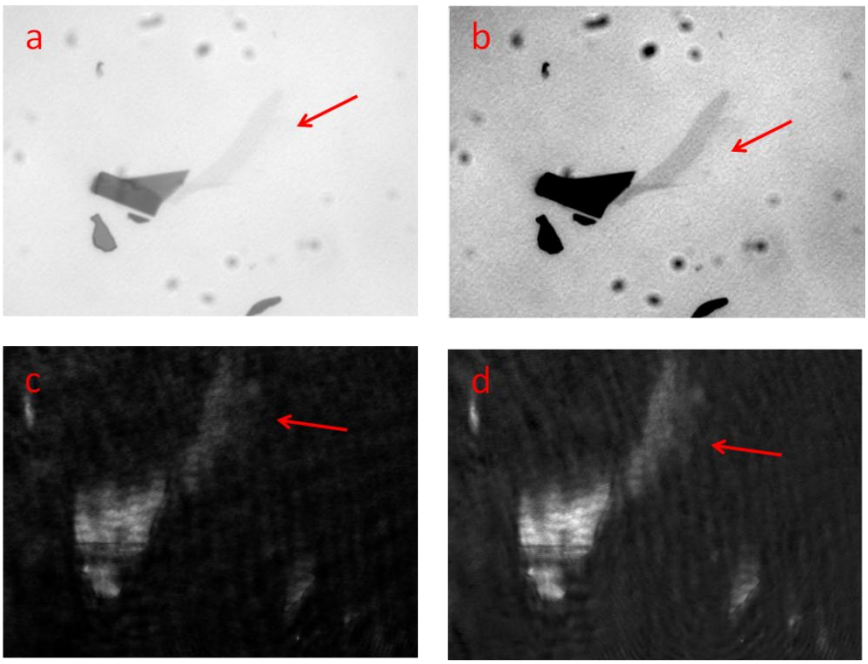

Figure 4.8. Transmitted and SPR images of single layer graphene. (a) Transmitted image of single layer graphene (pointed out by red arrow) by upright microscope. (b) Enhanced contrast image of (a). (c) SPR image of same single layer graphene by green light in air. (d) SPR image with subtraction of background interference pattern illuminated by green light in air.

Figure 4.9 (a) shows the Raman spectrum of single layer graphene shown in Figure 4.8. Since graphene is on top of Au, therefore the Raman spectrum in Figure 4.9 (a) is the sum of both single layer graphene (G and 2D band) and bare Au's Raman spectrum (Figure 4.9 (c)). From Figure 4.9 (a) the graphene measured is single layer since it has single 2D band peak and 2D band is much higher than G band. Figure 4.9 (b) shows the thick graphite on top of Au surface, since graphite is really thick while the light cannot penetrate through the graphite, the bare Au shape does not affect the spectrum in Figure 4.9 (b) (the base line of Raman spectrum is flat).

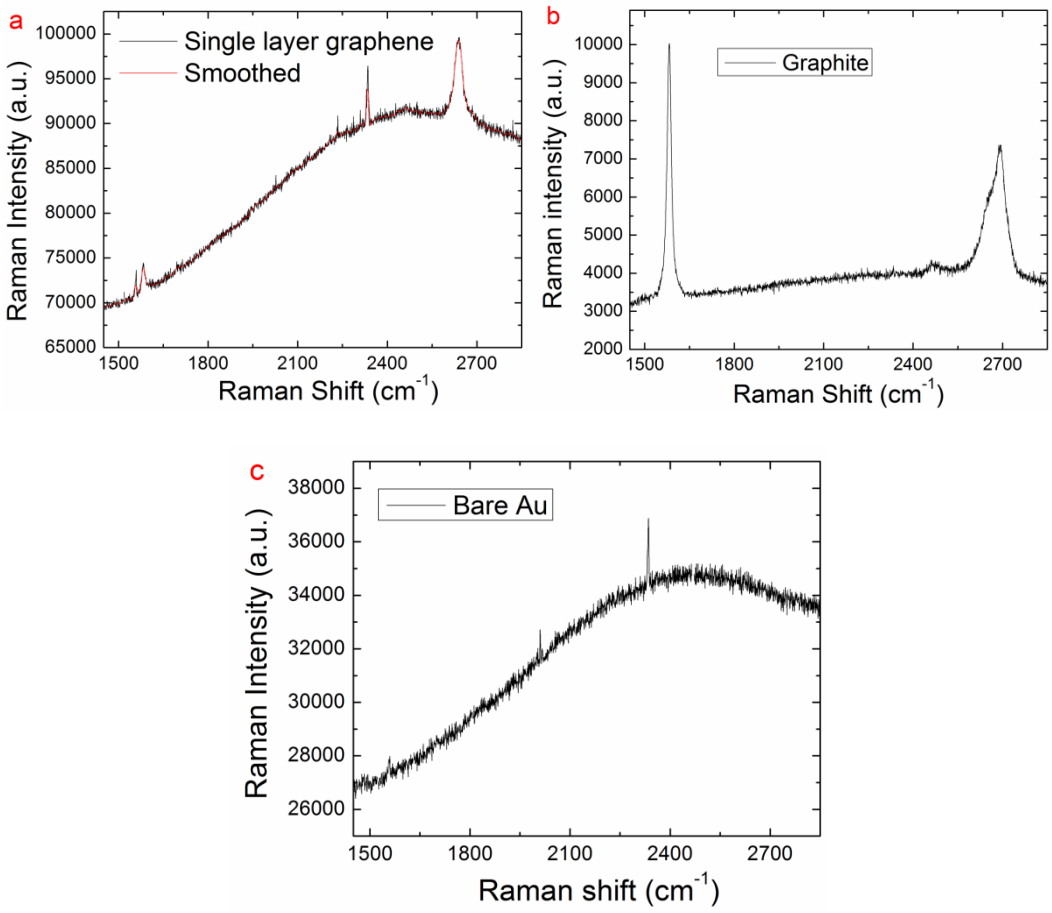

Figure 4.9. Raman spectrum of single layer graphene on Au. (a) single layer graphene on Au surface (47nm thick); (b) thick graphite piece; and (c) bare Au surface.

Figure 4.10 shows the reflectivity difference at different angles between bare Au and single layer graphene. Figure 4.10 (a) (b) and (c) are illuminated by 680nm (red) light in air, 680nm (red) light in 0.2M NaF solution and 534.5nm (green) light in air. The simulation response of bare Au and 0.66nm graphene on Au is also plotted in each figure. All three figures show the perfect matching between experiment data (bare Au and single layer graphene) and simulated data (bare Au and 0.66nm graphene). The reason why experiment result do not match the 0.335nm (single layer graphene's thickness) is because graphene may not have very strong contact with Au substrate. And this result correspond to the AFM height of single layer graphene very well which has typically ranged from 0.6 to 1.0 nm.[51] Figure 4.10 (a) and (b) have almost identical curves with simulation results which is due to less fringe effect with red light. However the Figure 4.10 (c) has much rough curve due to the fringe change in the scanning process.

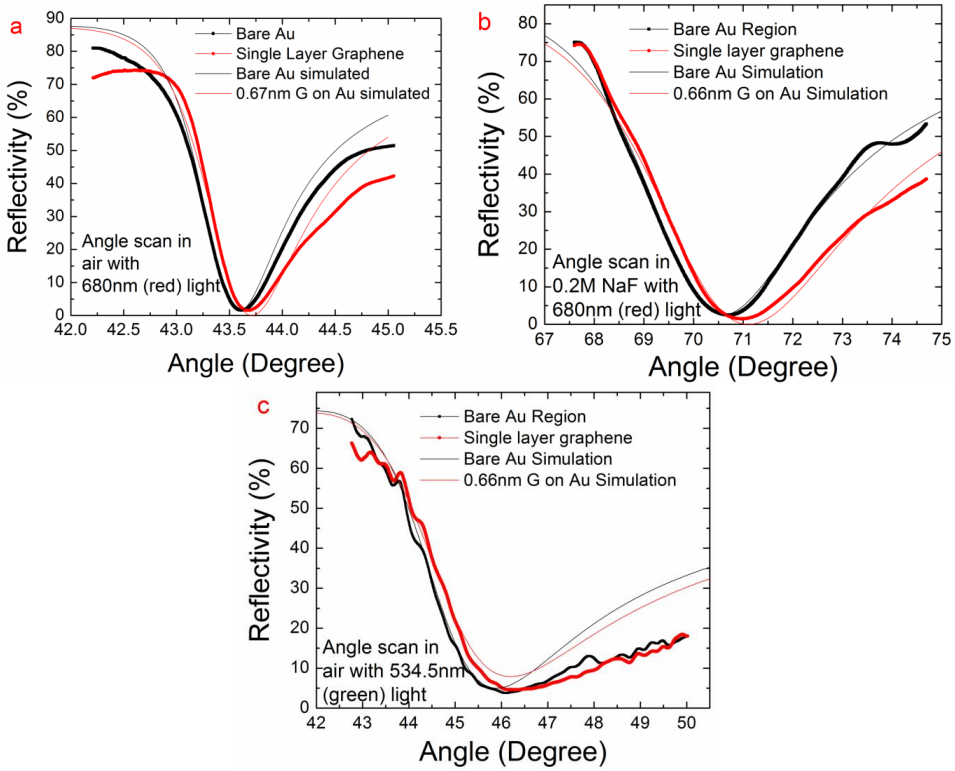

Figure 4.10. SPR Reflectivity of single layer. Angle is scanned with (a) red light (680nm) in air; (b) red light (680nm) in 0.2M NaF solution; and (c) green light (534.5nm) in air. Both experiment and simulated data is shown.

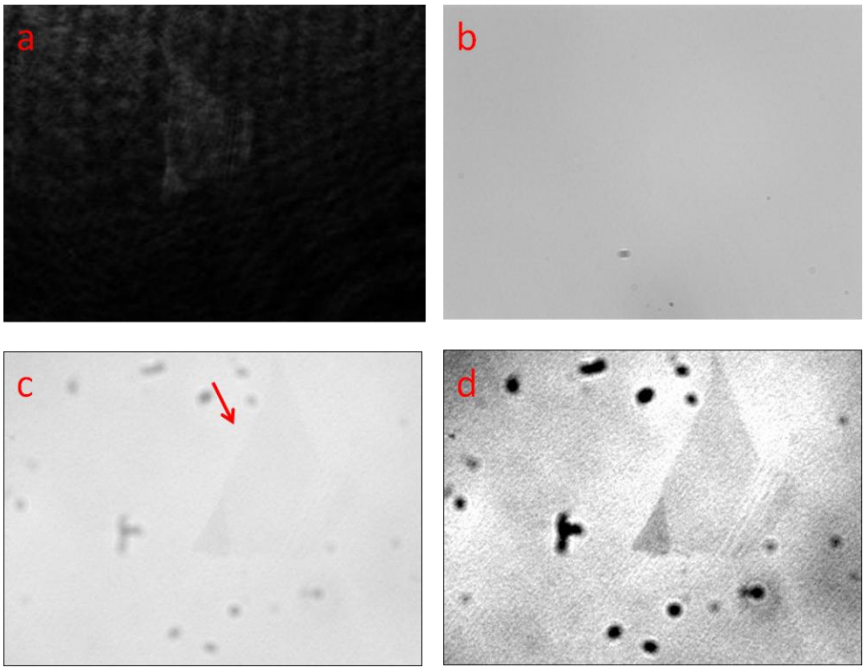

Figure 4.11. SPR and transmitted images of double layer graphene. (a) SPR image of double layer graphene. (b) Transmitted image of same double layer graphene taken by inverted microscope. (c) Transmitted image of double layer graphene taken by upright microscope, red arrow points out the location of graphene flake. (d) Enhanced contrast image of (c).

Figure 4.11 shows a double layer graphene piece (Raman data is shown next) image by SPR and transmitted image. It is impossible to see a single or double layer graphene on Au surface by inverted microscope (Figure 4.11 (b)), while upright microscope has better contrast compare with inverted. This is probably due to a little interference effect of graphene and Au substrate. Graphene can be only observed clearly by enhanced contrast image of (c) (Figure 4.11 (b)). Note that Figure 4.11 (a) is the direct SPR image without subtraction of fringe.

After subtraction, the SPR image of double layer graphene (Figure 4.7 (d)) is much more clear than transmitted image (Figure 4.11 (c)).

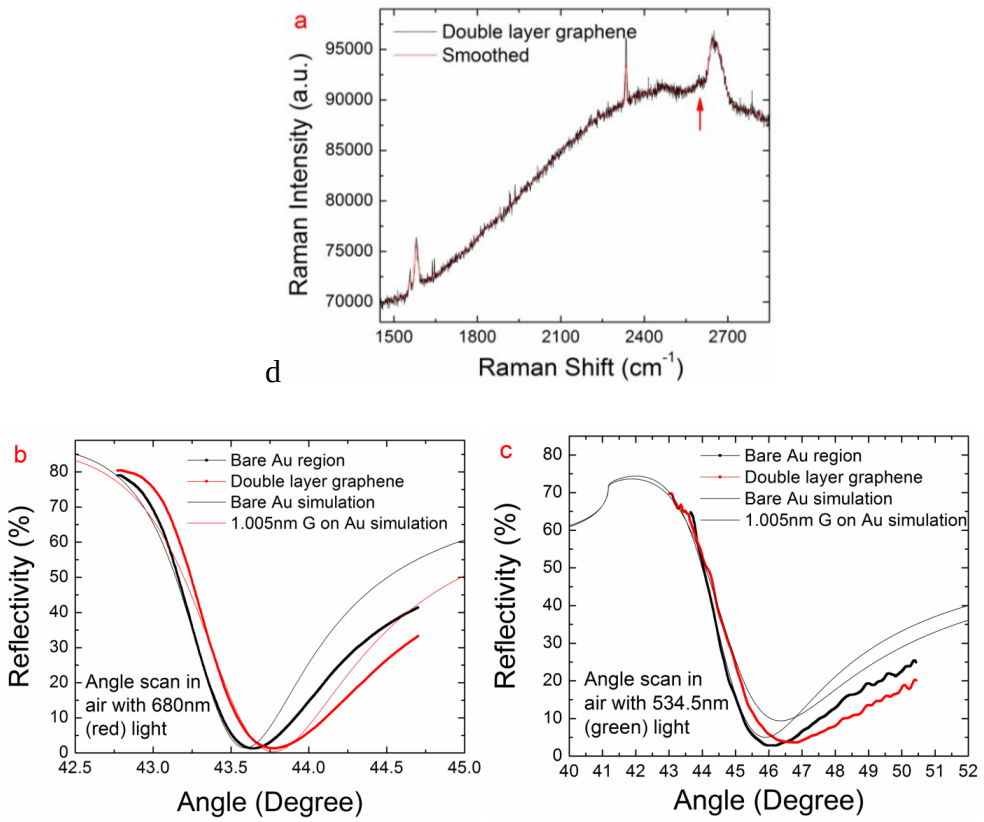

Figure 4.12. Raman spectrum and SPR reflectivity of double layer graphene. (a) Raman spectrum of double layer graphene flake in Figure 4.11, laser wavelength is 633nm. Reflectivity of double layer graphene and bare Au at different angle with (b) 680nm (red) light and (c) 534.5nm (green) light illumination. Both figure shows the simulated SPR response of bare Au and 1.005nm (3 layers) graphene on Au.

Small step at around 2600 cm^{-1} (Figure 4.12 (a)) shows the graphene piece in Figure 4.11 are double layer graphene. Figure 4.12 (b) and (c) are also the SPR angle scan curves which are matching very well with simulation response of bare

Au and 1.005nm (3 layers) graphene on Au results with both 680nm (red) light and 534.5nm (green) light in air. 1.005nm graphene is exactly 1 layer thicker than the single layer graphene's result (0.66nm). This means SPR has the sensitivity and ability to measure the single layer and double layer graphene.

4.3 Graphene PECI image by normal cyclic voltammetry

To evaluate the local electrochemical activity of graphene, PECI technique has been applied to image the electrochemical current of graphene on top of Au substrate. Ferricyanide redox couple $[Fe(CN)_6]^{3-}$ and $[Fe(CN)_6]^{4-}$ were chose with 0.2M NaF solution as electrolyte. Ferrocyanide was dissolved in 0.2M NaF solution with 10mM to 10mM ratio of K_4 $[Fe(CN)_6]$ and $K_3[Fe(CN)_6]$. A silver/silver chloride (Ag/AgCl) reference electrode (RE) was used and Pt wire was used as counter electrode (CE). Working electrode (WE) is the SPR sensing surface (Au film) with graphene flake on it. A normal EC cyclic voltammetry method was used with voltage range from -0.05V to +0.5V. Detailed process is described in Chapter 3, in brief SPR images were taken by Pike camera when potential is applied to SPR sensing surface. After subtraction the first image, the SPR response due to EC reaction is obtained and the SPR angle shift was calculated through the sensitivity calibration curve. By applying the reverse Laplace transfer, the current at each pixel is calculated at each frame.

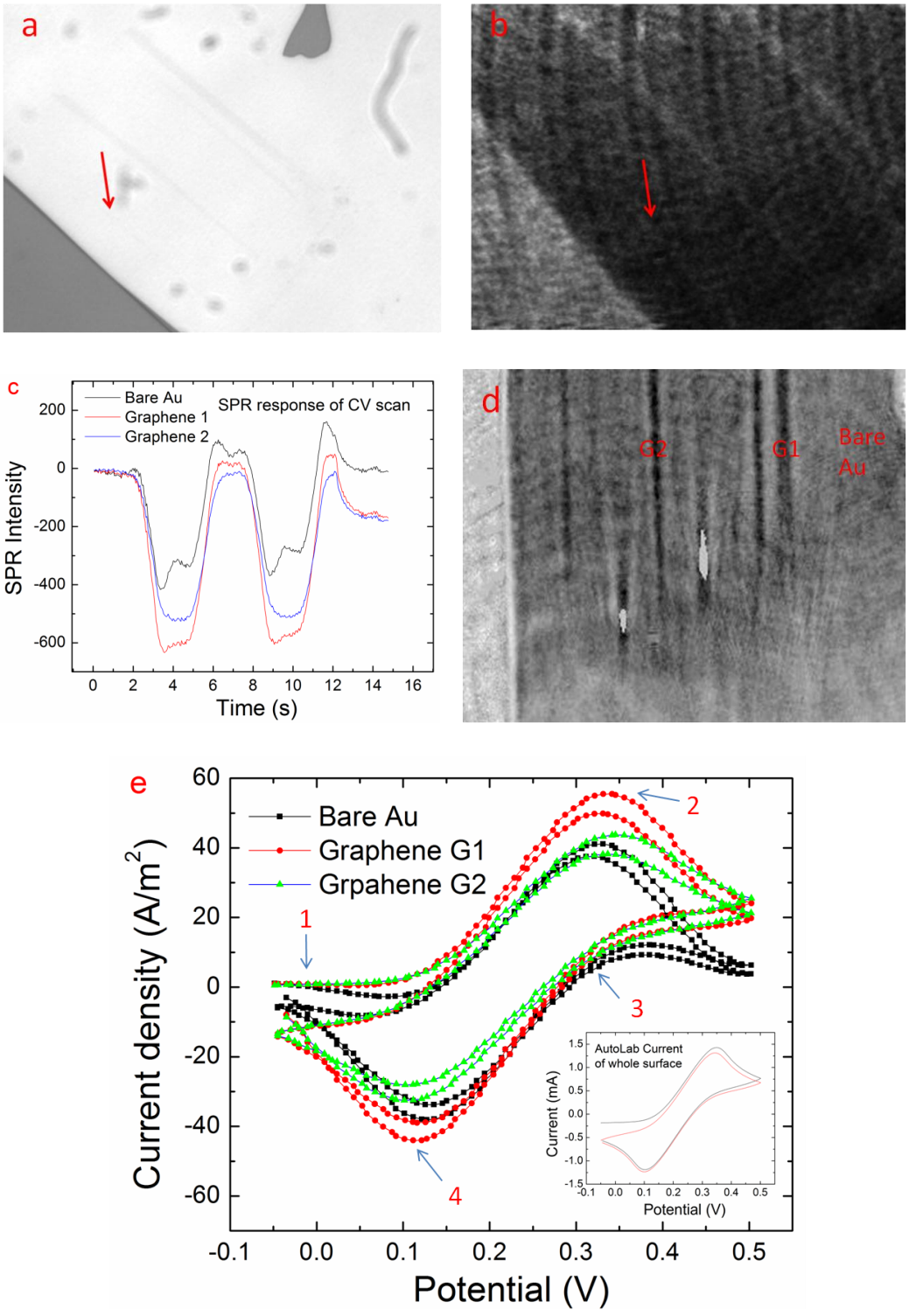

Figure 4.13. PECI current of graphene. (a) Transmitted image of graphene thin lines. (b) SPR image of same area of graphene with (a) illuminated by green light

in air. (c) SPR response at different locations, bare Au and two graphene locations. Locations are indicated in (d). (d) SPR response at certain potential about 0.1V during the CV scan. (e) Current calculated from SPR response at different locations. Locations are pointed out in (d). Inset is the CV current response measured by AutoLab.

Several thin graphene lines was found on Au surface. Figure 4.13 (a) (b) shows the transmitted image and the SPR image of same graphene area. The field of view in Figure 4.13(b) is 80 by 60μm. The normal CV scan was applied to this region and the SPR response at different locations (Grpahene location 1 and 2 and bare Au) are indicated in Figure 4.13 (d). Figure 4.13 (d) is the relative SPR intensity change due to the electrochemical reaction of $Fe(CN)_6$ molecules at potential +0.35V. From Figure 4.13 (c) the electrochemical current at different locations can be calculated (Figure 4.13 (e)). And the inset of Figure 4.13 (e) shows the current measured by Autolab potential stat in the same CV scan process. The big shape of current calculated from SPR have very good matching with the current measured by Autolab, while the Autolab current is the average effect of whole surface while the PECI current is the local current. That's why current at different location (Figure 3.14 (e)) does not 100% match with Autolab current curve. The peak height and peak location have slightly difference for different locations because the different surface condition and EC activity. The difference between graphene area and bare Au area is small while the graphene area has slightly bigger current which is possibly caused by the different charging effect between bare Au and graphene. The charging effect has reversed response with

$Fe(CN)_6$ molecules' EC reaction response. It means when potential increases the SPR response increases by the charging effect while SPR response decreases by the $Fe(CN)_6$ molecules' EC reaction. Bare Au has bigger charging effect than graphene area, therefore some of SPR response is canceled out by charging effect which caused the decreasing of current peak value and distort the current curve around -0.05V and +0.5V.

Figure 4.14 shows the EC current image of graphene area at different potential measured by PECI technique. The potential V1 to V4 is pointed out in Figure 4.13. First of all, at potential "1" and "3" the current is almost zero and relative change between graphene and bare Au is small, therefore there is no contrast in the image. At potential "2" and "4", the current is on the peak and the dip of the CV curve and bare Au has similar current with graphene area. Graphene area's current is a little higher than bare Au at potential "2" and a little lower than bare Au at potential "4", which matches the CV current curve in Figure 4.13 (e) very well. Since the big piece graphene on the left side of view is too thick to have SPR response, there is no current change in that area at different potentials. Note that there are brighter lines beside the graphene thin lines (in Figure 4.14 (b) and (d)), this means that line area has smaller current response. That phenomenon is optical effect at the boundary of graphene and bare Au that decreases SPR response.

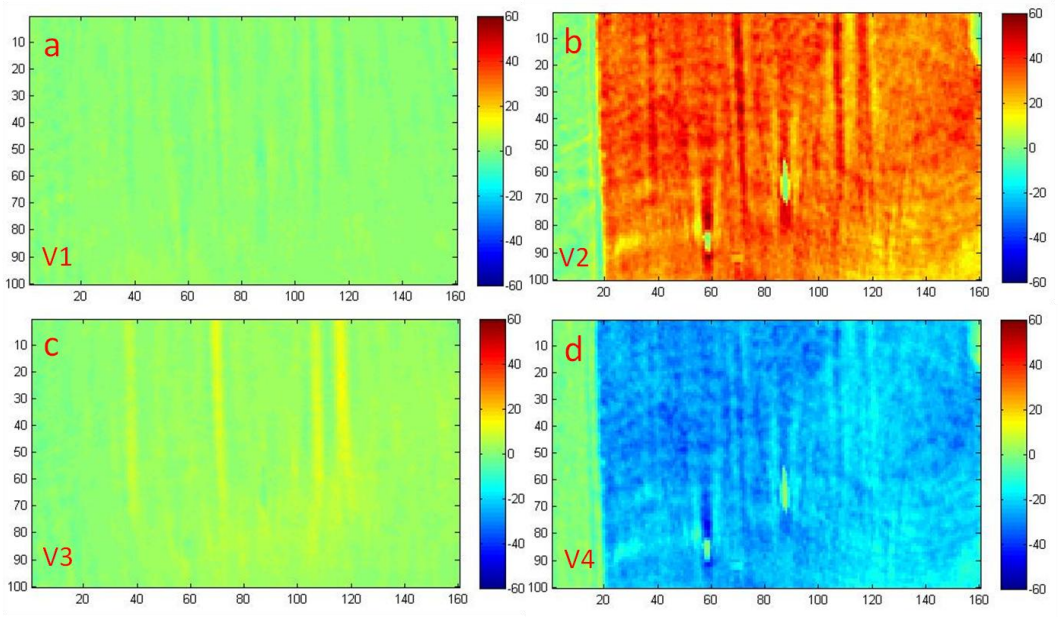

Figure 4.14. PECI images of graphene at different potential. The potential of figure (a) (b) (c) and (d) is V1 V2 V3 and V4 which is pointed out in Figure4.13 (e) with "1" "2" "3" and "4".

EC current image of another thin graphene layer was measured as well. Figure 4.15 (a) (b) (c) are the SPR, transmitted and enhanced transmitted images of the graphene area. SPR response at different locations are shown in Figure 4.15 (d) and the local EC current calculated from SPR response from (d) is plotted in Figure 4.15 (f), while the Figure 4.15 (e) is the current measured by Autolab potential stat. Current on bare Au surface has almost same response with current on the graphene area, and they both matches with current from Autolab very well. Figure 4.16 shows the EC current measured on double layer graphene (same piece with Figure 4.11 and 4.12). The response of bare Au and graphene also has similar response.

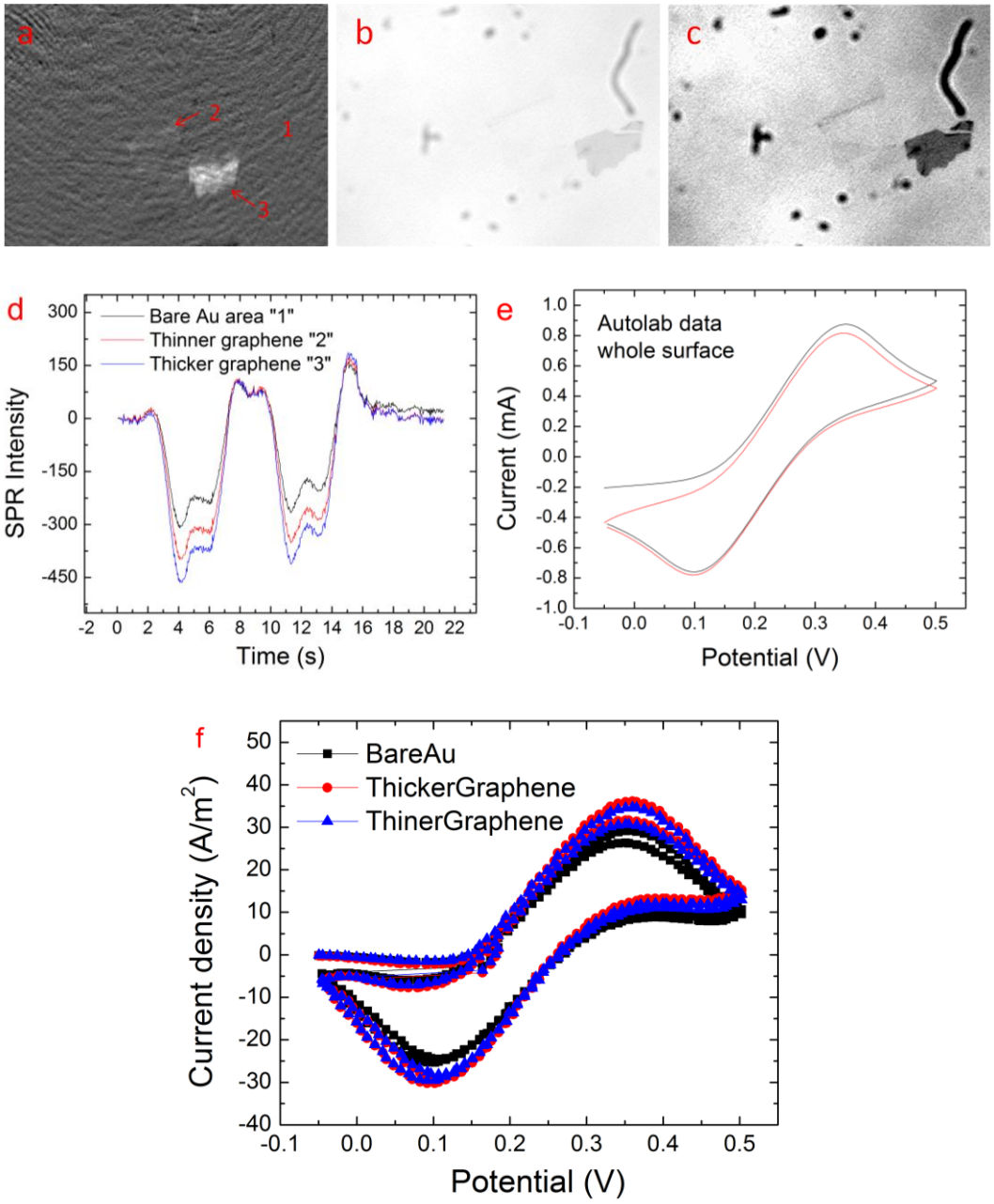

Figure 4.15. SPR and PECI current response of thin graphene. (a) (b) and (c) are SPR, transmitted and enhanced transmitted image of graphene flake. (d) shows the SPR response at different locations. Locations are pointed out in figure (a). (e) shows the Autolab current of the same process. (f) Electrochemical current at different locations calculated from SPR response in (d).

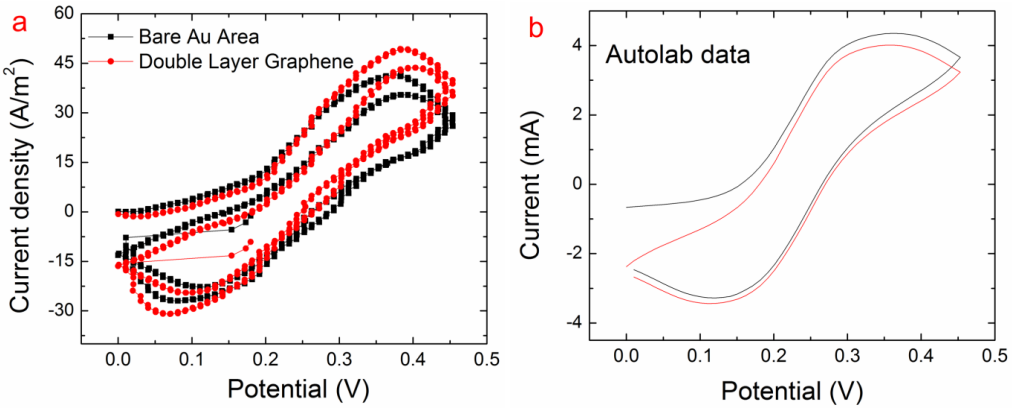

Figure 4.16. PECI CV of double layer graphene. (a) Electrochemical current measured by PECI on double layer graphene (the same graphene with Figure 4.11 and 4.12). (b) Autolab current from same process.

4.4 EC impedance image of graphene with redox molecules

In previous section PECI method has been applied to the normal CV scan to obtain the local current image of graphene. In this section impedance technique is used with redox molecules to evaluate the reactivity of graphene. Figure 4.17 shows the principle of this measurement. First, a standard electrode potential is applied to the Au electrode with graphene on it, and a sine wave at certain frequency is superimposed on the base of standard electrode potential (Figure 4.17 (a)). The voltage applied to the working electrode is plot in Figure 4.17 (b), where the standard electrode potential is about +0.22V and the peak to peak amplitude (Vpp) of sine wave is 0.1V, the frequency is 11Hz. In a reversible redox process, standard electrode potential means the oxidation and reduction has similar rate. When potential increase, there are more molecules oxidized than reduced, for $Fe(CN)_6$ molecule the SPR response will decrease like shown in

Figure 4.17 (b). When potential decrease, on the other hand, there are more molecules reduced than oxidized, SPR signal will increase. Therefore the SPR response is also a sine wave as long as SPR have linear relation with potential applied. From Figure 4.13 (c) and Figure 4.15 (d) by using small Vpp (less than 0.3V), a good linear relationship between potential and SPR response will be obtained around standard electrode potential. This is because in this voltage range, the concentration of redox molecules on the electrode is decided by the potential applied to electrode.

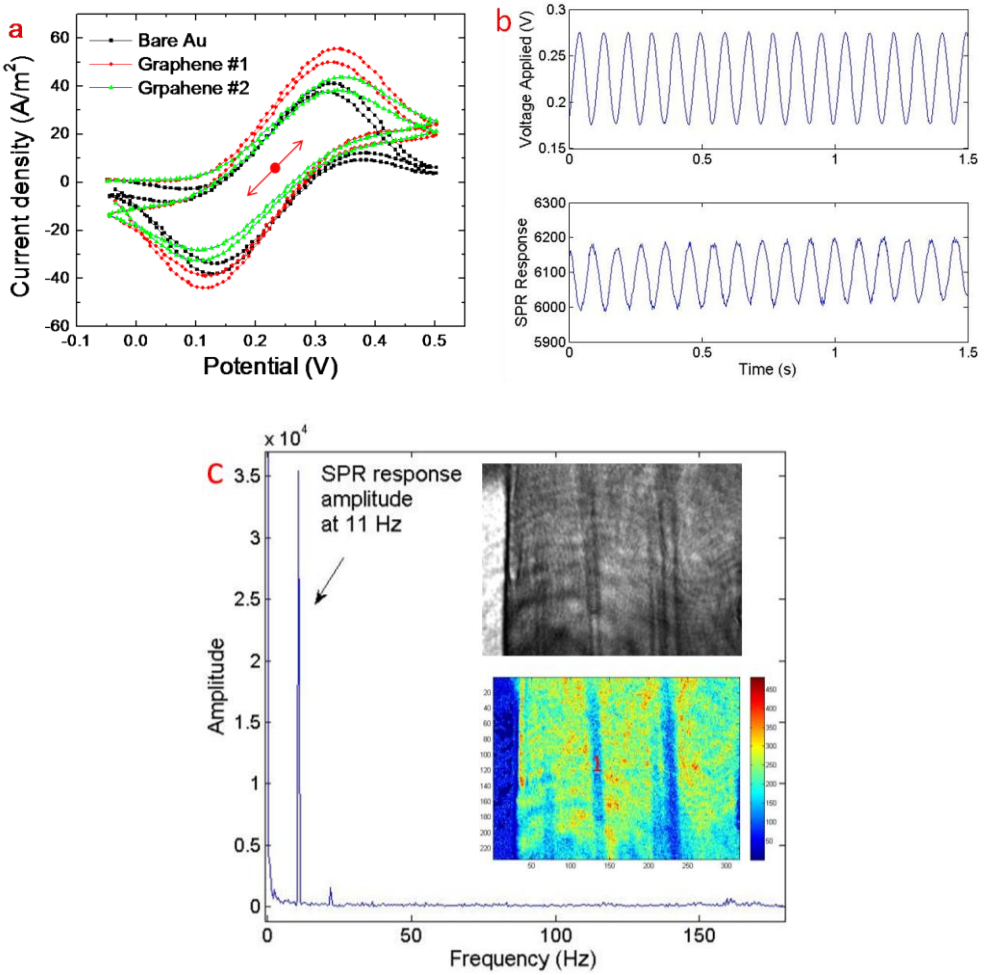

Figure 4.17. Principle of impedance measurement of graphene. (a) Principle of EC impedance with redox molecules. (b) Voltage applied and corresponding SPR response. (c) FFT of SPR response. Inset is SPR image and corresponding EC impedance with redox molecules.

As shown before, SPR will response to charging effect as well, moreover the charging effect has 180 degree shift with the SPR response due to ferricyanide redox molecules. Charging effect will increase with higher frequency, while the ferricyanide response decreases with increased frequency. However at low frequency region (<100Hz), the ferricyanide response still dominate the SPR response. Therefore the amplitude of SPR response reflects the reactivity of the local electrode surface. To obtaine an accurate amplitude information, a FFT of SPR response is executed (Figure 4.17 (c)). The peak frequency is right at 11Hz and peak amplitude reflects SPR response in that region. FFT is applied to each pixel and plot the amplitude of each pixel at the frequency applied. The amplitude image (inset of Figure 4.17 (c)) of electrode surface represents the EC reaction response at local electrode area.

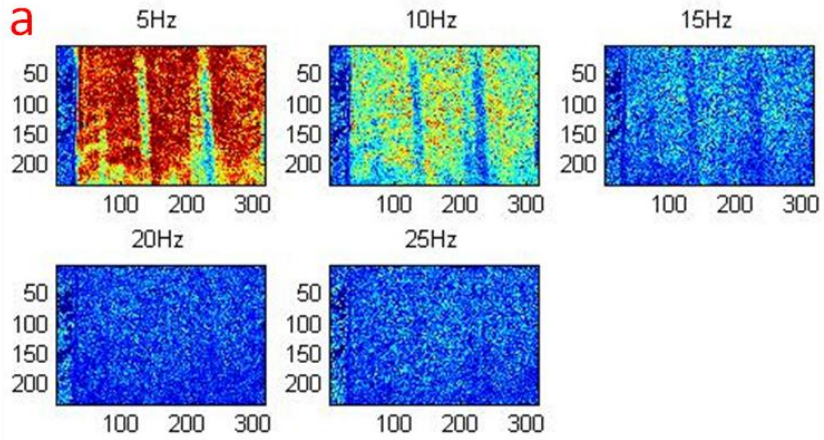

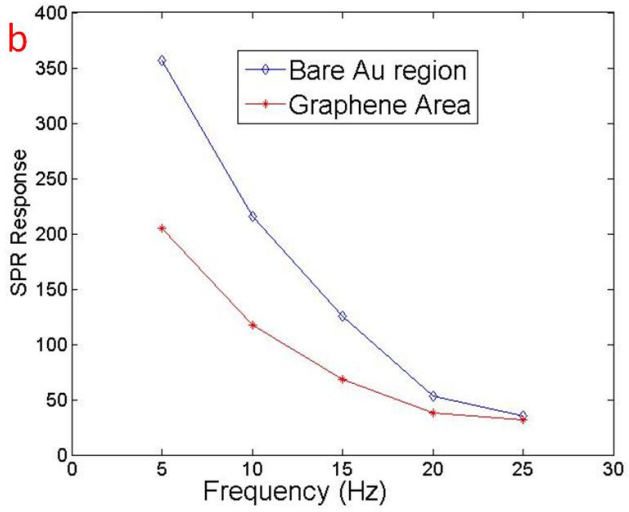

Figure 4.18. Graphene impedance image with redox molecules. (a) Impedance image with redox molecules at different frequency. Vpp = 0.1V. It is same area with Figure 4.13 and 4.14. (b) Amplitude of graphene and bare Au region at different frequency. Graphene area location is pointed out in inset of Figure 4.17 (c) by "1".

Figure 4.18 (a) shows the impedance amplitude image of graphene area at different frequency. As frequency increases, the time for redox molecule to react on the surface decreases therefore the SPR response amplitude also decreases. The relationship is roughly proportional to the reverse of frequency after subtract out the base line (~40 in Figure 4.18 (b)) which is background noise. At frequency range 5 To 25 Hz for both Figure 4.18 (a) and (b), the amplitude response of graphene is smaller than that of bare Au (about half). This is probably due to the contact resistant for graphene area is bigger than bare Au. And also the increasing EC response is not observed at the edge of graphene layer.

Figure 4.19 shows single layer graphene's impedance response at different frequency. Note that the Vpp is 0.3V which is much bigger than Figure 4.18. That is why the amplitude is much higher and decays slower (at higher frequency) than Figure 4.18. At low frequency (~1Hz), the single layer graphene has similar response with bare Au, which matches the results in 4.3.2 section's normal CV scan. As frequency increases, both graphene and bare Au's amplitudes decrease and graphene's response is about half of bare Au.

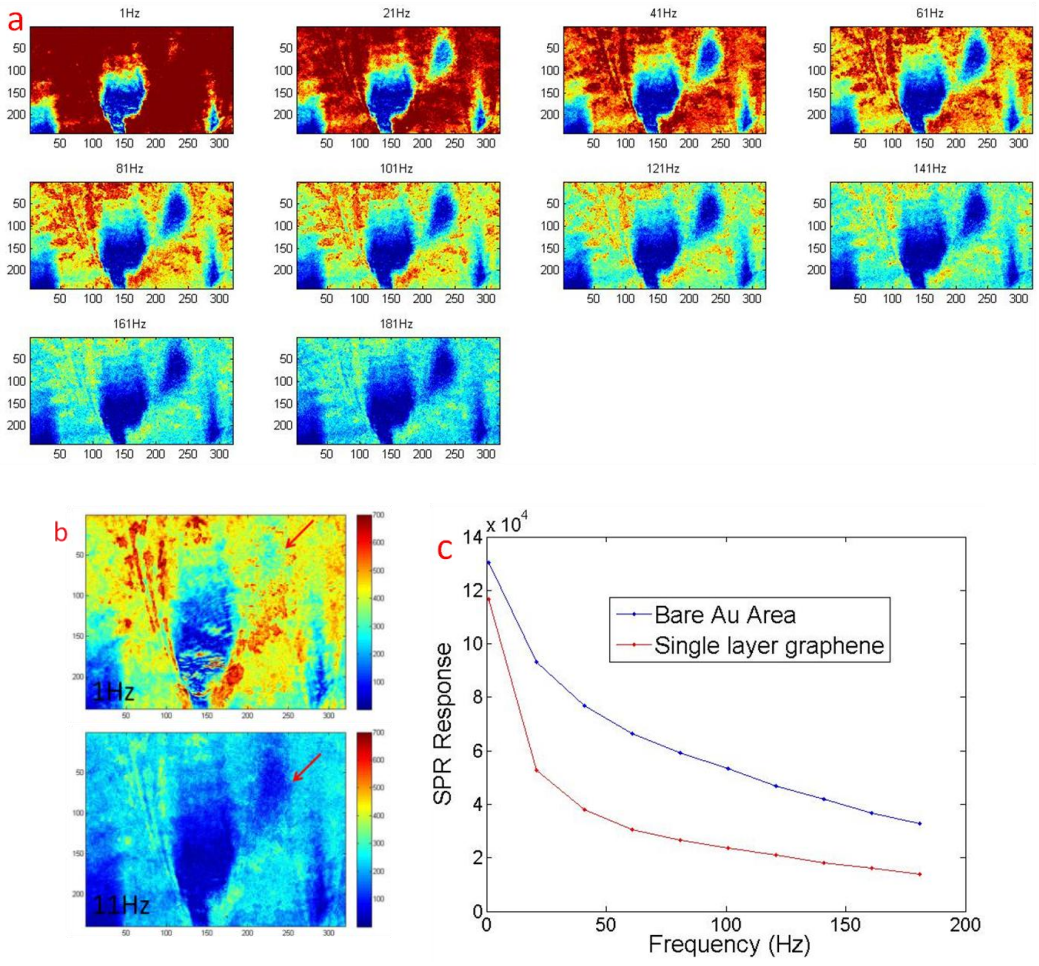

Figure 4.19. Impedance images of single layer graphene at different frequency. (a) Impedance amplitude image of single layer graphene piece (same flack with

Figure 4.7 and 4.8) at different frequency. Vpp = 0.3V. (b) Re-plot of amplitude response at 1Hz and 11Hz. (c) Bare Au and single layer graphene's amplitude response at different frequency.

CHAPTER 5

PLASMONIC-BASED IMAGING OF LOCAL SQUARE WAVE VOLTAMMETRY

5.1. Introduction

Electrochemical (EC) detection has matured into a powerful analytical tool for various applications, from trace chemical analysis, glucose and neurotransmitters monitoring, to protein and DNA microarray detections. Conventional EC methods measure the total current from an electrode, which does not have spatial resolution to measure local EC reactions. Spatial resolution is needed for studying heterogeneous reactions[78, 79], for monitoring single cell activities[80], and for high throughput reading of microarrays[81]. As discussed in previous chapters, to provide EC methods with spatial resolution, Scanning Electrochemical Microscopy (SECM) has been developed, which maps local EC current by scanning a microelectrode across a sample surface[82, 83]. Although SECM has found numerous applications, mechanical scanning of the microelectrode limits its imaging speed and the proximity of the scanning microelectrode to the reaction sites may perturb the reactions. Furthermore, the measured current scales with the electrode area, which leads to a decreasing signal when one attempts to improve the spatial resolution by decreasing the electrode size. Other imaging techniques, including Scanning Tunneling Microscopy, Atomic Force Microscopy and optical interference microscopy[84]

have been developed to provide high-resolution structural information of an electrode surface, but they do not measure electrochemical reaction current.

As introduced in Chapter 3 and 4, a plasmonic-based electrochemical current imaging (PECI) technique has been developed that can map local current of an electrode with sub-micron resollution[85]. Instead of probing local EC current point by point electrically with a microelectrode, PECI technique images the local EC current optically by measuring the refractive index change near the electrode surface due to local EC reaction. Because oxidation or reduction of an analyte is almost always accompanied by a change in the optical property of the analytes, the approach is quite universal. In addition to high spatial resolution, PECI is fast and non-invasive, and its signal does not decrease with the size of a region of interest[85]. In previous Chapters (3 and 4), PECI method has been proved to provide local cyclic voltammetry (CV) information. Although popular, CV suffers from background current that often places a practical limit on EC detection. Square Wave Voltammetry (SWV) has become a widely used EC detection technique because of its high sensitivity and superior capability to suppress unwanted background current. Important applications of SWV includes DNA damage detection[81, 86], trace chemical analysis[87, 88] and protein detections[89]. However, SWV requires fast response time of the detection system, which poses a technical challenge to imaging techniques. Furthermore, capacitive charging needs to be considered when developing PECI of SWV. In this chapter, a method has been established to perform local SWV with PECI.

5.2. Theory

EC current includes two major contributions: faradaic current which originates from oxidation or reduction of analyte molecules on the electrode, and non-faradaic current due to, e.g., capacitive charging current. Conventional EC methods measure both faradaic and non-faradaic currents. Likewise, PECI also measures both the faradaic and non-faradaic contributions. The former is measured, as pointed earlier, via EC reaction-induced change in the refractive index of the analytes. In contrast, the latter is measured because plasmonic signal is sensitive to surface charge density of the electrode, which has been used in our recent work[90, 91] to image electrochemical interfacial impedance.

The total plasmonic signal ($\Delta\theta$) can be expressed at a given location and time as a sum of faradaic ($\Delta\theta_f$) and non-faradaic ($\Delta\theta_c$) contributions,

$$\begin{aligned}\Delta\theta(x,y,t) &= \Delta\theta_f(x,y,t) + \Delta\theta_c(x,y,t) \\ &= \beta\int_0^t i_f(x,y,t')(t-t')^{-1/2}dt' + \frac{1}{\alpha}\int_0^t i_c(x,y,t)dt \qquad (1)\\ \beta &= B\left(\alpha_R D_R^{-\frac{1}{2}} - \alpha_O D_O^{-\frac{1}{2}}\right)(nF\pi^{1/2})^{-1},\\ \alpha &= -\frac{ed_m n_e \varepsilon_2(\varepsilon_2+\varepsilon_m)^2 \sin(2\theta_R)}{\varepsilon_1^2(\varepsilon_m-1)}.\end{aligned}$$

where i_f and i_c are the corresponding faradaic current and charging current, α and β are the constants[90, 92] that can be determined independently. The detailed discussion about α and β can be found in Chapter 2.

In order to measure the electrochemical activity of a target analyte, one needs to suppress unwanted background current in electrochemical analysis. This task is accomplished in conventional SWV by applying a square wave potential superimposed on a linearly sweeping potential to the electrode. The current

response to each square wave has two components, faradaic current and charging current. The latter component changes exponentially with time, and reaches a steady state faster than the former. So by measuring current at the end of each square wave, right before the next, the transient charging current is suppressed. In PECI, the same potential waveform is applied to the entire electrode and the plasmonic response is measured in each electrode region. From the local plasmonic signal vs. time, local current vs. time is determined, and then local SWV was obtained by measuring the current at the end of each square wave. To simplify signal/data processing, the second term may be excluded when calculating the EC current. Including the second term in Eq. 1 leads to only a small baseline shift in the SWV, which is the essence of SWV for minimizing background current. This will be discussed in the Section 5.5.

5.3. Experimental details

The plasomonic imaging setup is based on the widely used Krechmann configuration (Scheme 1),[93] which comprises a light emitting diode (LED) light source (670 nm), collimating lens, prism, imaging optics, polarizer, and a CCD camera. A microscope cover slide coated with 47 nm thick Au film was coupled optically to the prism surface via index of refraction matching fluid. The plasmonic image was captured at up to 380 frames per second, allowing for measurements of the plasmonic response induced by the applied potential waveform.

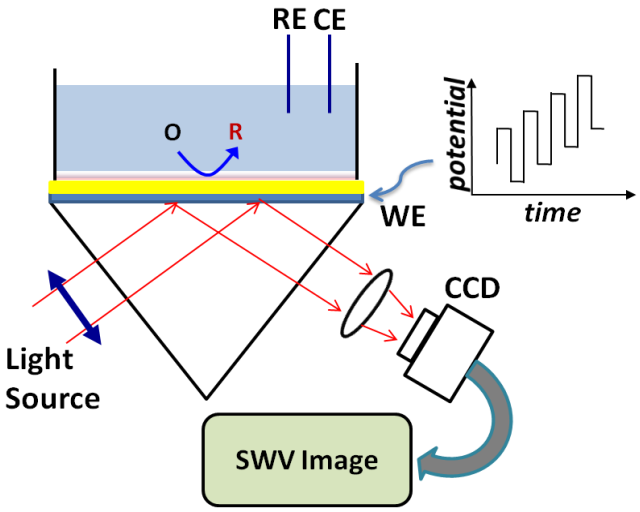

Figure 5.1. Experiment setup of SWV imaging.

Hexaammine-ruthenium (III) chloride ($[Ru(NH_3)_6]Cl_3$), potassium ferricyanide ($K_3[Fe(CN)_6]$), potassium hexacyanoferrate (II) trihydrate ($K_4[Fe(CN)_6]\ 3H_2O$) and sodium fluoride (NaF) were purchased from Sigma Aldrich and were used as received. All aqueous solutions were prepare from PURELAB ultra (>18.2 MΩ cm^{-1}) water.

SWV was performed at room temperature using a Teflon EC cell fixed on top of the Au film, which was also served as the working electrode. Potential waveform with frequency 10 Hz, pulse height 50 or 25 mV and a potential step 10 mV or 5 mV was applied to the Au electrode with an Autolab potentiostat using a Pt wire and Ag/AgCl/KCl as counter electrode and reference electrode, respectively. Redox reaction of 10 mM of $Ru(NH_3)_6^{3+}$ or 20 mM of $[Fe(CN)_6]^{3-}$ and $[Fe(CN)_6]^{4-}$ mixture (1:1 ratio) in 0.2 M NaF solution were studied. A Matlab program was used to determine PECI from the plasmonic signals. The setup was

capable of simultaneously recording the total electrochemical current with the conventional EC method, and acquiring PECI of the electrode.

To demonstrate local SWV imaging capability, a patterned hexadecanethiol monolayer was created by soft lithograph technique.[94] 2 mM-hexadecanethiol in ethanol solution was applied to PDMS stamp surface by cotton Q-Tips. After drying the stamp with N2 for 15 s, it was then brought into contact with the Au film for 5-10 s.

5.4. PECI of SWV

To validate PECI of SWV, SWV measurements were first carried out on an Au electrode in 10 mM $Ru(NH_3)_6^{3+}$ simultaneously with the plasmonic imaging and conventional electrochemical approaches. Figure 5.2(a) shows the potential waveform applied to the electrode, which is composed of square waves superimposed on a linearly sweeping potential from 0 to -0.3 V. The corresponding plasmonic response over an area of 1.8 x 1.3 mm^2 of the electrode is shown in Figure 5.2(b). The plasmonic response is initially small (0 to ~ 0.5 s), which is almost entirely due to capacitive charging effect because the potential is far more positive than the formal potential of the redox reaction (~ -0.16 V). The response increases and reaches a maximum as the potential sweeps to the formal potential (at ~ 2 s), and then decreases again and returns to the capacitive charging background.

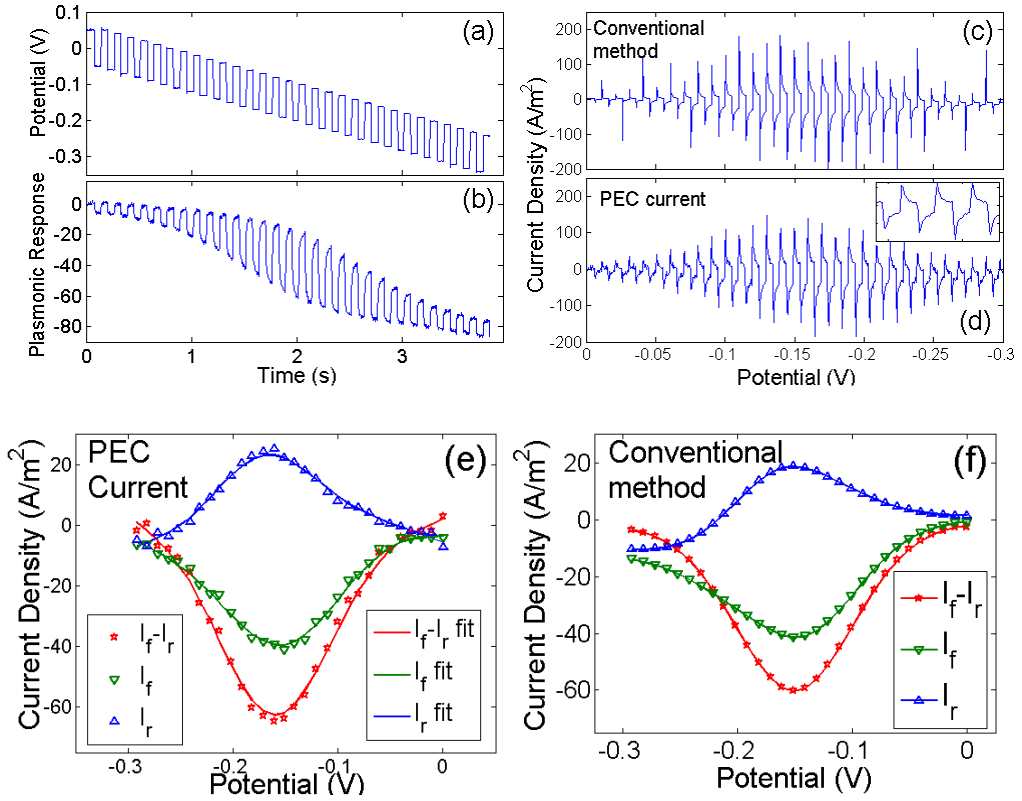

Figure 5.2. PECI response and current of SWV vs conventional method. Solution is using $Ru(NH_3)_6^{3+}$ in 0.2 M NaF. (a) Potential waveform for SWV. It consists of square waves superimposed on a linear potential, sweeping from 0 to -0.3 V. (b) Plasmonic response due to the potential waveform shown in (a). (c) Transient current density vs. potential obtained with the conventional electrochemical method. (d) Transient current density vs. potential of the same electrode obtained with the plasmonic-based method. (e) SWV obtained with the plasmonic method. (f) SWV obtained with the conventional electrochemical method. I_f and I_r in (e) and (f) are forward current and reverse current, extracted at the end of each of the forward potential step, and reverse potential step, respectively.

From the plasmonic response vs. time, the current can be determined using the algorithm described in Chapter 2, and the result as a function of potential is

shown in Figure 5.2(d). For each square wave there is a forward (in the direction of potential sweep) and reverse potential steps. In the present case, the potential sweeps negatively, so the forward potential step is in the negative potential direction. Figure 5.2(d) shows that each forward potential step induces a sudden drop in the current, followed by a fast rise and then a slow rise in the current. The fast rise is due to capacitive charging process, and the slow rise is due to electrochemical reaction (faradaic current). Associated with each reverse potential step, the current response is reversed, as expected. The simultaneously recorded current by the conventional method is shown in Figure 5.2(c), which is in quantitative agreement with the plasmonic-based current. This observation demonstrates that the algorithm to convert plasmonic signals into electrochemical current works well not only for a linearly sweeping potential but also for a potential waveform containing sharp potential steps.

Like the conventional SWV, the current shown in Figure 5.2(d) was extracted at the end of each forward potential step, and it was denoted as forward current, I_f (green triangles, Figure 5.2(e)). The forward current vs. potential shows a trough near -0.15 V. Similarly, the reverse current was obtained , I_r, from the end of each reserve potential step, vs. potential (blue stars in Figure 5.2(e)), which shows a peak near -0.15 V. The difference between the forward and reverse currents, I_f-I_r, vs. potential is the SWV, shown as red stars in Figure 5.2(e). For comparison, the corresponding I_f, I_r, and I_f-I_r obtained with the conventional SWV in Figure 5.2(f) was plotted. It is clear that the plasmonics-based SWV and the conventional SWV are excellent agreement with each other.

$[Fe(CN)_6]^{3/4-}$ in 0.2M NaF was also studied using the same approach, and observed quantitative agreement between the SWVs obtained by the plasmonic and conventional approaches. SWV measurement was carried out also in 10 mM $[Fe(CN)_6]^{3/4-}$ + 0.2M NaF solution by applying a potential waveform composed of square waves with a step height of 5 mV and frequency of 10 Hz superimposed on a linearly sweeping potential from +0.1 V to +0.4 V. The plasmonic response and the plasmonic-based current density vs. potential are plotted in Figure 5.3(a), and SWVs obtained from the current at the end of each potential step are shown in Figures 5.3(b) (PECI method) and c (conventional method). Quantitative agreement of the plasmonic-based SWV with the conventional SWV for $[Fe(CN)_6]^{3/4-}$ further validates the plasmonic imaging of SWV.

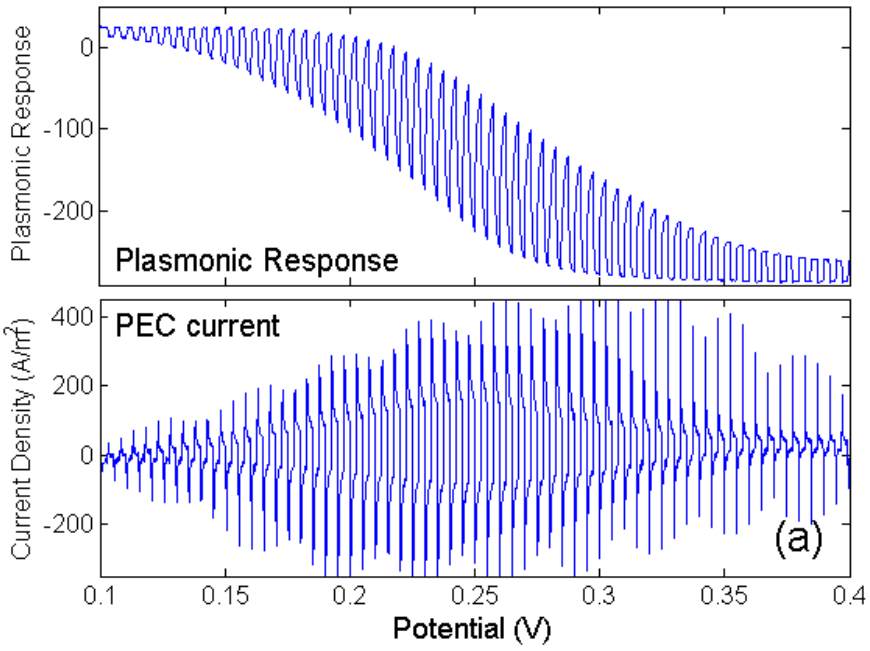

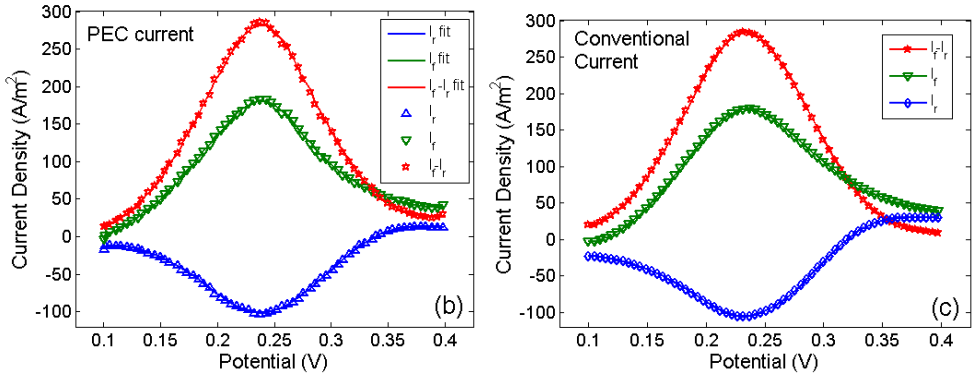

Figure 5.3. PECI response and current of $[Fe(CN)_6]^{3/4-}$ in 0.2M NaF. (a) Top: Plasmonic response vs. potential in10mM $[Fe(CN)_6]^{3/4-}$. Bottom: Transient plasmonic-based electrochemical current (PEC) vs. potential. (b) and (c) Plasmonic-based and conventional SWV, where I_f, I_r and I_f-I_r are forward, reverse and difference current.

5.5. Charging effects of SWV

To examine how capacitive charging affects the PECI, two plasmonic SWV measurements has been performed. The first measurement was carried out in the pure supporting electrolyte, 0.2 M NaF solution, and the result shown as the green curve in Figure 5.4(a) is due to background current (e.g., capacitive charging current). The second measurement was in 10 mM $Ru(NH_3)_6^{3+}$ + 0.2 M NaF solution, and the plasmonic response contains contributions from both the redox reaction of $Ru(NH_3)_6^{3+}$ and background current (red curve, Figure 5.4(a)). By subtracting the background current in the first measurement from the SWV in the second measurement, a charging effect-corrected plasmonic response of SWV was obtained, which is shown as the blue curve in Figure 5.4(a) (shift up 30 intensity units). Note that after subtraction, the plasmonic response to the square

waves near the beginning (0 to -0.05 V) and end (-0.275 to -0.30 V) of the potential sweep drops to nearly zero, indicating effective correction of the capacitive charging contribution.

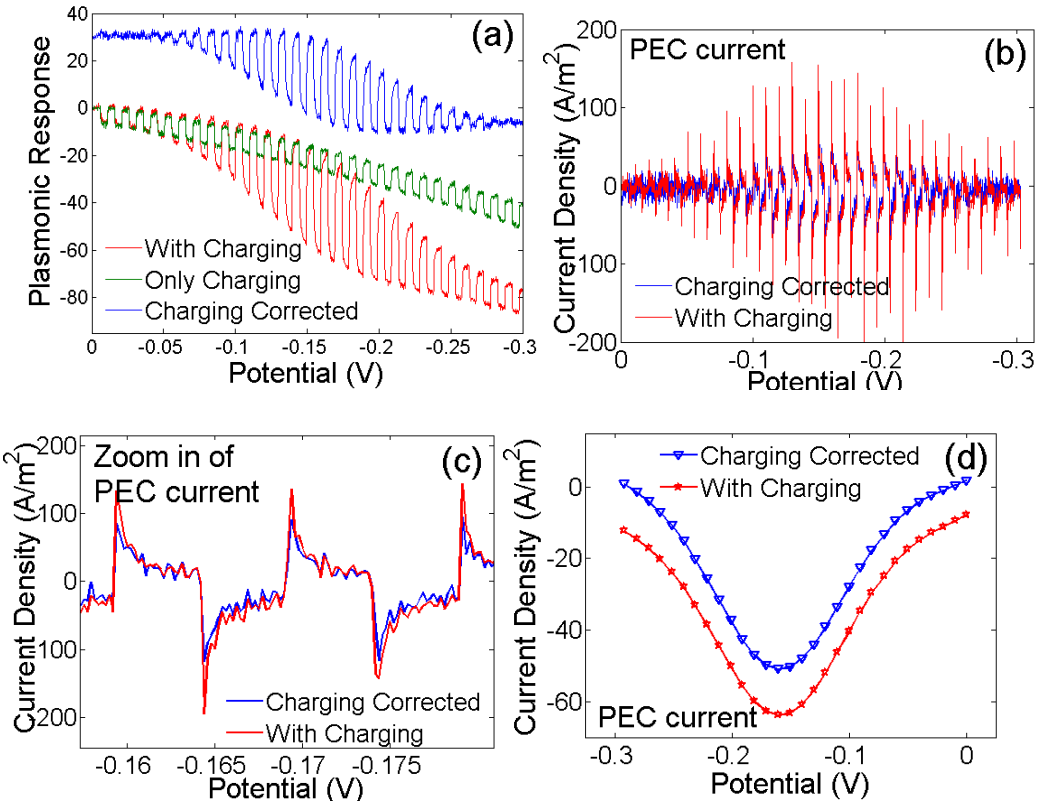

Figure 5.4. Charging effect of PECI SWV current. (a) Plasmonic responses in 10 mM $Ru(NH_3)_6^{3+}$ + 0.2 M NaF (red) and in 0.2 M NaF (green). The former contains both the redox reaction current and background current, while the latter contains only the background current. The difference of the two (blue) taken by subtracting the red curve from the blue curve presents background corrected SWV. Note that for clarity the background corrected SWV is shifted up by 30 units. (b) Corresponding plasmonic current densities vs. potential. (c) Zooming-in of current density signals of two potential steps. (d) SWVs with (red) and without correction of the background charging effect (blue).

From the plasmonic responses (Figure 5.4(a)), the current with (blue curve in Figure 5.4(b)) and without (red curve in Figure 5.4(b)) correcting the background current were determined. Zooming-in of two square waves shows that although the capacitive charging associated with each potential step leads to a large transient current in the beginning (Figure 5.4(c)), its contribution decreases rapidly over time, and becomes negligible near the end of a potential step. Figure 5.4(d) compares SWVs (I_f -I_r vs. potential) with and without background current correction. The two SWVs are similar except for a small baseline shift. The baseline shift is due to the capacitive charging effect associated with the linearly sweeping potential, which is also present in the conventional SWV.

5.6. Local PECIs at different SWV potential

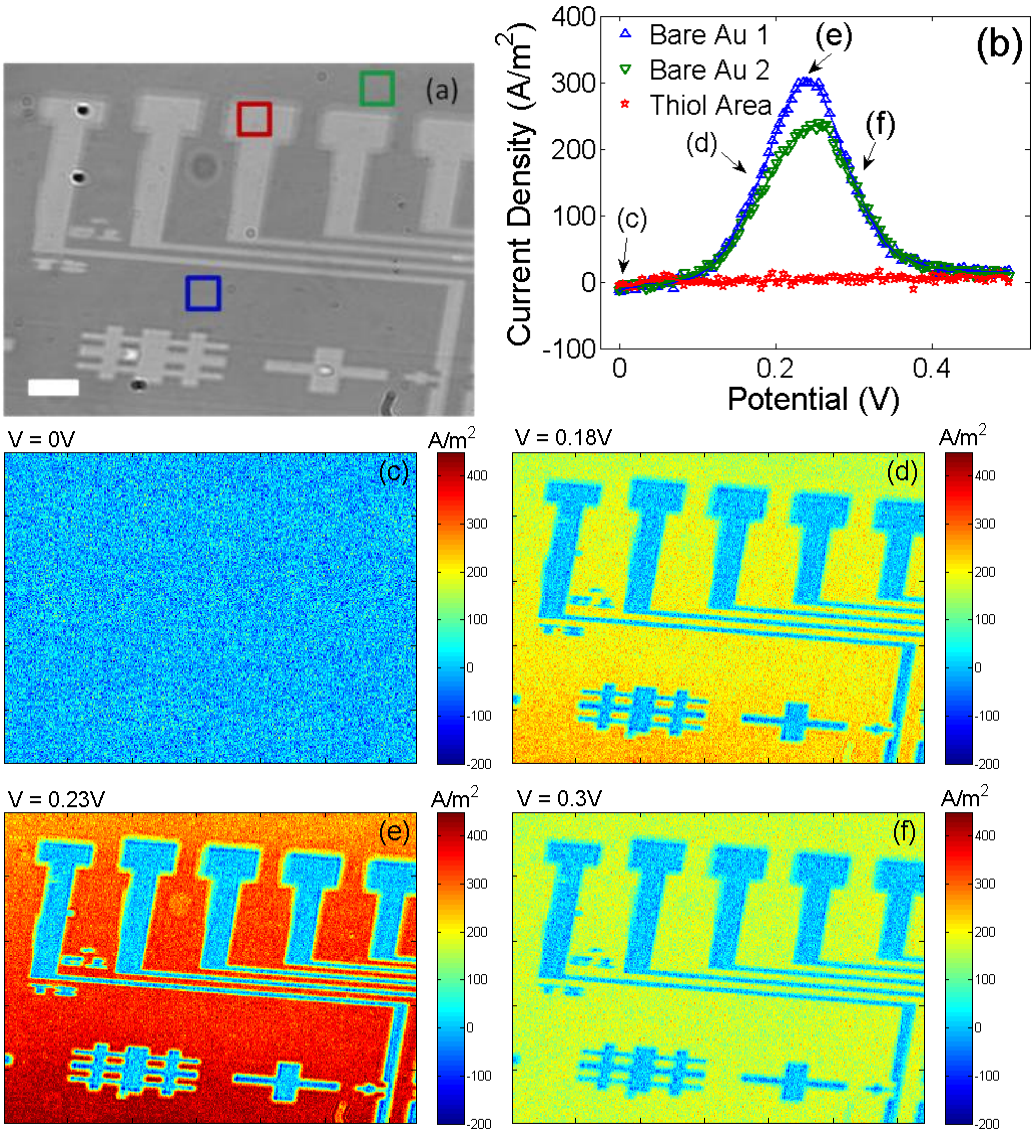

Figure 5.5. PECI current density images at different potential of a patterned Au surface. (a) SPR image of a Au surface patterned with thiols (the surface potential was not controlled), the scale bar is 100μm. (b) Local SWVs of the regions marked in (a). (c-f) Snapshots of SWV video of the surface at different potentials (which are pointed out in (b)).

In order to demonstrate SWV imaging capability with PECI, heterogeneous electrochemical reactions was studied with a Au surface patterned by hexadecanethiol monolayer. Figure 5.5(a) is a conventional SPR image, in which the bright patterns correspond to the hexadecanethiol-covered region, and the dark background is the bare Au surface. SWV imaging of the surface in 20 mM $[Fe(CN)_6]^{3/4-}$ + 0.2 M NaF electrolyte is performed. Figure 5.5(b) shows SWVs of three selected regions on the electrode, two from the bare Au area (marked by blue and green squares in Figure 5.5(a)) and one from the thiol-covered area (red square in Figure 5.5(a)). Each SWV was obtained from the plasmonic signal averaged over the corresponding region. The thiol-covered region shows only a flat baseline, due to effective blockage of the redox reaction by the thiol monolayer. In contrast, the bare Au regions show pronounced peaks near 0.25 V in the SWVs due to the redox reaction of $[Fe(CN)_6]^{3/4-}$. Although both bare Au regions display the redox peak, the peak amplitudes are different, which reflects different amounts of thiol "contamination" during the contact printing in the two regions.

It is also possible to obtain SWV at each pixel of the plasmonic image, which provides a SWV image, from which a SWV from each pixel is obtained. Figures 5.5(c)-(f) show a few snapshots of such SWV images at several different potentials, and a video showing SWV image during potential sweep is provide in the Supporting Materials. At 0 V, the image (Figure 5.5(c)) shows only noise, which is expected because no measurable redox reaction takes at the potential. Increasing the potential to +0.18V (closer to the formal potential), the current in

the thiol-covered regions remain small but the current in the bare Au region increases substantially, leading to high contrast images of the patterned surface (Figure 5.5(d)). When the potential increases to +0.23 V, the thiol-covered region still shows no current while the current in the bare Au regions reaches maximum (Figure 5.5(e)). Further increasing the potential, the current in the bare Au regions decreases again (Figure 5.5(f)). This spatial information and SWV imaging capability are not available in the conventional SWV.

5.7. Conclusion

In this chapter, PECI method has been extended to image local SWV. The SWV averaged over an electrode is in quantitative agreement with the simultaneously recorded SWV obtained by the conventional electrochemical method, which validates the plasmonic-based SWV. SWV imaging capability has been demonstrated and applied to study local electrochemical reactions on a surface. This capability is not possible with the conventional electrochemical methods, and it is particularly suitable for electroanalysis of heterogeneous reactions and for electrochemical detection of microarrays which will be discussed in the next chapter (Chapter 6).

CHAPTER 6

CATALYTIC CURRENT IMAGE OF PLATINUM NANOPARTICLE BY PECI TECHNIQUE

6.1 Introduction

Nanoparticles have attracted intense interest and found numerical applications in all the field over the past two decades such as electrocatalysis[95], sensors[96, 97], energy and fuel cell[98], SERS[99, 100] and optoelectronics[101]. Among these applications, the electrocatalysis reaction of nanoparticle is one of the most important areas[95, 102].

In general, the surface area decides the mass and heat transfer between particles and their surrounding when the reaction happens. Thus, the main reason that nanoparticles have improved catalysis effect is due to its large surface-to-volume (A/V) ratios compared with larger materials of same mass on the surface. Figure 6.1 shows the ratio of number of atoms (N_S) appear on the surface of nanoparticle and number of atoms (N_T) in the particle at different particle sizes (D). Obviously, the smaller particle size will have bigger surface-to-volume ratio (A/V). The typical surface area of a catalysis nanoparticle is 100-400 $m^2 g^{-1}$ which is more than million times bigger than bulk material.

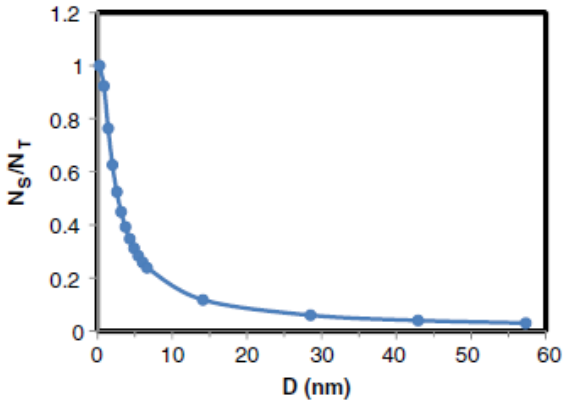

Figure 6.1. The calculated surface volume ratio of gold nanoparticle. X-axis is particle size (D). N_S and N_T represent the number of atom expose to surface or in the nanoparticle. From ref. [102]

Except nanoparticle's surface area and its composition are important for catalysis reaction, the shape of the particle also matters. Fundamental studies have shown that high-index planes ({210}, {410}, {730},{520}…)have much higher catalytic activity than most common stable planes ({100},{110} and {111})[95]. This is because the surfaces of these nanoparticles have a large density of atomic steps and dangling bonds. Therefore, in general small nanoparticles, no matter what kind of shape it is, will have more edges, steps and dangling bonds which will have more catalysis ability.

Since many properties (composition, size and shape of the particle) can affect the catalysis reaction of nanoparticles, the screening process is extremely important to find right nanoparticle for particular reaction. Scanning electrochemical microscope (SECM) has been applied to nanoparticle electrocatalytic properties screening[79, 103]. However, the efficiency of SECM

is slow due to the scanning process of the method. And also the electrode which is scanning through the surface will perturb the reaction.

Plasmonic electrochemical imaging (PECI) technique has been demonstrated in Chapter 3 and shows advantages on mapping local current of an electrode with sub-micron resolution. Instead of probing local EC current point by point electrically with a microelectrode, PECI technique images the local EC current optically by measuring the refractive index change near the electrode surface due to local EC reaction. In Chapter 3 and 4, PECI has been demonstrated as a technique with high spatial resolution, fast current imaging ability (upto 100,000 current images per second with enough light). In addition, PECI is non-invasive and its signal does not decrease with the size of a region of interest[85].

In this chapter, to demonstrate the ability of PECI for heterogeneous reaction current image, hydrogen catalysis reaction by platinum nanoparticle was investigated by PECI. Platinum nanoparticle (PtNP) microarray was modified onto Au surface. EC potential was applied to surface, due to the H2 generated from PtNP area, the refractive index of those areas were changed therefore the current image was obtained by PECI. First of all, the coefficient of the PECI was calibrated for H2 evolution reaction. The process to obtain PECI current image of PtNP microarray was demonstrated next, then the current image of different concentration of PtNP array was measured at different potential by PECI. At last, EC impedance method was applied to detect the PtNP local concentration.

6.2. Experiment

PtNP synthesis: Citrate-stabilized platinum nanoparticles were synthesized. A total of 1 mL of 1% H2PtCl6 aqueous solution was added into 100 mL of DI water and heated to boiling. Then 3 mL of 1% sodium citrate aqueous solution was added quickly into the boiling solution. The mixture was kept boiling for 30 min, until the color of solution turn dark.[104] Atomic force microscope (AFM) was use to confirm the size of synthesized PtNP. The size of PtNP is from 10 to 20nm (shown in Figure 6.2).

PtNP microarray modification: A 1.6nm thick Cr and 47nm thick Au was thermally evaporated onto a microscope cover slides in high vacuum ($3*10^{-6}$ Torr). After evaporation, the Au chip was clean and annealed by H_2 flame for 10 seconds. Au chips are immediately soaped into 1mM 1,3-Propanedithiol in ethanol for overnight (more than 8 hours). Au surface will be covered with 1,3-Propanedithiol molecule which is used to fix or link the PtNP onto Au surface. It is because the 1,3-Propanedithiol has two thiol molecules and one of them bind to Au substrate and the other one bind to PtNP. Then different concentration of PtNP solution was injected onto 1,3-Propaneditiol modified Au surface to form microarray. The array size ranges from 50 μm to 200 μm on diameter by adjust amount to inject onto the surface. The droplets will dry rapidly and Au substrate was rinsed with DI water for 10 seconds to rinse out the salt residue from PtNP solutions and nonbinding PtNP. N_2 gas was use to dry the substrate.

EC reaction: A Teflon EC reaction cell was mounted on top of Au substrate with PtNP microarray. 0.5 M H_2SO_4 solution was used for PtNP

catalysis reaction. The Au substrate was used as working electrode and the Ag/AgCl and Pt wires were used as reference electrode and counter electrode respectively. An Autolab potentiostat was used to apply potential to the system for cyclic voltammetry (CV) scan. A Pine potentiostat with controlling from function generator was used to apply impedance potential to the system.

Optical setup and program: Prism-based and microscope-based SPR setup was used in this experiment. For prism setup, a light from a 670nm LED was shined through a polarizer to generate a p-polarized light and hit onto the Au surface which is on top of prism. The SPR image was captured by a Pike camera with a zoom in lens mounted on it. The incident angle was adjusted for a best sensitivity range. A microscope setup was same as what have been described in Chapter 3. A MATLAB program was written to process the images and transform to PECI image.

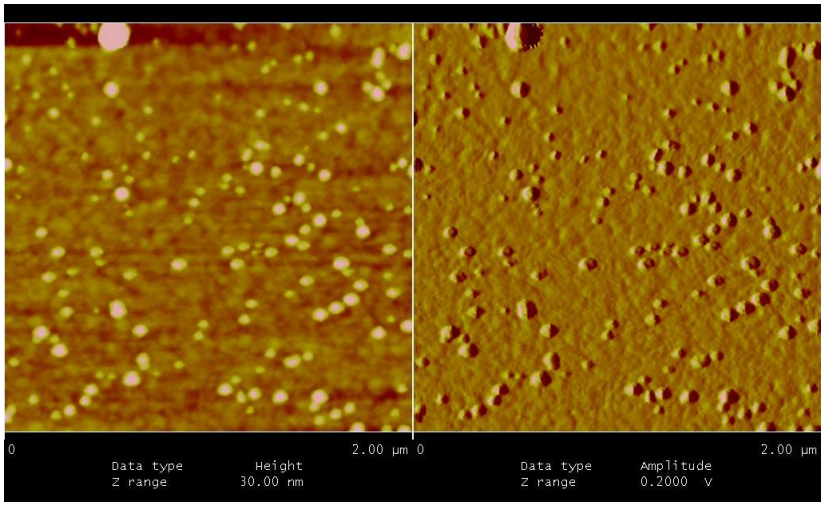

(a)

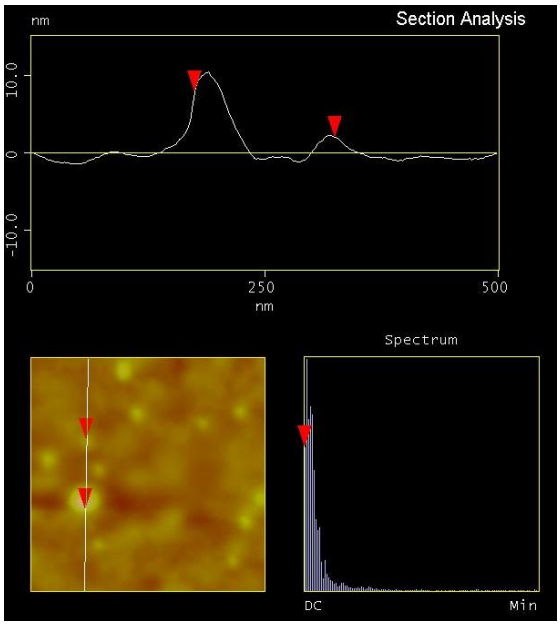

(b)

Figure 6.2. AFM image of PtNP on Au substrate. (a) AFM image of Au substrate modified by PtNP. The background variation is due to the grain of Au substrate. (b) Particle height section analysis.

6.3. Coefficient calibration

As discussed in Chapter 2, the PECI signal of EC reaction at given location and given time contributes from two parts: first part is from faradaic current, the second part is from charging current. The equation can be written by:

$$\Delta\theta(x,y,t) = \Delta\theta_f(x,y,t) + \Delta\theta_c(x,y,t)$$

$$= B\left(\alpha_R D_R^{-\frac{1}{2}} - \alpha_O D_O^{-\frac{1}{2}}\right)(nF\pi^{1/2})^{-1}\int_0^t i_f(x,y,t')(t-t')^{-1/2}dt' +$$

$$\frac{1}{\alpha}\int_0^t i_c(x,y,t)dt$$

$$= \beta\int_0^t i_f(x,y,t')(t-t')^{-1/2}dt' + \frac{1}{\alpha}\int_0^t i_c(x,y,t)dt \qquad (1)$$

where $\Delta\theta_f$ and $\Delta\theta_c$ are the PECI signal contributed from faradaic current and charging process. i_f and i_c are the faradaic and the charging current. α_R and α_O are the changes in the local refractive index per unit concentration for the oxidized and reduced molecules, respectively and D_R and D_O are the diffusion coefficients of the reaction species, n is number of electrons transferred per reaction, F is Faraday constant, B measures the sensitivity of the SPR angle to a change in the bulk index of refraction. β and α are two constants where

$$\beta = B\left(\alpha_R D_R^{-\frac{1}{2}} - \alpha_O D_O^{-\frac{1}{2}}\right)(nF\pi^{1/2})^{-1}, \quad (2)$$

$$\alpha = -\frac{ed_m n_e \varepsilon_2(\varepsilon_2+\varepsilon_m)^2 \sin(2\theta_R)}{\varepsilon_1^2(\varepsilon_m-1)}. \quad (3)$$

Based on equation (1) to (3), the faradaic current can be calculated from PECI signal $\Delta\theta_f$ and the only unknown parameter is β. Although the β includes B, α_R, α_O, D_R, D_O and n, for certain reaction last five parameters are fixed and B is always same for all the reactions. Therefore for the given EC reaction, H2 evolution reaction for here, the β can be consider as one unknown parameter which can be calibrated by control experiment.

There are 3 situations as shown in Figure 6.3 (a), the blue arrows represent the local current density. The first situation is bare Au surface and current I_1 includes charging current and a little H_2 evolution current for bare Au surface since bare Au also has H_2 evolution at more negative potential. Situation 2 and 3 both have thiol monolayer covered. For situation 3, there are PtNP fixed on top of thiol monolayer. I_2 includes charging and small H_2 evolution current, since the situation 2 covered with thiol layer, I_2 should be smaller than I_1. For situation 3,

because the extra PtNP area, the current at PtNP area is much bigger compare with situation 2 by the PtNP catalysis effect. Both I_2 and I_3 include charging effect, therefore the difference I_3-I_2 is purely due to the PtNP catalytic effect

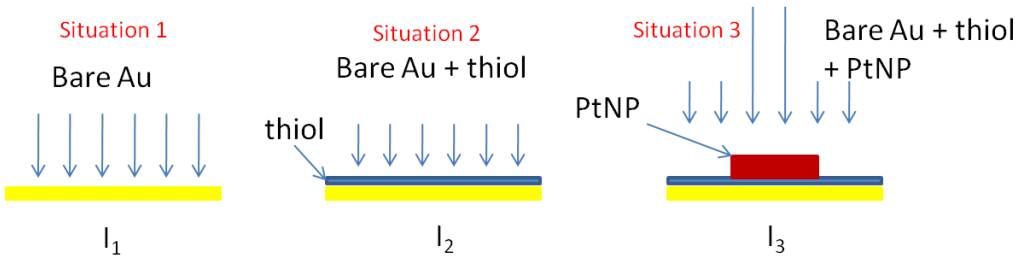

(a)

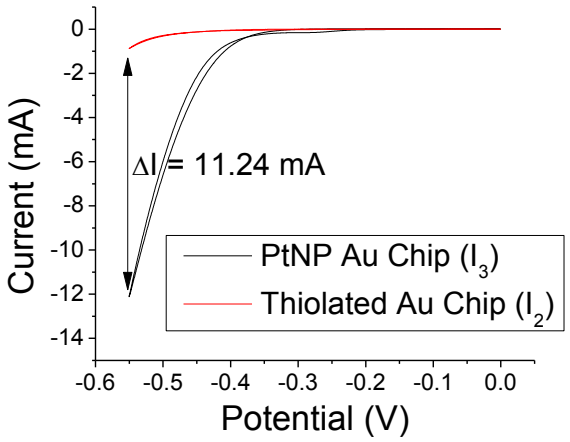

(b)

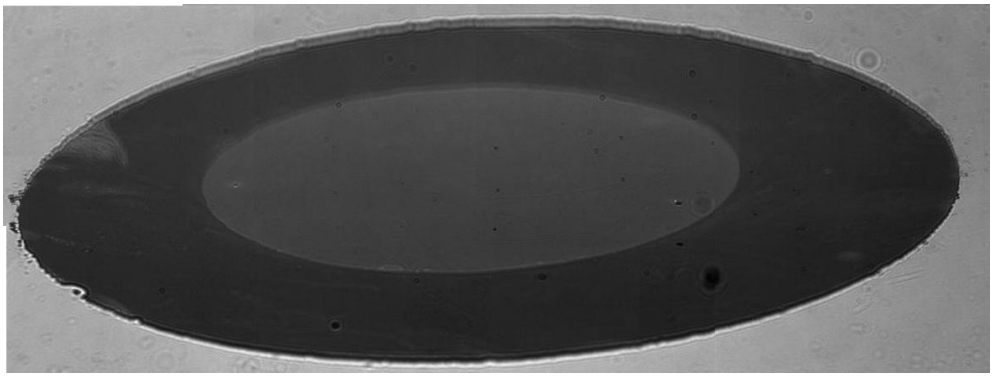

(c)

Figure 6.3. Calibration process. (a) 3 situations in H_2 evolution experiments. (b)CV curves for situation 2 and situation 3. (c) SPR images of PtNP modified Au surface. The center brighter ellipse is PtNP modified area while the rest darker area is Au with thiol monolayer area.

For calibration experiments both thiol covered Au chips (situation 2) and thiol covered Au with PtNP (situation 3) chips are used. The currents of these two situations (I_2 and I_3) were measured and the difference between these two currents are the i_f in Eq.(1) which is purely due to the PtNP catalysis effect. The PECI signal ($\Delta\theta_f$) was captured at same time. By using the equation (1) the constant β for H_2 evolution experiments can be calculated. Note that due to the subtraction of current I_3-I_2, the charging current part in Eq.(1) will be canceled out.

Figure 6.3(b) shows the CV curve for thiol covered Au chips (situation 2) and PtNP covered Au chip (situation 3). The difference between I_2 and I_3 is 11.24 mA. Figure 6.3(c) shows the SPR image of situation 3. The brighter ellipse in the center is PtNP modified/linked area (due to the compression on one direction, the circle pattern will look like an ellipse on SPR image). The outer darker ellipse is the thiol covered Au area without PtNP. From this image the area of PtNP modified region can be calculated (6.12 mm^2), and the current density can be calculated by: $i_f = \frac{\Delta I}{A} = \frac{I_3 - I_2}{A}$. Then from Eq.(4) the β can be calculated. For this chip, the current density i_f is 1835A/m^2 and the β is 0.0336 (mdeg $s^{1/2}$)/C.

$$\Delta\theta_f(x,y,t) = \beta \int_0^t i_f(x,y,t')(t-t')^{-1/2}dt' \qquad (4)$$

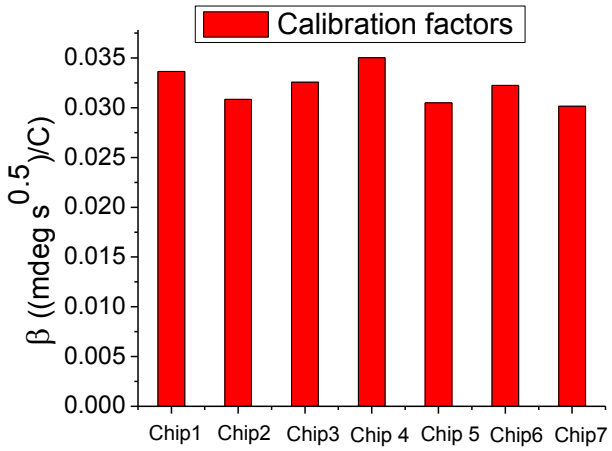

Figure 6.4. Calibration factor β for different chips.

Since this constant β will not change for a given reaction, therefore to get more accurate number, different chips have been tested. The results of β for different chips are shown in Figure 6.4 and it shows calibration factor β for different chips are excellent consistent. The mean is 0.0321 (mdeg $s^{1/2}$)/C and ratio between standard deviation and mean is 5.56%. Therefore the calibration factor β=0.0321 was used for entire chapter's PECI current calculation.

6.4. Principle demonstration

As discussed in experimental section, the PtNP was injected onto dithiol modified Au surface and PtNP linked onto Au surface and microarray was formed on Au chip. Figure 6.5(a) shows the SPR image of PtNP microarray on Au surface. The ellipse shape brighter patterns represent the PtNP microarray which has higher reflectivity due to the coverage of PtNP.

The potential was applied to patterned Au surface by a 3 electrodes system as described in experiment section. The potential range is from 0V to -0.8V to -

1V. Figure 6.5(b) shows the typical PECI response in which the black curve is the response of PtNP region and red curve is Au region and blue curve is the response difference between PtNP and Au region. When potential scan from 0 to -0.65V (Figure 6.5(b) and (c)), the Au and PtNP region have same response which is purely due to charging effect. This proves the PtNP modification does not change the charging properties of Au surface. More detailed evidence will be shown in section 8.

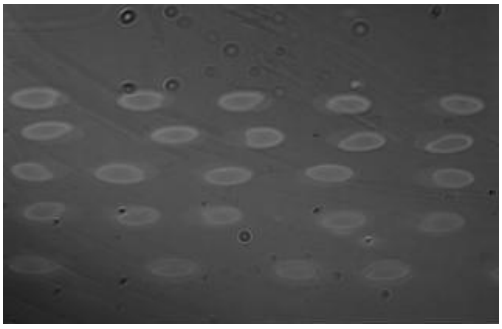

(a)

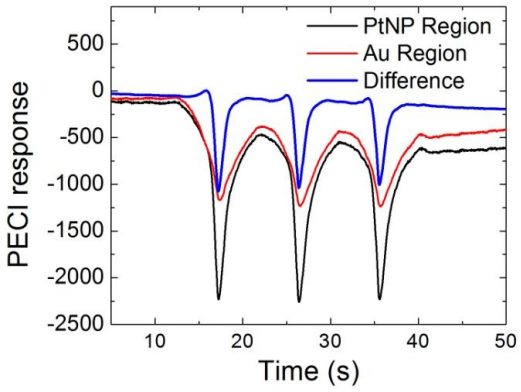

(b)

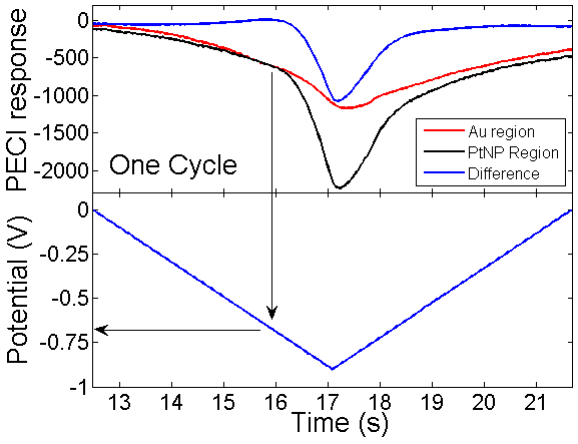

(c)

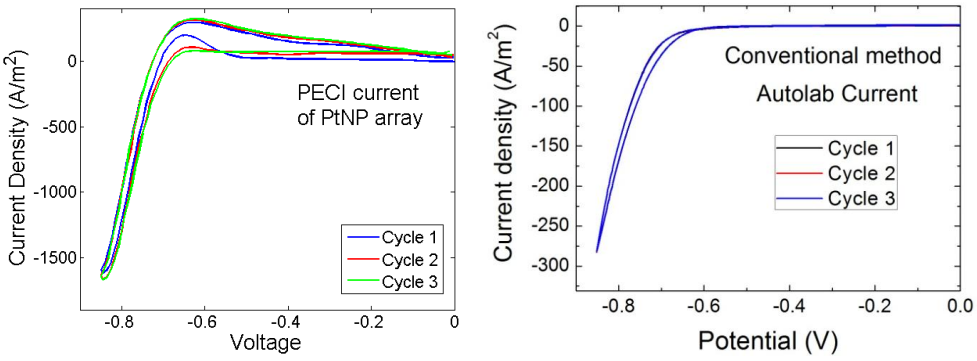

(d) (e)

Figure 6.5. Principle demonstration: PtNP catalytic reaction measured by PECI method. (a) SPR image of PtNP array surface. (b) PECI response of different region for 3 CV scan cycles. (c) PECI response of one CV cycle with corresponding potential. (d) PECI current of one PtNP spot. (e) Current density measured by conventional method.

The Au area only shows the typical charging effect response throughout entire scan, while the PtNP response has much sharper peak at more negative potential (<-0.65V). This is because at negative potential (<-0.65V) PtNP will catalyze the H_2 evolution reaction on the surface, thus H_2 molecules are generated on the PtNP region which will change the refractive index near sensing surface and decrease the PECI signal more while the signal on Au region still governs by charging effect. Therefore the PECI signal has much sharper peak when potential is more negative than -0.65V and the difference between PtNP and Au region is purely due to catalytic reaction (blue curve in Figure 6.5 (b) and (c)). The curve "difference" (blue curve) shows a peak only when potential is more negative than -0.65V which proves the huge catalytic reaction happens and when potential is

positive than -0.65V the PECI signal (blue curve) is very flat indicates no reaction happens. Note that the H_2 molecules generated from surface are still dissolved in solution, and it will not nucleate until certain concentration is reached. In our case, as long as potential is higher than certain value, the generated H_2 molecule can diffuse away from surface before concentration increase to the limit to trigger the nucleation.

From PECI response (the "Difference" in Figure 6.5 (b)), catalytic PECI current can be easily calculated by equation 4 where the β has been calibrated and charging effect has been subtracted out. Figure 6.5(d) shows a typical PECI current response of one PtNP spot. Conventional EC current was also recorded at same time which is shown in Figure 6.5(e), the current has been transformed to current density by dividing working electrode area. Since the conventional method only measures the total current of the entire surface, thus the current density from conventional method indicates average result of whole surface and it is much smaller than current density of PtNP area because most of area does not contribute the catalytic current.

Compare PECI current of PtNP with conventional method, the shape of the curves and the starting potential of catalytic reaction (~-0.68V) matches perfectly. A little peak was shown from -0.5V to -0.7V when potential scan back in PECI current curve, which is due to the reoxydation of H_2. This peak cannot be seen in conventional method which is because the current peak is averaged out by the whole surface. At mean time, PECI method is highly sensitive to the RI change near surface caused by reaction product concentration while conventional

method is only sensitive to electron exchange on working electrode surface. Some reaction may not have many electrons exchange while the RI change could be big and detectable. This proves local catalytic current of PtNP spot can be obtained by PECI method.

6.5. PECI of PtNP microarray

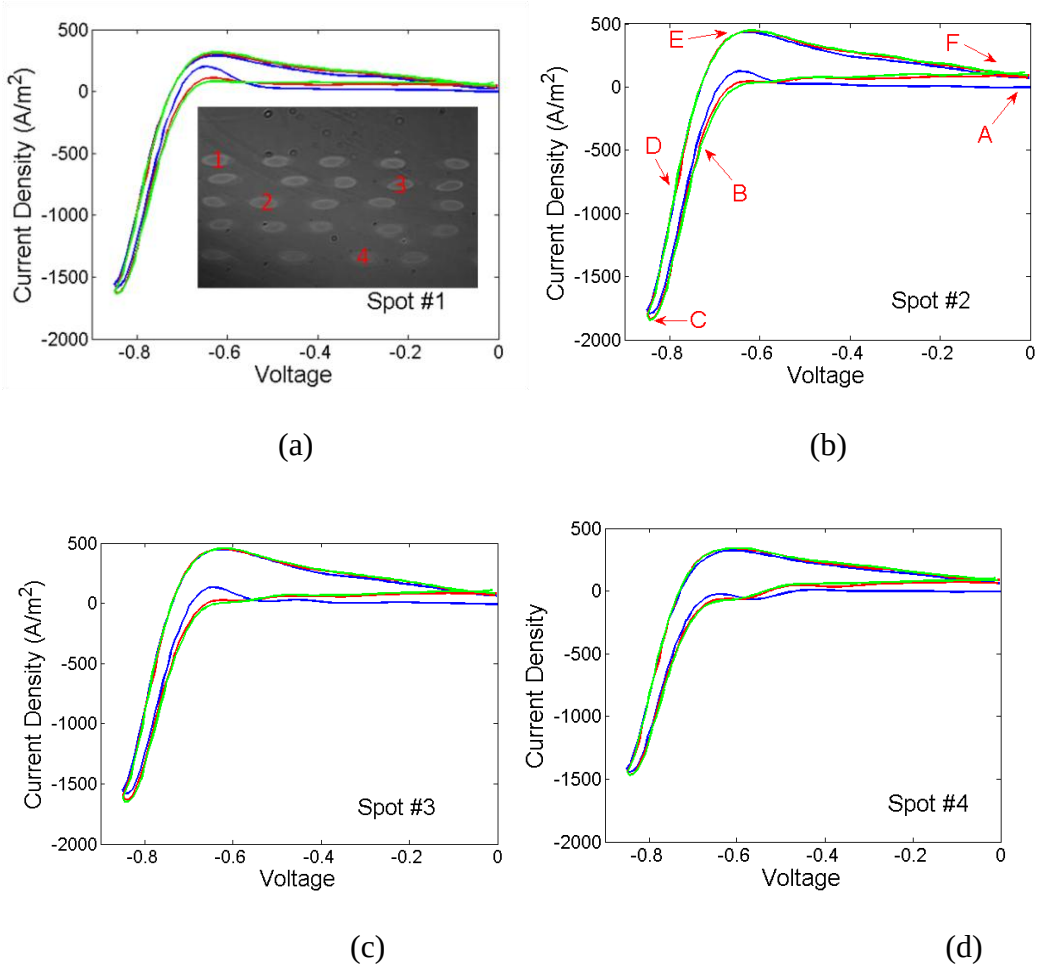

Figure 6.6. PECI current at different PtNP spots. (a) PECI current of spot #1. The inset shows the SPR image of PtNP array and the locations of spot #1 to #4 are pointed out in the inset image. (b) PECI current of spot #2. The A, B, C, D, E and

F point out the corresponding potentials of Figure 6.7. (c) and (d) are the PECI current of spot #3 and #4.

One of the important advantages of PECI method is the local current imaging capability. Figure 6.6 shows the PECI current at different PtNP spots and the spots locations are labeled in inset of Figure 6.6(a). All the curves have similar shape while the maximum current densities are slightly different. It is because the concentration of particle modified on different spots may vary.

Figure 6.7 demonstrates PECI current density image at different potential by 3D plots and it shows the spatial current density imaging ability of PECI method from another aspect. The amplitude of z-axis and the color map both represent the current density at different locations. The potentials of Figure 6.7 (A-F) have been labeled on the images and pointed out on Figure 6.6 (b). At beginning (0V) there is no current throughout entire surface (Figure 6.7(A)), when the potential decreases lower than -0.68V, the catalytic current begin to rise (Figure 6.7 (B)) until it reaches the peak (most negative) potential (Figure 6.7(C)). Note that Figure 6.7 (B), (C) and (D) are looks from negative current (negative z) direction. Each current dip represents a PtNP spot and they both have much bigger current at catalytic reaction potential compare with Au region (Figure 6.7 (B)-(D)). When the potential scans towards positive direction the current density (the absolute value) decreases (Figure 6.7 (D)) until it turns to positive current, and current peak locates at -0.622V (Figure 6.7(E)). If potential keeps increasing to 0V, the current drops back to zero (Figure 6.7(F)).

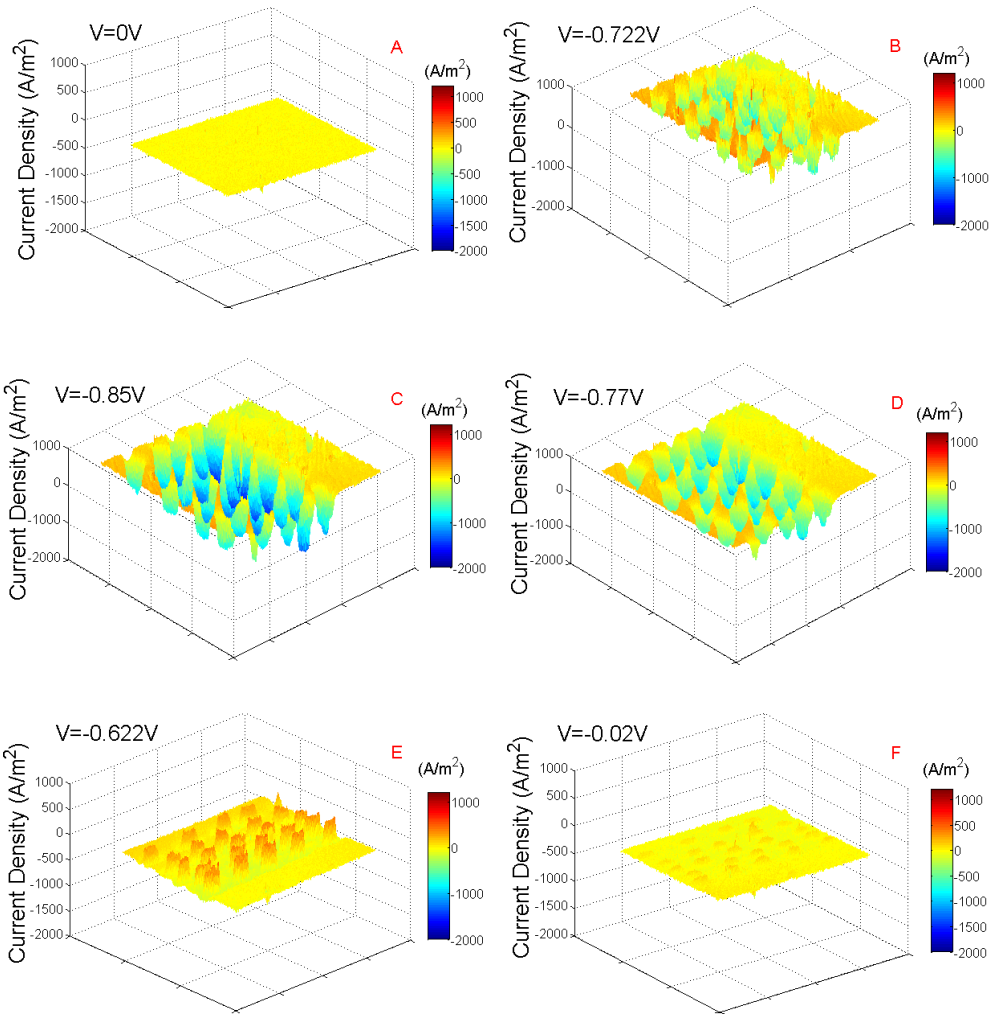

Figure 6.7. 3-D plots of PECI current images at different potentials. (A) to (F) are the PECI images at different potentials, the potentials was labeled on top of image and pointed out in Figure 6.6(b). Current density is represented by amplitude of z-axis and color map. Figure (B), (C) and (D) is projected from bottom of the plane (negative z-axis direction) and figure (A), (E) and (F) are projected from top of plane (positive z-axis direction).

Figure 7.8 shows the same images in Figure 7.7 on 2D. The color map shows the current density of pixel. The shape of the patterns can be recognized

easier than 3-D plot while the relative value between spots are more obvious in 3-D plots.

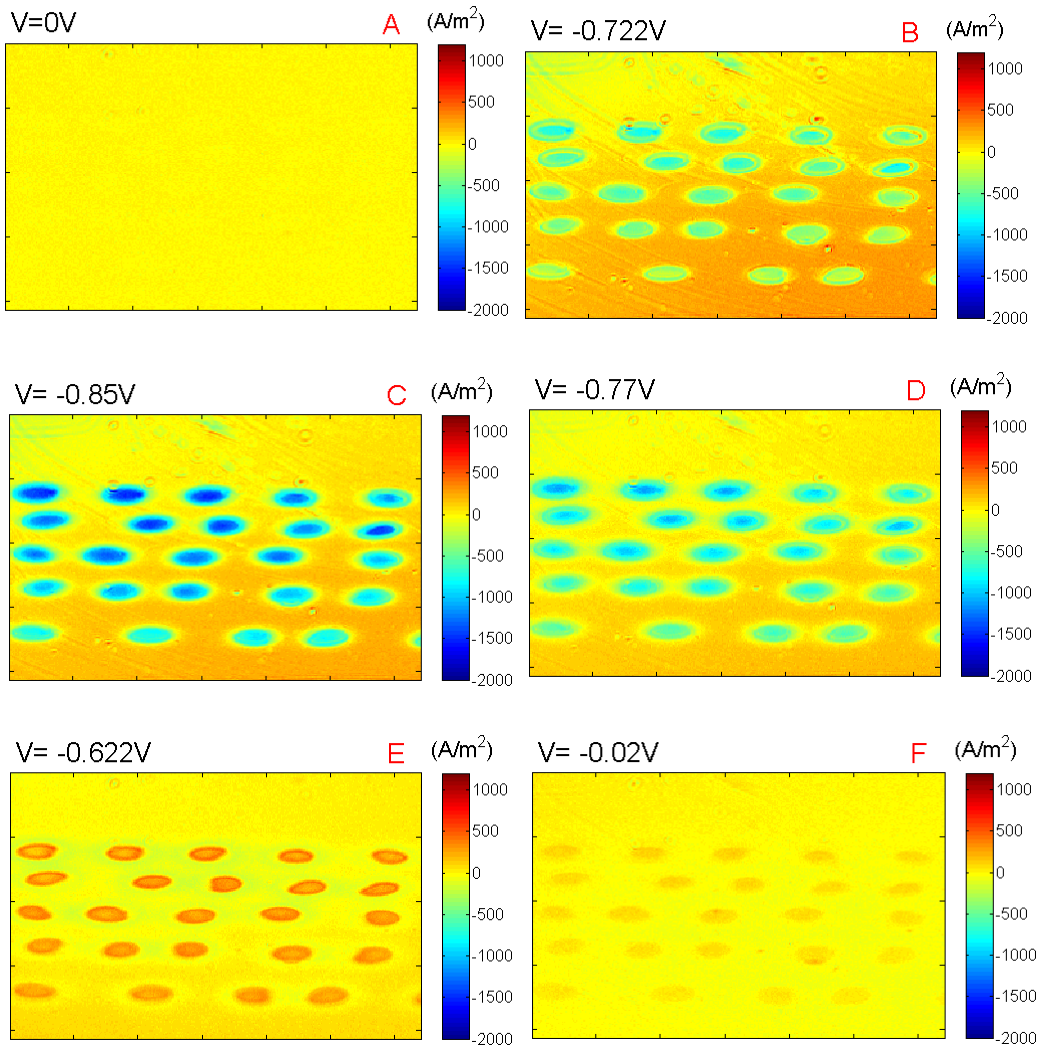

Figure 6.8. 2D plot of same images of Figure 6.7.

6.6. Different concentration of PtNP array

To prove the nanoparticle catalytic screening ability of PECI method, different concentration of PtNP array is created on Au surface by injecting different concentration of PtNP solution onto Au surface. The particle concentration and type is shown in Figure 7.8(b) where #1 row is modified with

no dilution PtNP solution and #2 to #4 rows are modified with 2, 4 and 8 times dilution (0.5X, 0.25X and 0.125X concentration) PtNP solution. There is one AuNP (5nm) row on the right side of array as control experiment. Figure 7.8(a) top image shows the SPR images of different concentration of PtNP arrays and bottom image shows the subtracted image between before applying potential and most negative potential. PtNP array cannot be easily distinguished from SPR image while the reaction helps enhanced the contrast and helps the detection of PtNP. AuNP is much more easily to see because the concentration of AuNP is higher and more AuNPs are modified onto Au surface.

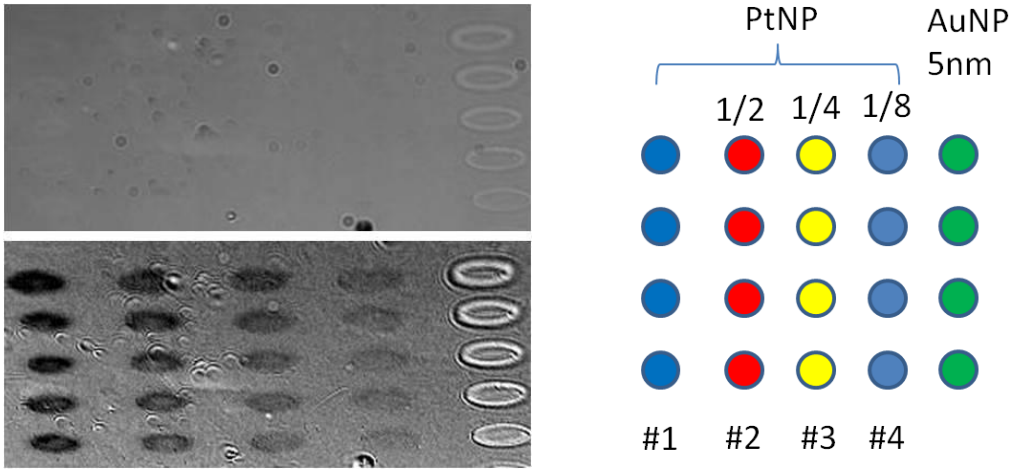

(a) (b)

Figure 6.9. Different concentration of PtNP spots. (a) Top: SPR image of different concentration PtNP array and AuNP array. Bottom: subtracted image between before apply potential and peak potential. (b) Scheme of different concentrations PtNP arrays and AuNP.

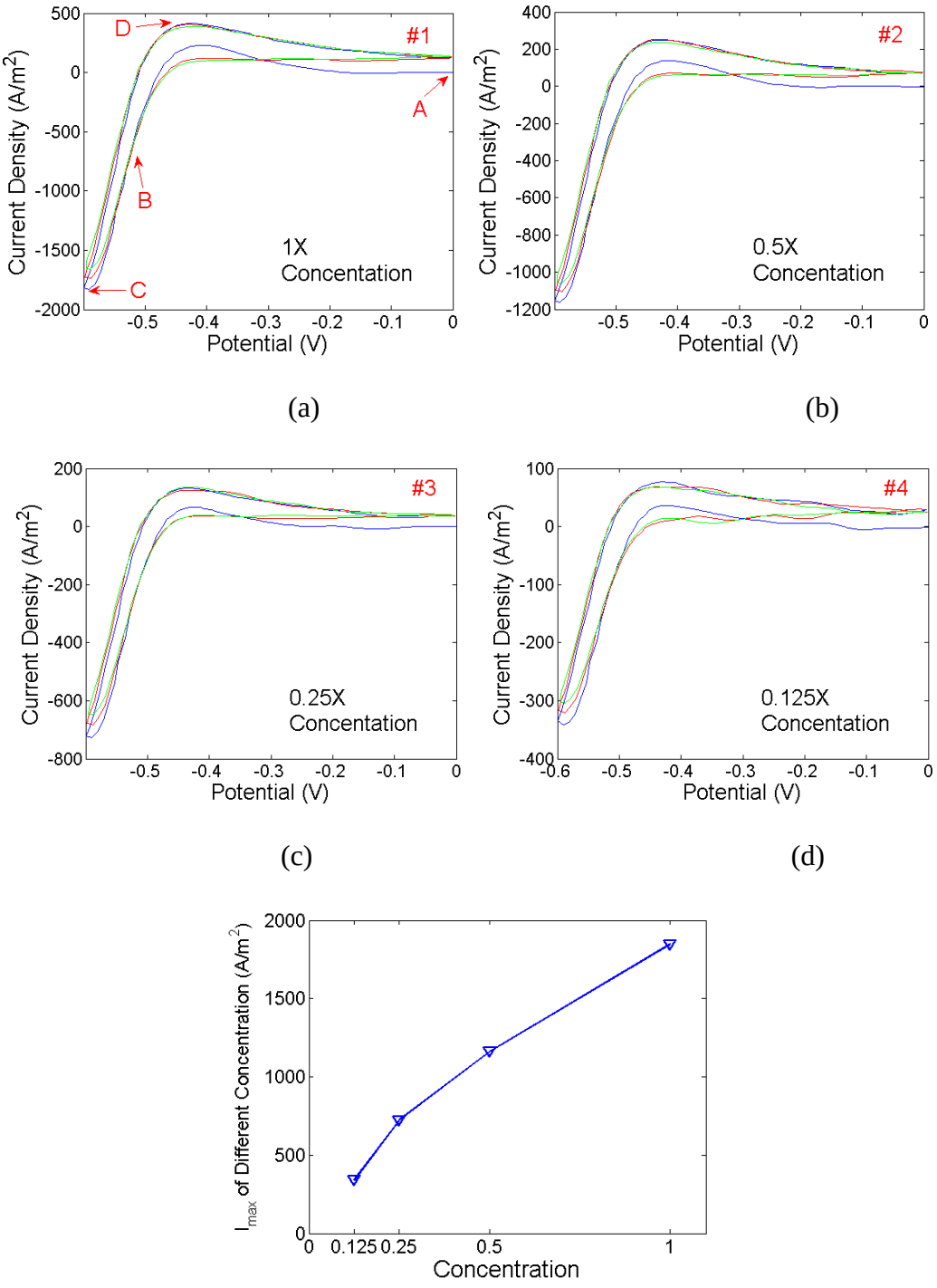

Figure 6.10. PECI current for different concentration of PtNP spots. (a) to (d) Corresponding PECI current curves for 1X, 0.5X, 0.25X and 0.125X

concentrations of PtNPs. (e) Relation between peak current density and PtNP concentration.

Figure 6.10 (a) to (d) show the PECI current density of different concentration of PtNP spots and Figure 7.10 (e) shows the relation between concentration of PtNP and peak current density. Higher concentration of PtNP will give more catalytic current and the relation between concentration and peak current density is linear (Figure 6.10 (e)). This demonstrates PECI method can be use for nanoparticle catalytic efficiency screening.

PECI current density images at different potential can also been plotted (Figure 6.11). Note that even within one spot, the current density is not uniform because of donut effect when printing array onto surface and there are more information about the local variation of PtNP concentration detection in next section.

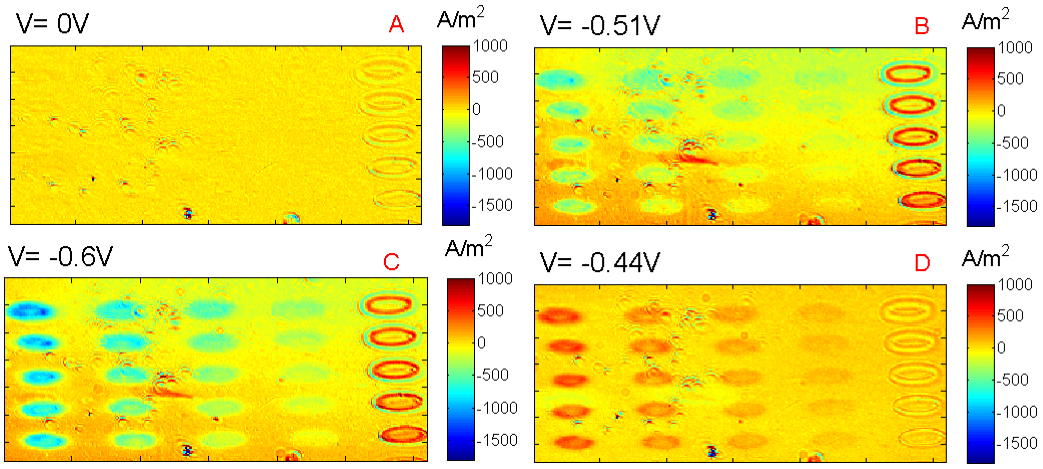

Figure 6.11. PECI current density images at different potentials. A to D, the potentials are pointed out on top of images and labeled out in Figure 6.10 (a).

6.7. Impedance method for PtNP detection.

In this section, a microscope SPR setup was used to obtain higher magnification image of PtNP array so detailed information from single spot can be available. A sine wave was applied to the PtNP array surface and potential ranges from -0.5V to -1.0V which covers the H_2 catalytic reaction. And the SPR images are processed by FFT pixel by pixel and re-plot the amplitude response at different frequency.

Figure 6.12 (a) shows the direct SPR image of PtNP spot, the PtNP region cannot be distinguished with bare Au region. It is because the amount of PtNP modified onto the surface is small and also because of interference pattern caused by the using of laser. Figure12(c) shows the fft of entire surface, since the potential 5Hz is applied, therefore at 5Hz there is a huge response and 10Hz and 20Hz components are harmonic frequencies. Figure 6.12 (b) and (d) shows the PECI response image at 5Hz and 10Hz, there is a small spot of PtNP in the center of image (scale bar is 6 μm), and on the left bottom corner there is a part of big PtNP spot.

The PtNP region can be easily distinguished from Au area because only PtNP regions generate the catalytic current and this amplifies the difference between PtNP and Au region. Thus the EC reaction can amplify the difference between PtNP and Au and improves the detection limit of PtNP. Another advantage for impedance method to detect PtNP is lower noise, and that is because the FFT of a periodic signal is equivalent to average the different cycles, therefore the better contrast images can be obtained than just one cycle. And also

from PECI images, the local PtNP concentration can be measured by the PECI response amplitude.

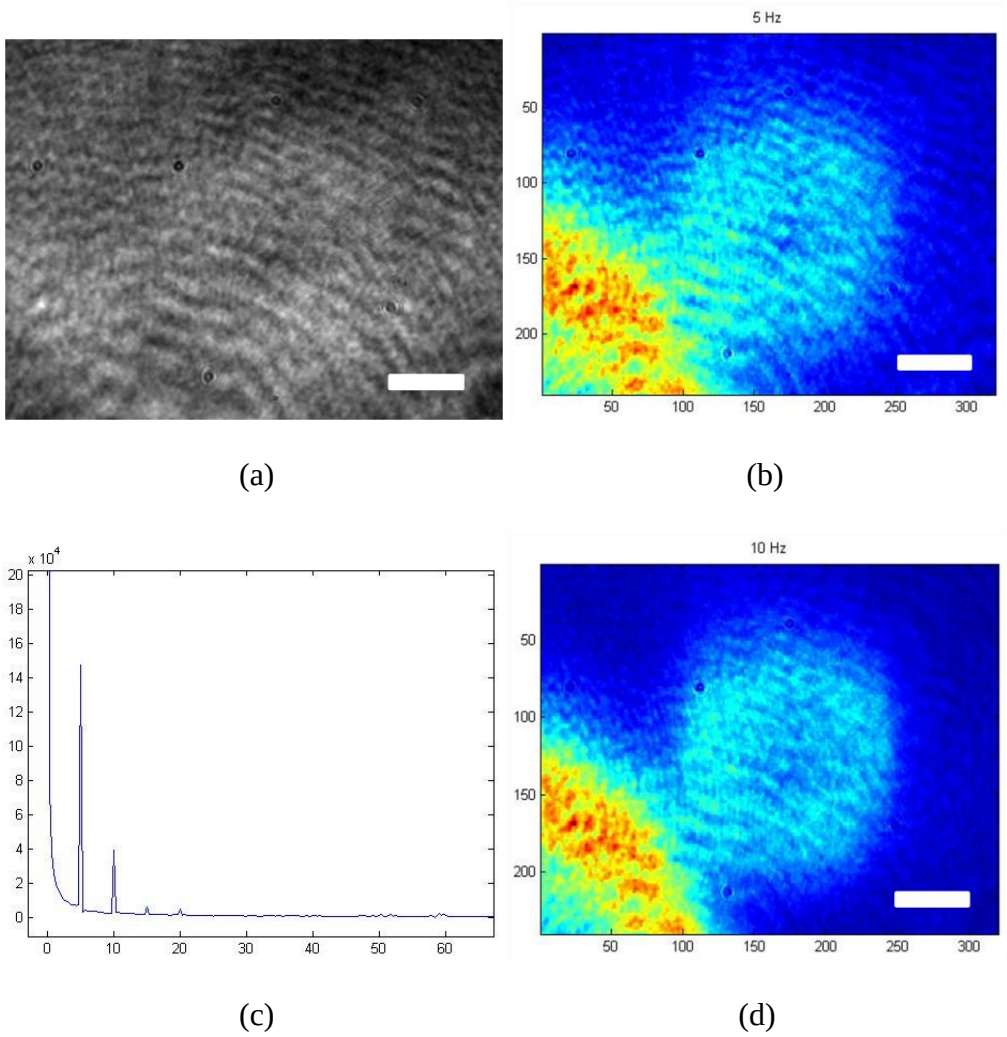

Figure 6.12. Impedance measurement of low concentration PtNP microarray. (a) SPR image of PtNP spot. (b) and (d) FFT image at 5 Hz and 10 Hz. (c) FFT result of whole image.

In the Figure 6.13 (a), the left half of image is covered by PtNP spot and it is easier than Figure 6.12 to distinguish between PtNP and Au region due to the higher concentration of PtNP. Figure 6.13 (c) shows the fft result of whole surface

and Figure 6.13 (b) and (d) are the fft images at 5Hz and 10Hz. The local PtNP concentration is proportional to the H2 evolution reaction signal and therefore proportional to the fft image and PtNP concentration distribution can be observed very easily. The edge has much more PtNP than the center of the spot because of donut effect.

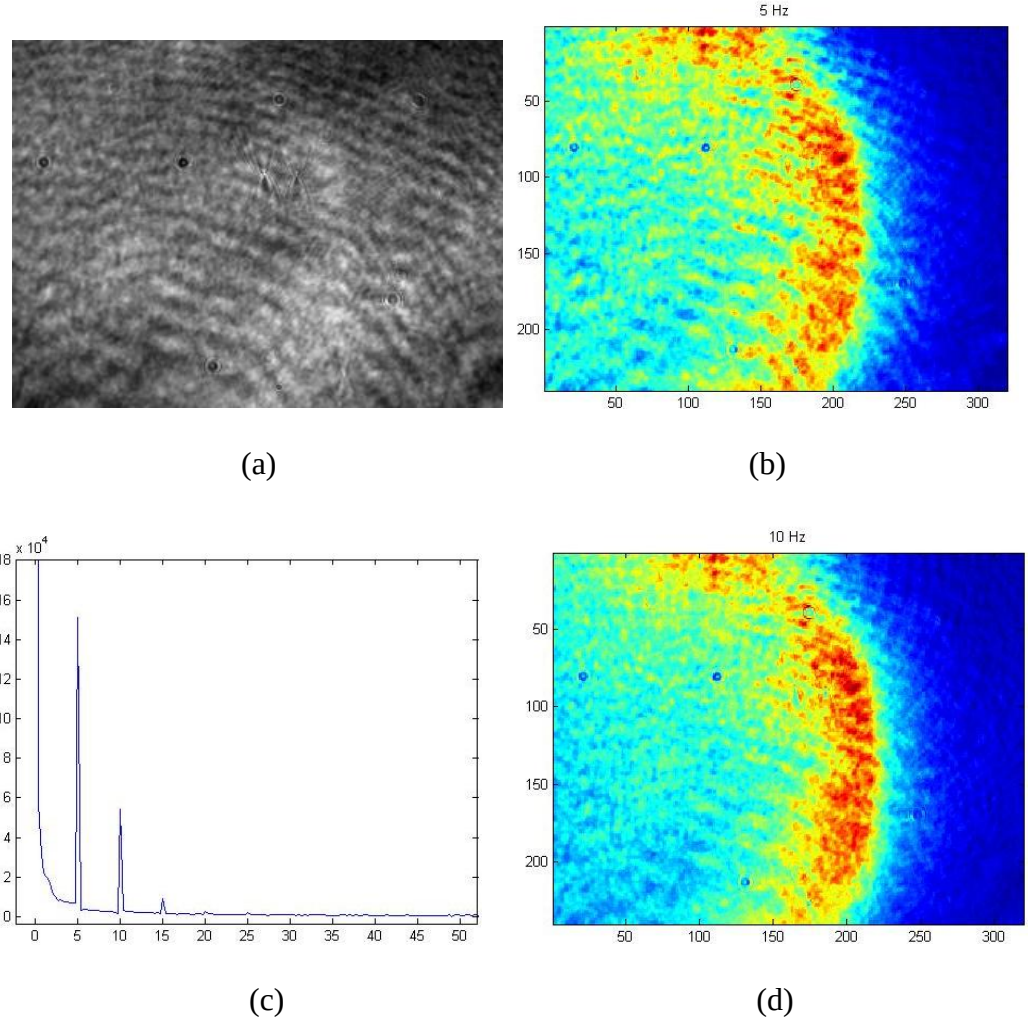

Figure 6.13. Impedance measurement of high concentration PtNP microarray. (a) SPR image of PtNP spot. (b) and (d) FFT image at 5 Hz and 10 Hz. (c) FFT result of whole image.

6.8. Charging effect and angle selection

As discussed in previous section, the modification of PtNP onto Au surface will not change the charging properties of Au. To further prove that, a charging potential, from 0V to -0.5V in which the H_2 catalytic reaction have not happened, was applied to PtNP microarray. SPR image is shown in inset of Figure 6.14 (b) where the left side is PtNP region and right side is Au surface. Figure 6.14 (a) shows the SPR response of two regions and they match very well on both amplitude and shape. This proves the PtNP modified area has same charging response with Au surface and by subtraction Au area's response from PtNP area's response, the charging effect can be eliminated and the rest of response is purely due to the catalytic reaction (faradaic current). Therefore eq(4) is suitable to use to calculate catalytic reaction current. Figure 6.14 (b) shows the current measured by the conventional method.

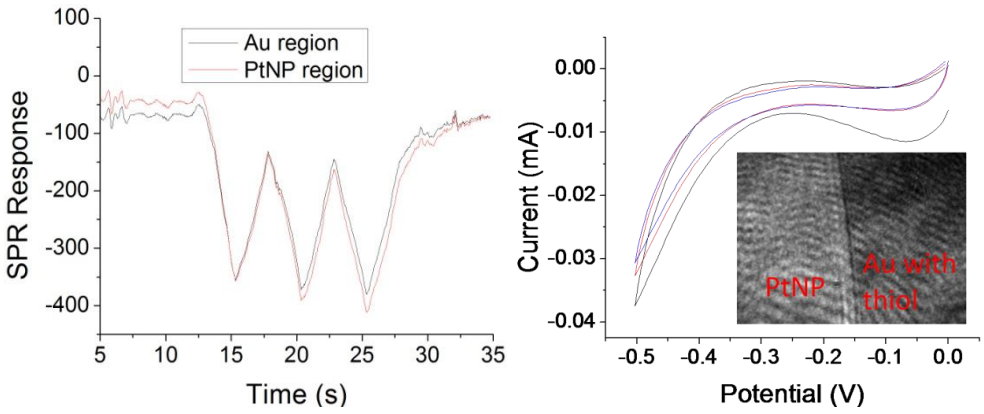

(a) (b)

Figure 6.14. Charging effect of PtNP array. (a) SPR response of PtNP and Au region. (b) Charging current measured by conventional method. Inset: SPR image of PtNP spot and Au region.

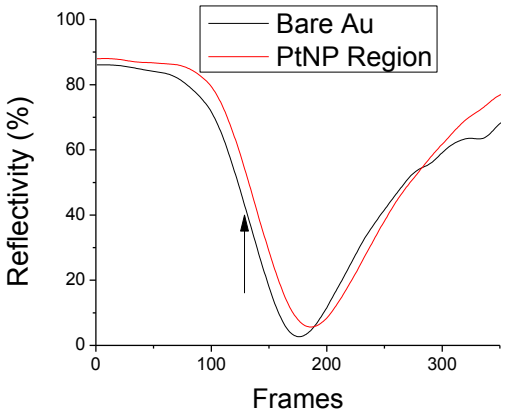

Figure 6.15. Sensitivity curve of PtNP region and Au region.

PtNP region's charging effect has been proved identical with Au surface, sensitivity of PtNP also need to calibrate. Figure 6.15 shows the SPR response of PtNP and Au region at different angle, and the slow for different regions are same and only PtNP's curve shifts. This proves modification of PtNP will not affect the sensitivity of PECI, it only shifts the SPR response curve. As long as the incident angle is located in linear range (pointed out by the arrow in the Figure 6.15), the PtNP and Au region will have same sensitivity.

CHAPTER 7

MEASURING SURFACE CHARGE DENSITY AND PARTICLE HEIGHT USING SURFACE PLASMON RESONANCE

7.1 Introduction

Surface charge density is a fundamentally important quantity and measuring it has a broad impact on many applications. For example, electrostatic charge on sensor surfaces has profound effects on DNA hybridization and protein binding in microarray technologies[105]. Quantification of surface charge density can lead to a better understanding of biomolecular interactions on surfaces. In addition, measurement of surface charge density can be used as a signal transduction mechanism to detect molecular binding events on surfaces[106]. Several methods have been developed to measure surface charge density. One is potentiometric titration, which is limited to measuring the average charge density of an entire surface[107, 108]. Atomic force microscopy can probe local charge density with high resolution,[109, 110] but it is slow and can cover only a small sample area[111, 112]. Reflection interference contrast microscope has also been used to measure the surface charge density[106, 113], but it requires well defined, smooth and spherical particles in order to obtain well defined interference patterns.

In this chapter a SPR method to measure surface charge density is developed. Comparing to the previously reported methods, the SPR approach has the following distinct features: 1) It offers spatial resolution (sub-micron

resolution[114]) when operated in the imaging SPR mode which is ideal for high throughput mapping of heterogeneous surface charge distribution. 2) SPR can measure the local coverage of molecules, making it possible to study the correlation between the coverage and surface charge density. 3) It allows one to monitor various surface processes, including molecular binding, on the same surface after determination of surface charge density. 4) It can be used to measure the charge density of not only surfaces but also the particles, including cells. 5) Finally, the approach may be used to study the interactions between the particles and surfaces.

SPR is extremely sensitive to refractive index changes near a metal film (sensor surface), which has been used as real-time and label-free technique for many applications, ranging from environmental studies to biomedical research. Most SPR applications, to date, are based on the detection of molecular binding on sensor surfaces[115]. Since the evanescent field associated with SPR penetrates into the solution phase over a distance of ~200 nm, SPR probes refractive index changes within the entire penetration depth. The intensity of the evanescent field decays exponentially, making SPR also an extremely sensitive tool to measure the distance between an object and the sensor surface. The object could be macromolecules, cells, nanoparticles or glass beads, so long as its index of refraction is different from that of the liquid medium. In this chapter, this sensitive distance dependence has been demonstrated that it can be used to determine the surface charge density and particle-height.

7.2 Theory

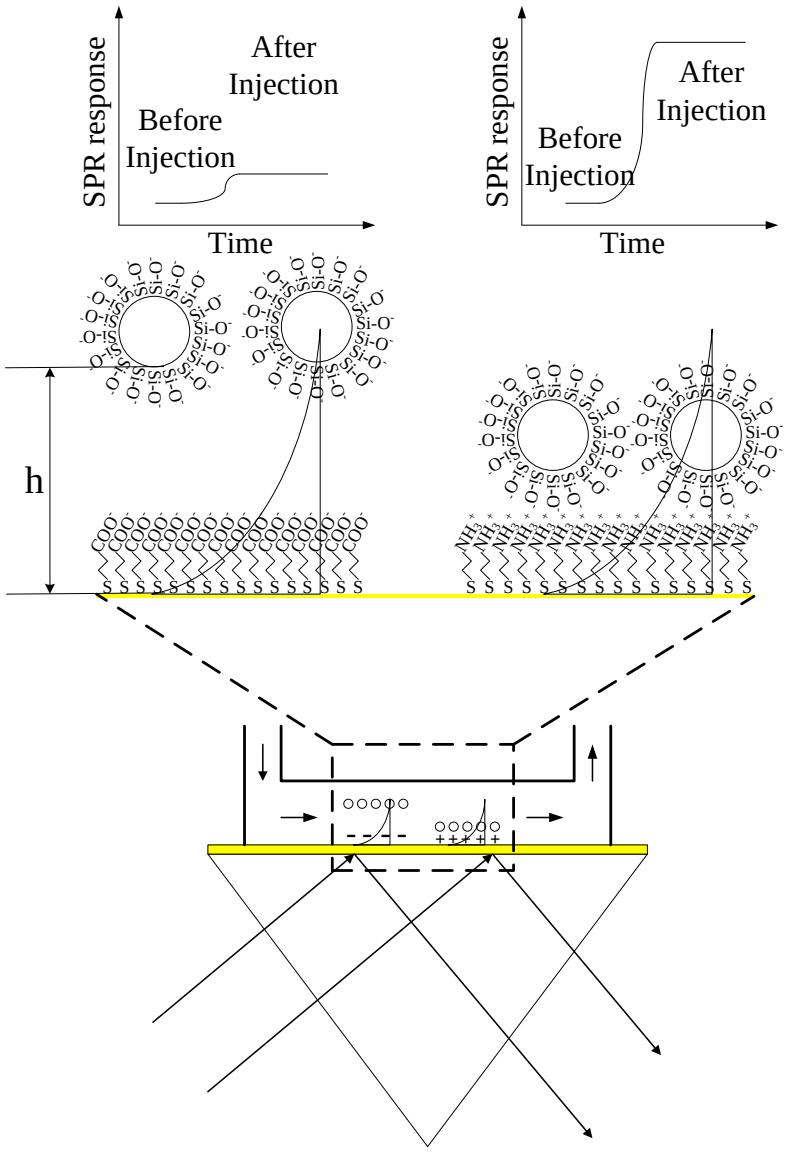

Figure 7.1. Scheme of the surface charge density detection principle.

Figure 7.1 illustrates the basic principle of the method, in which charged silica particles are used as probes to measure the surface charge density of a sensor chip. If choosing the silica particle probes with the same charge as the

sensor surface, then the electrostatic repulsion will prevent the particles from reaching the surface. The equilibrium height of a silica particle from the surface depends on the electrostatic force between the particle and the surface. Since the equilibrium height can be accurately measured with SPR, one can thus determine the surface charge density.

A quantitative relation between surface charge density and the particle height can be derived based on the balance between two forces, electrostatic repulsion that tends to drive the particles away from the surface and the gravitational force that moves the particles towards the surface.

The potential energy, U(h), of a particle near a charged surface in an electrolyte is given by[113, 116-120]:

$$U(h) = \Psi_0 e^{-\kappa h} + F_g h \quad (1)$$

In Eq. 1, F_g is the gravitational force on the particle and Ψ_0 is the effective electrostatic potential, which are expressed as

$$F_g = \left(4/3\right)\pi \cdot r^3 \left(\rho_p - \rho_f\right) g \quad (2)$$

and

$$\Psi_0 = 64\pi\varepsilon\varepsilon_0 r \left(\frac{kT}{e}\right)^2 \tanh\left(\frac{e\psi_p}{4kT}\right)\tanh\left(\frac{e\psi_s}{4kT}\right), \quad (3)$$

respectively, where κ^{-1} is the Debye length, h is the particle height measured from the bottom of the particle to the surface, r is the particle's radius, ε is the relative permittivity of water, ε_0 is the vacuum permittivity, k is Boltzmann's constant, T is temperature, e is electron charge, ψ_p is the surface potential of the particle, ψ_s is the potential of the charged surface.

At the equilibrium:

$$\frac{\partial U(h)}{\partial h} = -\kappa\Psi_0 e^{-\kappa h} + F_g = 0. \quad (4)$$

Combining Eqs. 3 and 4:

$$\frac{F_g e^{\kappa \cdot h}}{\kappa} = 64\pi\varepsilon\varepsilon_0 r\left(\frac{kT}{e}\right)^2 \tanh\left(\frac{e\psi_p}{4kT}\right)\tanh\left(\frac{e\psi_s}{4kT}\right). \qquad (5)$$

According to Eq. 5, the surface potential can be expressed as a function of particle height, h, as

$$\psi_s = \gamma \tanh^{-1}\left(\zeta e^{\kappa \cdot h}\right), \qquad (6)$$

where

$$\gamma = \frac{4kT}{e} \qquad (7)$$

and

$$\zeta = \frac{F_g / \kappa}{64\pi\varepsilon\varepsilon_0 r\left(\frac{kT}{e}\right)^2 \tanh\left(\frac{e\psi_p}{4kT}\right)} \quad . \qquad (8)$$

The dependence of surface charge density $\sigma(\psi_s)$ on surface potential, ψ_s, is described by the Poisson-Boltzmann equation, which leads to the Grahame equation[121]

$$\sigma(\psi_s) = \frac{2\varepsilon\varepsilon_0 kT\kappa}{e}\sinh\left(\frac{e\psi_s}{2kT}\right) . \qquad (9)$$

By substituting Eq. 6 into Eq. 9, the relation between the surface charge density and particle height is obtained, which is given by

$$\sigma(h) = \frac{2\varepsilon\varepsilon_0 kT\kappa}{e}\sinh\left(\frac{e\gamma \tanh^{-1}(\zeta \cdot e^{\kappa \cdot h})}{2kT}\right) . \qquad (10)$$

Equation (10) describes the relationship between the surface charge density and particle height. Using Eq. 10, together with Eqs. 8 and 2, the surface charge density, σ, is plotted as a function of the distance, h (Figure 7.2a). The plot shows that the logarithmic surface charge density is approximately proportional to the particle height. Once the equilibrium height is known, then the surface charge density can be determined by using this relation.

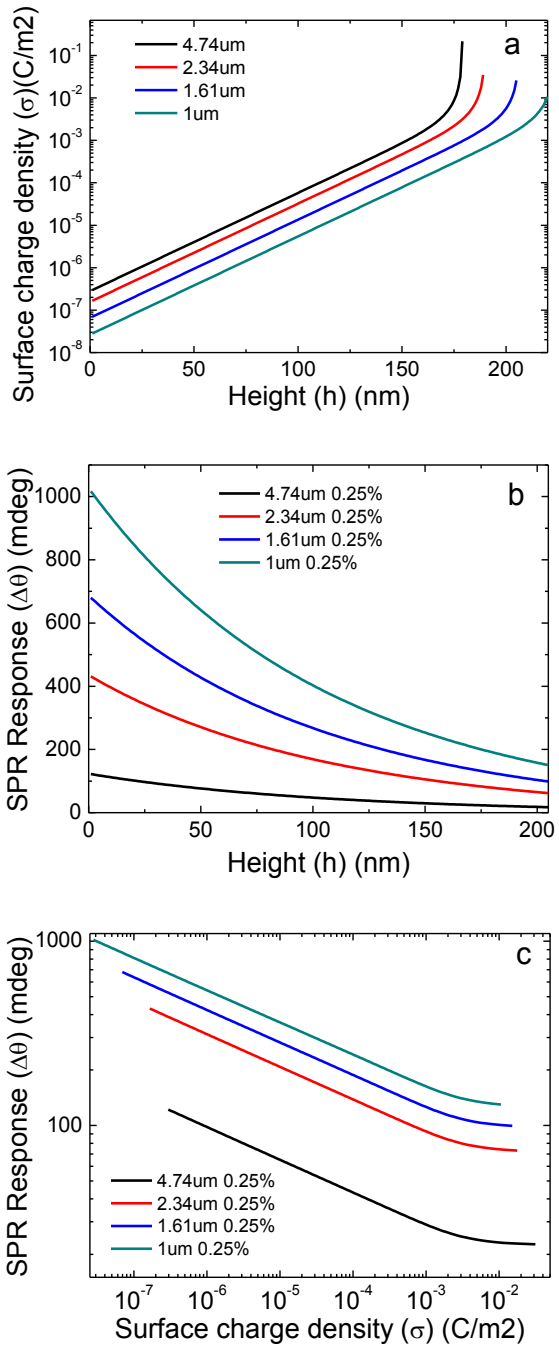

Figure 7.2. Calculation surface charge density vs SPR response. (a) Surface charge density vs. particle equilibrium height. (b) SPR response vs. particle equilibrium height. (c) SPR response vs. surface charge density.

Since the equilibrium height of the particles can be measured using SPR, numerical calculation[122, 123] of the dependence of the SPR angular shift vs. the height for silica particles with different diameters (Figure 7.2b) is performed. A MATLAB program was developed to simulate the relation between SPR angle shift and particle height using a stratified medium model.[122, 123] In the model the SPR sensitivity distribution (along z direction) was simulated by treating the dielectric medium (electrolyte and particles) near the sensor surface as a stack of thin layers, each layer is described by two parameters, thickness and index of refraction. For a layer of silica particles near the Au surface, each thin layer contained both silica and electrolyte and the average index of refraction was thus used. The average index of refraction was calculated from the volume ratio between silica and electrolyte, which varies with the particle height and also depends on particle size and concentration. The layer thickness was chosen to be 1 nm, which is much smaller than the field penetration distance and particle sizes. Fig 7.2(b) shows the SPR response of 0.25% (mass ratio) simulated with this procedure.

The simulation shows that the SPR response decreases rapidly with the height, due to the exponential decay of the evanescence field from the surface into the fluid phase. Combining Figure 7.2a and b, the relation between the SPR response and surface charge density is plotted in Figure 7.2c. It shows that within a broad range of surface charge density, the logarithm of the SPR angular shift decreases linearly with the logarithm of the surface charge density, which can be readily used to determine the surface charge density based on measured SPR

angular shift. A theoretically-predicted error can be obtained from Figure 1c as well. Surface charge density and SPR response have the relationship as $\ln\delta = K\ln\theta$, where K is a constant in the linear region (Figure 7.2c), and the error can be calculated from the derivative of equation, $\frac{\Delta\delta}{\delta} = K\frac{\Delta\theta}{\theta}$. Note that at different surface charge density (δ) the SPR response (θ) will be different, thus the noise will be $\frac{\Delta\delta}{\delta}$ will be different. For 1.61um 0.25% particles K=-5.85 and the noise level of our SPR equipment is 0.1 mdeg, the theoretically predicted error ($\frac{\Delta\delta}{\delta}$) varies from 0.087% to 0.39% when surface charge density varies from 1e-7 to 1e-2 C/cm^2.

As shown in Figure 7.2c, the relation between the SPR response and the surface charge density depends on the particle size. For a given change in the surface charge density, smaller particles produce larger SPR responses. This observation can be understood based on geometrical considerations. Small particles have larger interaction volumes within the evanesce field (Figure7.3). This can be understood based on simple geometrical considerations. Considering a monolayer of closely packed particles on a sensor surface, and evanesce field with penetration depth, L, the interaction volume is $\pi L^2R-\pi L^3/3$, where R is the radius of the particle. The SPR angle is determined by the ratio of the interaction volume to the evanesce field volume. The later is πR^2L, so the ratio is $L/R-L^2/(3R^2)$, which decreases with R for R> 2L/3. L is about 200 nm and the smallest particle studied here has a radius of ~800 nm, so the condition R> 2L/3 is satisfied, and that smaller particles lead to greater SPR responses.

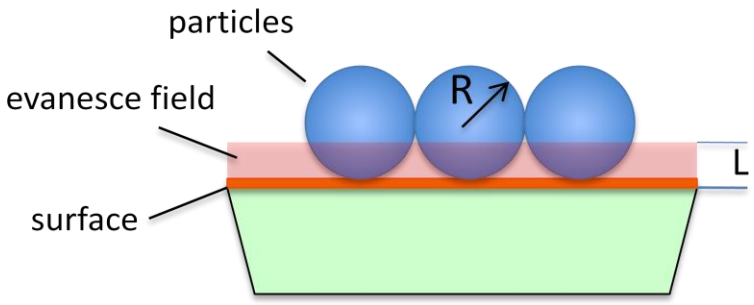

Figure 7.3. Schematic diagram of particle size effect. Smaller particles have larger effective interaction volume with the evanesce field near the surface.

However, if the particle is too small, then Brownian motion becomes important and a more complete theory including thermal fluctuations will be needed. Brownian motion becomes important when the gravitational energy, $\frac{4\pi}{3} r^3 (\rho_p - \rho_f) gh$ reduces to the same level as the thermal energy, $k_B T$, or $\frac{4\pi}{3} r^3 (\rho_p - \rho_f) gh \approx k_B T$. Assuming h~200 nm, the radius of the particle is about 0.7 μm.

Another approximation made in deriving Eqs. 1-10 is that the negligence of the van der Waals interaction between the particles and the surface. The van der Waals force between a silica particle and a flat surface is given by $F_{vdw}=AR/h$, where A is the Hamaker constant.[124] For water, $A=1.5 \times 10^{-19}$ J, the van der Waals force for a 1 μm-diameter particle in contact with the surface is $\sim 10^{-17}$ N, which is several orders of magnitude smaller than the gravitational force, $\frac{4\pi}{3} r^3 (\rho_p - \rho_f) g \sim 10^{-14}$ N. This analysis justifies the approximation of neglecting the van der Waals interaction.

SPR impedance method [90] can also be used to determine surface charge and impedance. The method relies on the dependence of SPR frequency on the surface charge density, which leads to a surface-charge dependent SPR angular shift given by $\Delta\theta_R = \beta\Delta\sigma$, where $\Delta\theta_R$ is the SPR angular shift and $\Delta\sigma$ is the surface charge change (is given by, where the β describes the sensitivity). The sensitivity, β, was found to be 0.021 deg/C/m^2.[90] In contrast, the sensitivity of the present method is 1 deg/C/m^2 for an equilibrium height of 200nm, which is 2 orders of magnitude more sensitive than the direct method. If decreasing the height to zero, the sensitivity increases to 10^6 deg/C/m^2.

7.3 Experiment and setup

HPLC-grade 3-Mercaptopropionic acid (3-MPA), Cysteamine hydrochloride, sodium chloride and sodium acetate anhydrous were purchased from Sigma-Aldrich (St. Louis, MO). 3-MPA and Cysteamine hydrochloride were used as received. Glacial acetic acid was supplied by Mallinckrodt chemicals (Philipsburg, NJ). Phosphate buffer saline (PBS) tablet was purchased from Calbiochem (Darmstadt, Germany). Silica particles, with diameters of 1.00um, 1.61um, 2.34um and 4.74um, were purchased from Bangs Laboratories (Fishers, IN). Zeta potentials of the silica particles were measured using Zetasizer Nano (Malvern Instruments, Worcestershire, UK). Ultrapure water (18.2MΩ.cm) from ELGA was used for preparing all the solutions.

BI-2000 SPR system (Biosensing Instrument, Tempe, AZ, www.biosensingusa.com) was used for SPR measurements. The wavelength of

the incident light is 635 nm. The system is equipped with a flow cell made of a PEEK (polyaryletheretherketone) cell block and a PDMS (Polydimethylsiloxane) gasket containing two channels. It has a valve control system that can switch the flow between single channel mode and serial channel mode. In the single channel mode, a sample solution injected via an injection valve flow through either channel 1 or channel 2, while in the serial channel mode the sample flows through the two channels sequentially. Before each experiment, the flow cell was cleaned with ethanol and DI water. The SPR sensor chip was a BK7 glass cover slide coated with 1.5nm chromium followed by 47nm gold by thermal evaporator at high vacuum ($3x10^{-6}$ Torr).

Before each experiment, a gold sensor chip was rinsed by ethanol and deionized water and then annealed with a hydrogen flame to remove possible surface contamination. The chip was modified using the flow through system of the SPR instrument. For example, 10 mM 3-MPA was injected into channel 1 to create a negatively charged surface and 10 mM cysteamine hydrochloride into channel 2 to create a positively charge surface using the single channel mode. The surface modification processes were monitored with the SPR in real time. As the molecules bound to the gold surface, the SPR signal increased and eventually reached a steady value, indicating the formation of a full monolayer coverage. All experiments were carried out using a flow rate of 60 μL/min.

Different solutions, including acetate buffer and NaCl solutions, were used as running buffers. NaCl solutions with concentrations varying from 0.1mM to 10mM were used to test the electrical double layer screening effect. The acetate

buffer was prepared by mixing of 37mM sodium acetate anhydrous and 10mM glacial acetic acid, which was diluted to 2mM, 1mM, 0.5mM, 0.25mM and 0.1mM. All the buffers were used immediately after preparation to minimize possible contamination.

The silica particle sample received from the vendor contained 10% (by mass ratio) silica particles suspended in deionized water. Before each experiment, the sample was rinsed 5 times with deionized water and extracted by centrifuge after each rinsing step. Different amounts of silica particles were then added into the acetate buffers to reach final particle concentrations at 0.0625%, 0.125%, 0.25%, 0.5% and 1%. The zeta potentials of the silica particles were determined to confirm the surface charges of the particles.

7.4. Ionic strength and particle size effect

One of the key assumptions in deriving Eq. 10 is that the electrostatic force between the particle and surface is determined by the Poisson-Boltzmann equation. An important prediction of the Poisson-Boltzmann equation is that the electrostatic force depends on the ionic concentration via the Debye length, κ^{-1}, which measures the screening length of the electrostatic force by the ions. For monovalent ions, $\kappa^{-1} \approx 0.3nm/\sqrt{c[M]}$, where c is the ionic concentration in molarity, showing that the Debye length decreases with the ionic concentration. To verify the theory, the particle height as a function of ionic concentration (0.1 to 10 mM NaCl solution) has been measured. Note that the change in the ionic concentration also cause a change in the solution pH from 6.2 to 6.0, but the pH

change is small and not expected to change the electrostatic force between the particle and the surface.

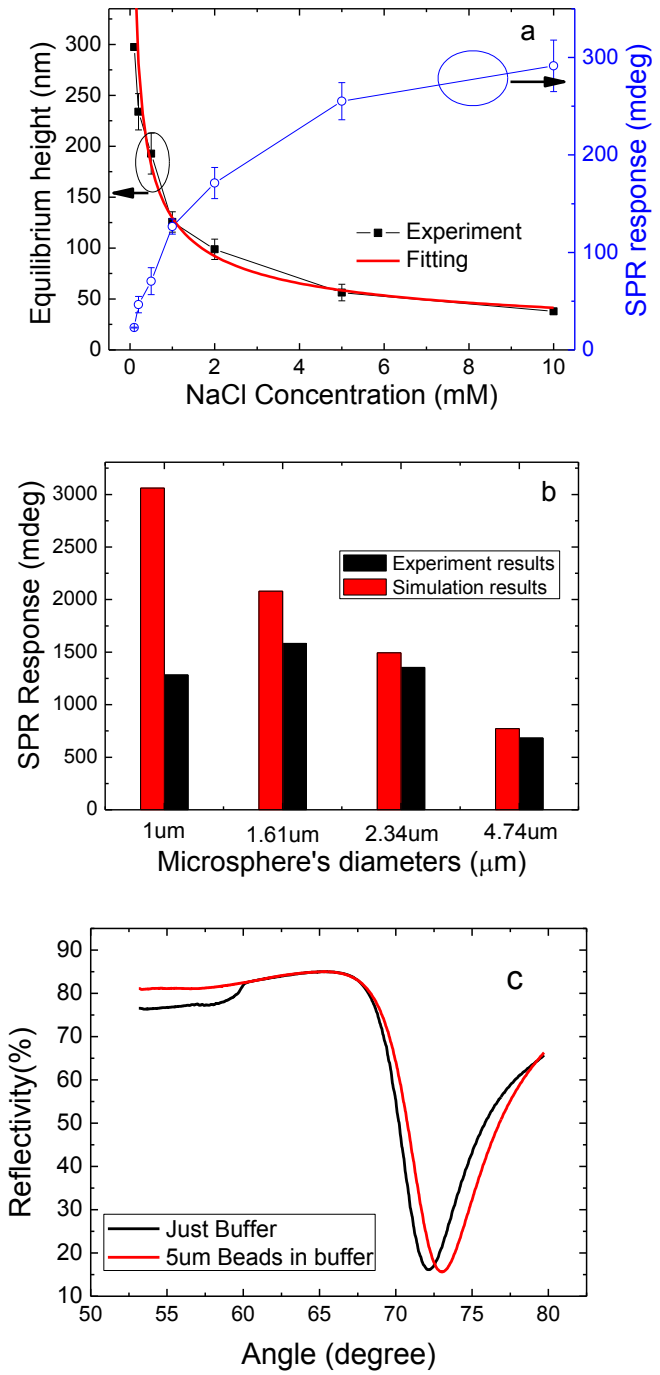

Figure 7.4. Ionic strength and particle size effect. (a) Experimental (solid squares) and theoretical (red line) equilibrium heights vs. NaCl concentration. The 2.34um

0.25% silica particle was used for measurements. The SPR response vs. NaCl concentration was also plotted. (b) Experimental and theoretical SPR responses for particles with different diameters. (c) Measured SPR profiles with (red curve) and without (black curve) the presence of full monolayer 5 μm silica beads in 0.5mM acetate buffer.

Figure 7.4a shows the SPR response (blue curve) of 0.25% 2.34 μm-diameter silica particles as a function of NaCl concentration. The sensor surface was modified with 3-MPA monolayer, so the balance between the electrostatic repulsion and gravity determines the equilibrium height. Using the relation shown in Figure 7.2b, the particle height vs. NaCl concentration (black curve, Figure 7.4a) is determined. As expected, the equilibrium height decreases with the ionic concentration. The experimental data is fitted using Eq. 10 with fitting parameters, σ=-2mC/m^2 and ψ_p=-31mV. The fit is excellent and the fitting parameter, σ matches closely with the independently measured values (this will be returned later). The second fitting parameter, ψ_p=-31 mV, is also in close agreement with the independently measured,[125] and calculated values (-30.5mV) reported in literature[121]. The quantitative agreement between the experimental data and theoretical prediction supports the simple theory described in the principle section. Note that the variation in the NaCl concentration also introduces a change in the refractive index of the medium. The angle shift due to different NaCl concentrations is measrued before each experiment, which was found to be relatively small (< 11 mDeg), and subtracted it out from the total signal.

The theory described in the theory section also predicts that smaller particles produce greater changes in the SPR responses than the larger particles and thus leading to more sensitive detection of surface charge density (see Figure 7.2c). This is because that the smaller particles have larger interaction volumes within the evanescent field near the SPR sensor surface. In order to verify the prediction, SPR responses to silica particles with various diameters was measured. Since the SPR response depends on not only the size but also the coverage of the particles, a complete coverage of the sensor surface is ensured with the particles in each experiment. This was achieved by 1) using sufficiently concentrated particle solutions and 2) modifying the surface with cysteamine.HCl to create a positively charged surface that attracted the particles onto the surface.

Numerical simulation of the SPR response vs. particle size using procedures described in section 7.2 is carried out as well. Note that the distance between Au surface and particle was set at 1 nm to represent the thickness of Cysteamine.HCl monolayer. Both the experimental and simulated SPR responses vs. particle size are shown in Figure 7.4b. For 4.74 μm- and 2.34 μm-diameter particles, the simulation and experiment are in good agreement. The small errors between simulation and experiment results come from the imperfect monolayer coverage. Deviations between the simulated and measured SPR responses begin to appear for the 1.61 μm- and 1 μm-diameter particles. While the dynamic range of the SPR setup may affect the result for the small particles, Brownian motion effect is expected to play an increasing role as the particles decrease in size. The estimated critical size, below which Brownian motion becomes non-negligible, is

~1.4 μm. This value is consistent with the observation shown in Figure 7.4b. It is important to note that although Eq. 10 will no longer hold when Brownian motion becomes important, the method of measuring surface charge density based on SPR should still work as long as the electrostatic force affects the distribution of the particles near a charged surface.

The presence of particles on the surface may introduce scattering to the evanescent field, which would increase the intensity at resonance and distort the SPR profile. SPR profiles (reflection vs. angle) in the presence and absence of full monolayer of 5 μm particles have been measured. Here the full monolayer corresponds to the formation of a closely pack layer of particles on the surface which is confirmed directly with an optical microscope and indirectly based on the saturation in the SPR angular shift. As shown in Figure 7.4c, the SPR profile in the presence of particles remains well defined and the intensity at the resonant angle remains unchanged comparing to the profile measured without the particles. SPR response has been simulated by representing the particles with a homogenous layer with refractive index calculated from the particle packing density and refractive indices of water and the silica particles, and found that the measured shift in the resonant angle due to the presence of the particles is in good agreement with the calculated angular shift (Figure 7.5). The effective refractive index of the layer was calculated from the particle packing density determined the geometry and refractive indices of water and the silica particles. The calculated shift in the resonant angle due to the presence of the particles is in good

agreement with the measured angular shift. These observations indicate that the scattering is relatively small for the purpose of the present project.

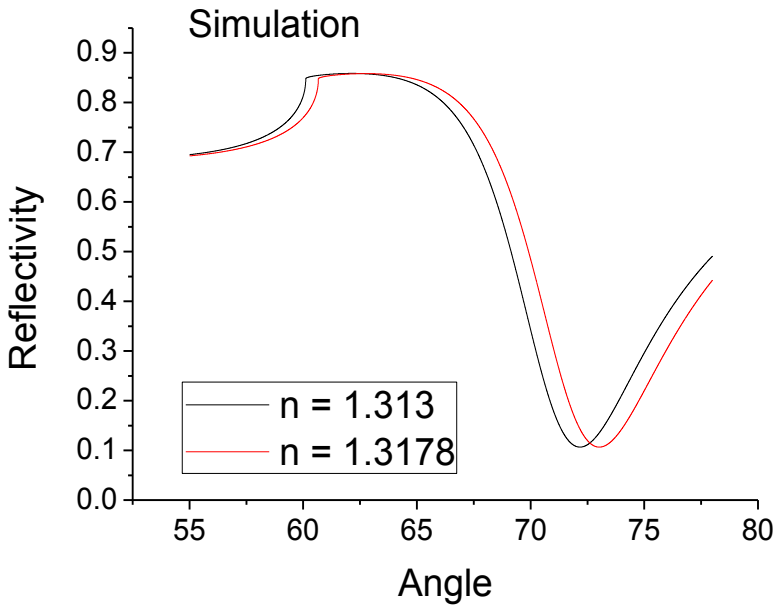

Figure 7.5. Sensitivity calibration. Simulated SPR profiles in the presence (red) and absence (black) of a full layer of 5 μm particles.

7.5 Response of positive and negative charged surfaces

To demonstrate the principle of the method, the SPR responses were measured by using negative and positive surfaces. First, channel 1 and channel 2 were modified with 10 mM 3-MPA and 10 mM cysteamine. HCl solution by operating the fluidics in the single mode to create negatively and positively charged surfaces (in 0.5 mM acetate buffer) independently. After surface modification, the fluidics was switched to serial mode, and silica particle solution was flown through the two channels sequentially for 1 min. The pump was then stopped to allow the particles to redistribute and settle down on the negatively and

positively charged surfaces in channels 1 and 2. After the SPR signals reached steady states, indicating that the particles approached equilibrium, acetate buffer was introduced to flush out remaining particles suspending in the solution. Finally the surfaces of both channels were regenerated with 10mM NaOH.

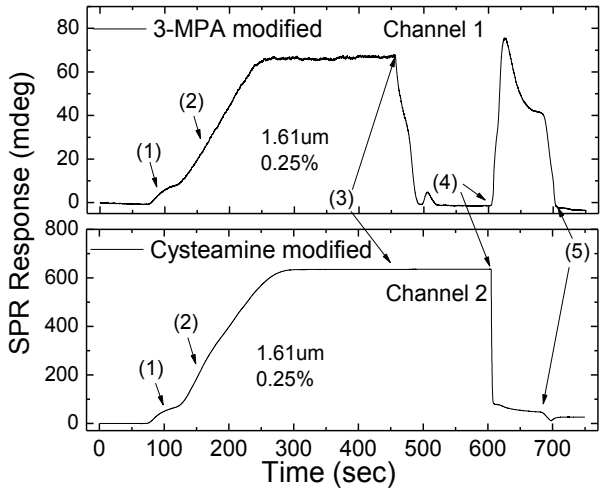

Figure 7.6. SPR response of different charged surface. SPR response of negatively charged surface (modified with 3-MPA) and positively charged surface (modified with Cysteamine.HCl) during different stages including (1) sample injection, (2) particle redistribution, (3) flushing, (4) surface regeneration, and (5) returning to baseline. 1.61 μm-diameter silica particles in 0.5mM acetate buffer with volume concentration of 0.25% were used in the experiments.

Figure 7.6 shows the SPR response of a complete experimental cycle, including injection and redistribution of the silica particles, flushing out the unsettled particles and surface regeneration. Immediately after injecting 100 μL of the silica particle solution into the cell, the SPR signals of both channels 1 and 2 increased slightly (marked by "1"). Most particles at this point were still suspended in the solution. The pump was turned off to allow the suspended

particles to settle on the surfaces, which was shown by the steady increases in the SPR responses ("2"). Within 1-2 mins., the particles reached equilibrium. For the negatively charged surface (channel 1), the corresponding steady state SPR signal is about 67 mdeg. In contrast, the SPR response reached 635 mdeg, nearly 10 folds greater, for the positively charged surface in channel 2. The large difference can be easily understood because the negatively charged particles were repelled from the negatively charged surface in channel 1, and attracted to the positive charged surface in channel 2.

The two channels also responded differently during the flushing stage ("3"), which was supposed to remove the suspended particles out of the fluidic channels with the running buffer. In channel 1, due to the repulsive force, most particles were suspended, which were completely flushed out, and the corresponding SPR signal returned to the original baseline. However, in channel 2, the SPR response did not change much. This is also expected because a complete layer of silica particles was attracted onto the surface, which could not be easily flushed out of the channel. To remove the particles from the surface in channel 2, 10 mM NaOH was introduced into the cell ("4"), which neutralized the surface and flushed the particles out of the channel. As a result, the SPR signal returned to the original baseline ("5"). The spikes in the channel 1 signal after the injection of NaOH was due to the particles released from channel 2 flushing through the channel 1. These experiments established the basic principle for the determining surface charge density using SPR. Note that the surfaces of both

channels 1 and 2 were regenerated by the 10mM NaOH injection to re-use the chip.

7.6 Particle concentration effect

The experiment discussed above demonstrated the detection of surface charges using 1.61 μm particles at 0.25%. However, as discussed in the principle section, the detection sensitivity depends on the concentration of the particles. The smaller particles have shown better sensitivity, but if the particles are too small then Brownian motion becomes important, which decreases the residence time of the particles on the surface and thus leading to smaller SPR responses. The particle concentration effect on the sensitivity has been examined by comparing the SPR responses of 1, 1.61, 2.34, and 4.74 μm-diameter particles at different particle concentrations. Figure 7.7a shows the SPR responses of 1.61 and 2.34 μm particles exposed to 3-MPA- and cysteamine.HCl-modified surfaces at 5 different particle concentrations. Following each injection of the particles into the fluidic channels, the surface was regenerated with 10 mM NaOH, which led to a spike in the SPR signal. From the SPR response curves, the SPR angular shift has been extracted as a function of concentration for particles with different sizes and surfaces with negatively (3-MPA) and positively (cysteamine.HCl) charges (Figure 7.7b).

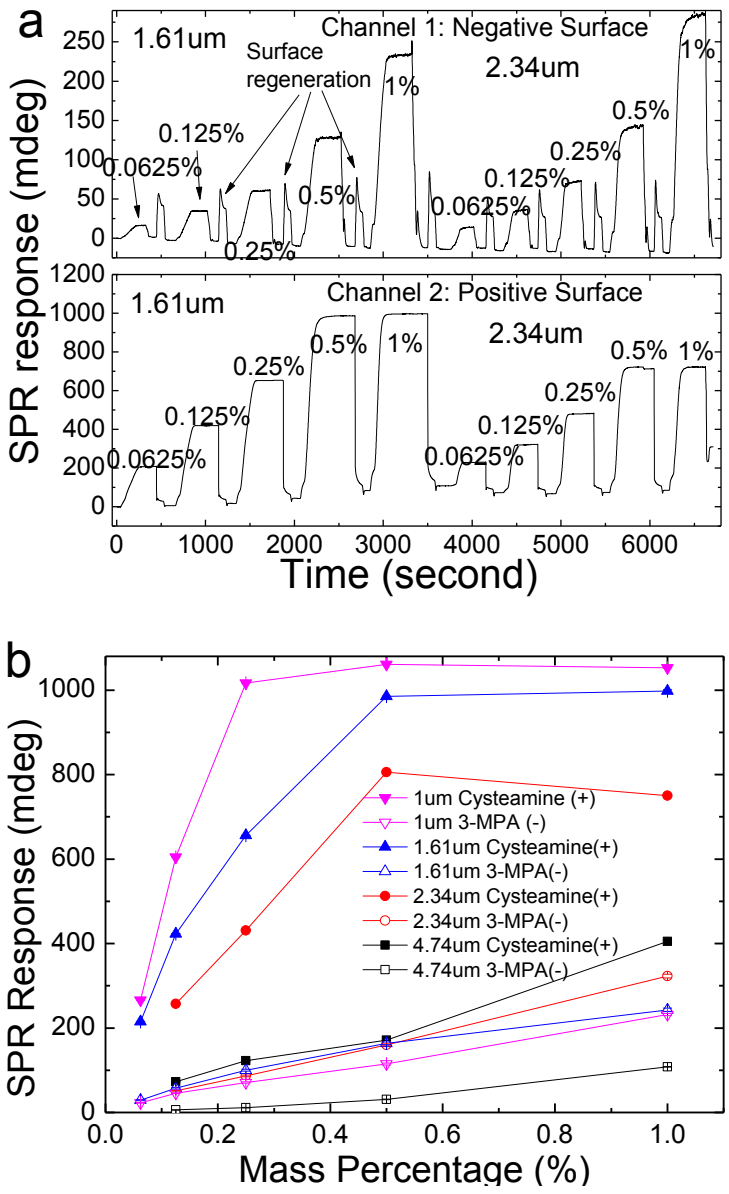

Figure 7.7. Particle concentration effect. (a) SPR response during the injection of silica particles with different concentrations and sizes for both positively and negatively charged surfaces. The small spikes in between injections are caused by surface regeneration. (b) SPR responses vs. particle concentration.

For the positively charged surface, the SPR response is proportional to the particle concentration below 0.25%, but the signal begins to saturate when the

concentration is greater than 0.5% (see Figure 7.7a). This saturation corresponds to the formation of full monolayer coverage of particles. Further increasing the particle concentration can only result in the formation of second or multiple layers of the particles on the surface, which does not contribute to the SPR response due to limited penetration length of the evanescent field created by SPR. This means that to study highly positively charged surface with negatively charged particles, one should use low concentration particles so avoid the saturation that limits the dynamic range. Based on these observations, it can be concluded that while 1.61 and 2.34 μm particles at 0.25% or 0.125% are the best for measuring the surface charge density using the SPR method.

7.7 Surface charge density of 3-MPA modified surface

The surface charge density of a 3-MPA modified surface is using as an example to demonstrate the method. For 0.25% 1.61 μm-particle, the equilibrium height is ~200 nm, according to Figure 7.2b. Using this height and Eqs. 10, the surface charge density was found to be -6 ± 0.5 mC/m^2. The measurements wree also performed by using 1.61 μm particles at 0.125% and 0.0625%, and obtained similar equilibrium heights and surface charge densities as shown in Figure 7.8a. Figure 7.8a also plots particle heights and surface charge densities for 2.34, and 4.74 μm-diameter particles at different particle concentrations. Comparing to 1.61 μm particles, the heights are somewhat smaller, and the corresponding surface charge densities of 2.34um and 4.74um particles are about -2.25 ± 0.13 mC/m^2 and -3.2 ± 0.28 mC/m^2 respectively. This discrepancy is likely due to the greater

effect of Brownian motion in the small particles, which is not included in Eq. 10. In other words, the surface charge density obtained using 1.61 μm particles overestimates the actual surface charge density.

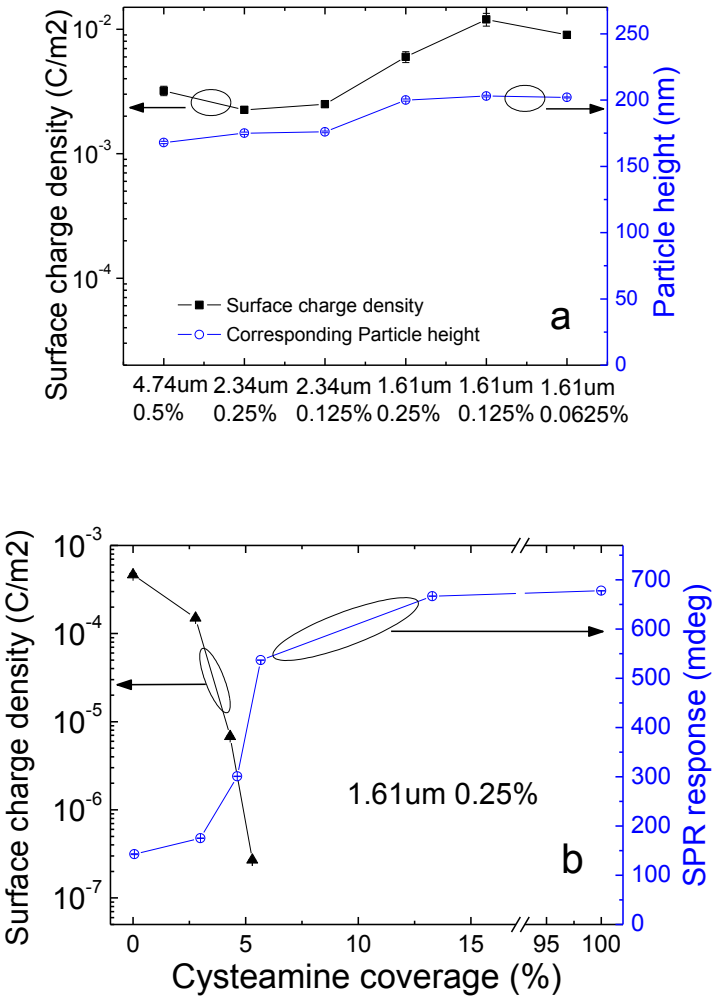

Figure 7.8. Surface charge density of different charged surface. (a) Surface charge density of 3-MPA modified surface determined by the SPR method. (b) Surface charge density (left axis) and corresponding SPR response (right axis) vs. cysteamine surface coverage.

Assume that the Au surface is fully covered with 3-MPA, which is reasonable since injecting of 3-MPA continued for 240 seconds until the SPR signal saturated, then the surface density of 3-MPA, according to the STM study reported in literature (22), is ~10^{19} m^{-2}. The pH of the acetate buffer is 5.0 and the pKa of $COOH^-$ functionalized self assembled monolayer on Au surface is 7.4.[126] Using these numbers and relation $pH = pKa + \log\frac{[A^-]}{[HA]}$ the surface charge density is -6.4 mC/m^2, which is in good agreement with the values determined using the present method. However, different methods have been applied to measure pKa of 3-MPA monolayer, and the reported values vary between 5.2 and 8.[127, 128] Since pKa is a logarithmic of the charge density, determining pKa from charge density measurement is more accurate than the titration measurements.

7.8 Surface charge density measurement at different cysteamine coverage

To further demonstrate the method, sensor surfaces were prepared with different charge densities by varying cysteamine surface coverage. This was achieved by injecting low concentration (10μM) cysteamine.HCl solution into the cell and expose it to the Au film for 4, 5, 7, 10 and 240 seconds. The corresponding surface coverage values of cysteamine as determined from the SPR angular shifts were 2.78%, 4.31%, 5.3%, 12.5% and 100%, respectively. As a reference, the surface charge density of bare Au was also measured and the Au film was found out that it was slightly negatively charged under the experimental condition (Figure 7.8b). Increasing cysteamine coverage, the negatively charged

Au surface was first neutralized by cysteamine, and turned into positively charged when cysteamine coverage reached 5.3%. Further increasing the coverage over 12.5%, the negatively charged particles were attracted to the positively charged surface and form a complete layer, which led to the saturation of the SPR signal to a fixed value.

7.9 Error analysis

The accuracy of this method depends on different factors, which is shown in Equ (1): the surface charge density is a function of SPR signal ($\Delta\theta$ affect δ through h), particle size (R), particle concentration and buffer concentration (affect through Debye length κ^{-1}). 1) The surface charge error due to noise of SPR signal is discussed in the previous section. 2) The particle size variation that came from fabrication process will affect the measurement result of surface charge density, which can be calculated from Equ (1). For example if particle's diameter varies 1% (from 4.74um to 4.787um), the surface charge density will change 1.99%. Normally the particle size has Gaussian distribution in real sample, where the most variation due to particle size will be canceled out. 3) As discussed in previous section, the particle concentration variation will affect the surface charge density results because higher concentration will give more SPR signal. Actually the concentration variation is not a problem because the concentration is calibrated by a control channel which is modified by positive charged molecule (Cysteamine). 4) Surface charge density is a function of pH. Since the solution

used here is acetate buffer which will keep the pH as constant in experiment, therefore the surface charge density will not change.

7.4.8 Zeta potential measurement

The silica particles used in this work are known to acquire negative surface charges because of the dissociation of silanol groups, given by (3), $SiOH \rightarrow SiO^- + H^+$. Since the charge density depends on pH and ionic strength of the solutions, the zeta potentials of the sample silica particles in solutions with different pH and ionic strengths were measured using electrophoretic light scattering technique. To prepare solutions with different pH values, HCl and NaOH solutions with appropriate amounts were mixed. As shown in Figure 7.9a, the zeta potential of 1.61 μm silica particle decreases with pH due to protonation of the silanol group. The figure also shows a large pH window within which the particles are negatively charged. Since our surface charge density measurements used the low concentration acetate buffer, zeta potential of the particles is also measured in acetate buffers (Figure 7.9b). The zeta potential increases with acetate concentration, due to the decrease of pH (from 5.21 of 0.1mM to 4.88 of 37mM).

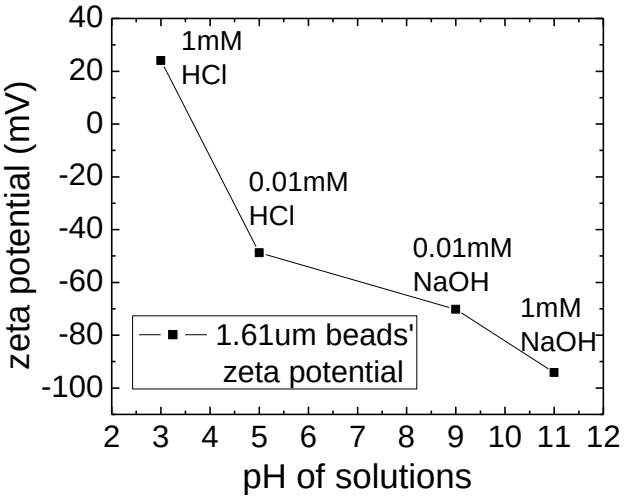

(a)

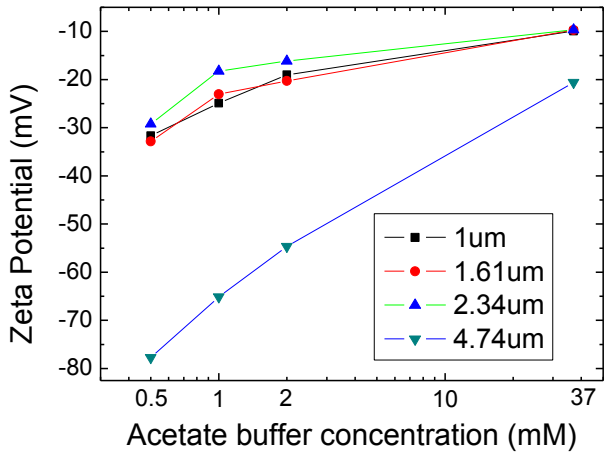

(b)

Figure 7.9. Zeta potential of 1.61 μm silica particles vs. pH. (b) Zeta potentials of silica particles with different sizes vs. acetate buffer concentration.

7.10 Conclusion

SPR response is extremely sensitive to the vertical position of an objective over a SPR sensor surface. This unique feature can be used to accurately measure the equilibrium height of a particle over the surface. If the particle and surface are charged, then the equilibrium height is determined by the balance between gravity

and electrostatic force on the particle. Both numerical simulations and experiments carried out in this work show a simple relation between the surface charge density and SPR response, which leads to a sensitive method to determine surface charge density. The sensitivity of the method depends on the particle size and concentration. Smaller particles are, in general, more sensitive than larger particles. However, if the particles are smaller than ~1 μm, then Brownian motion becomes important, which changes the relatively simple relation between SPR response and surface charge density. Higher particle concentrations are also more sensitive, but the upper limit is determined by the full coverage of the surface with particles. The particles demonstrated in this work were negatively charged silica particles, which acted probes and amplifiers for sensitive detection of surface charge density. Other micro- and nano-objects, insulating, semiconducting or metallic, may also be used as probes, as long as their optical properties are different from that of the buffer solution. Finally, this method can, in principle, determine the charge of micro- and nano-scale objects if the surface charge of the sensor is known or calibrated which will be shown in Chapter 8.

CHAPTER 8

STUDY OF SINGLE PARTICLE CHARGE AND BROWNIAN MOTHIONS WITH SURFACE PLASMON RESONANCE

8.1 Introduction

Particulate matter is a unique form of materials that exists everywhere in nature. It includes inorganic and organic particles, but also biological substances, such as cells, bacteria and viruses, with size ranging from a few tens of nm to a few tens of microns. Understanding particulate matter is critically important for environmental, colloidal and life sciences, and directly relevant to many chemical engineering processes. Surface charge density of a small particle is a basic quantity that determines the interactions of the particle with a surface and with other particles.[129, 130] The most widely used method to measure surface charge density of a particle is electrophoresis, which measures the average drift velocity of many charged particles under the influence of a static electric field.[130-132] While popular, the method is difficult to follow and measure the individual particles that often have different surface charges. A capability of measuring the surface charge of a single particle in solution is important because of the inhomogeneity of particles in most practical settings.

In last chapter, the SPR is used to measure the silica particle's height, and by using this height information, the surface charge density has been measrued. The silica particle is used as a probe or tool to explore the surface property and

the particle height is an equilibrium height after stabilization. If SPR imaging technique is used, the local surface charge density can be measured.

In this chapter, a method which can accurately measure the surface charge of individual small particles is developed with SPR. SPR is a surface sensitive technique that has been widely used to study molecular binding processes onto a surface. Recently the principle of SPR has been used to measure surface charge density[133] and to map local surface impedance[43] and electrochemical current.[134] The basic principle of our single particle surface charge measurement relies on the sensitive dependence of surface plasmon waves propagating along a metal surface on a small particle near the surface. Chapter 7 shows that the SPR signal provides an accurate measurement of the vertical position of the particle, which can be used to study the Brownian motion of the particle. By applying an AC potential to the metal surface, an oscillating electric field that drives the particle to move up and down near the metal surface is created, which is measured with SPR, allowing for accurate determination of the surface charge of the particle. In order to simultaneously measure many particles, an microscope-based SPR[44] imaging setup that can image particles as small as a few tens of nm was used.[135]

8.2 Experiment setup

Figure 8.1a shows a schematic diagram of the experimental setup. The SPR microscope (SPRM) was constructed based on an inverted microscope (Olympus IX81), using a high numerical aperture oil immersed objective (N.A.

1.49) to achieve high incident angle for surface plasmon excitation[44]. A polarizer was inserted into the optical path to produce p-polarized light to excite surface plasmons in a 47 nm thick Au film thermally evaporated on a glass slide in high vacuum ($3x10^{-6}$ Torr). A Teflon solution cell was placed on the Au film. The electrical potential of the Au film was controlled and modulated with a potentiostat (Pine Instruments) using the standard 3-electrode electrochemical configuration (with Ag and Pt wires as quasi-reference and counter electrodes, respectively). Silica particles (Bangs Laboratories, Inc.) of different sizes (4.74 μm, 2.34 μm, 1.61 μm) were rinsed with DI water 5 times and then dissolved in 0.5mM NaF solution before each experiment. A CCD camera (Pike F-032B from Allied Vision Technologies, Newburyport, MA) was used to record the SPRM image with a frame rate varying from 100 fps to 378 fps. A LabView program and a National Instrument data acquisition card was used to record the current and trigger signal of the CCD camera for signal synchronization.

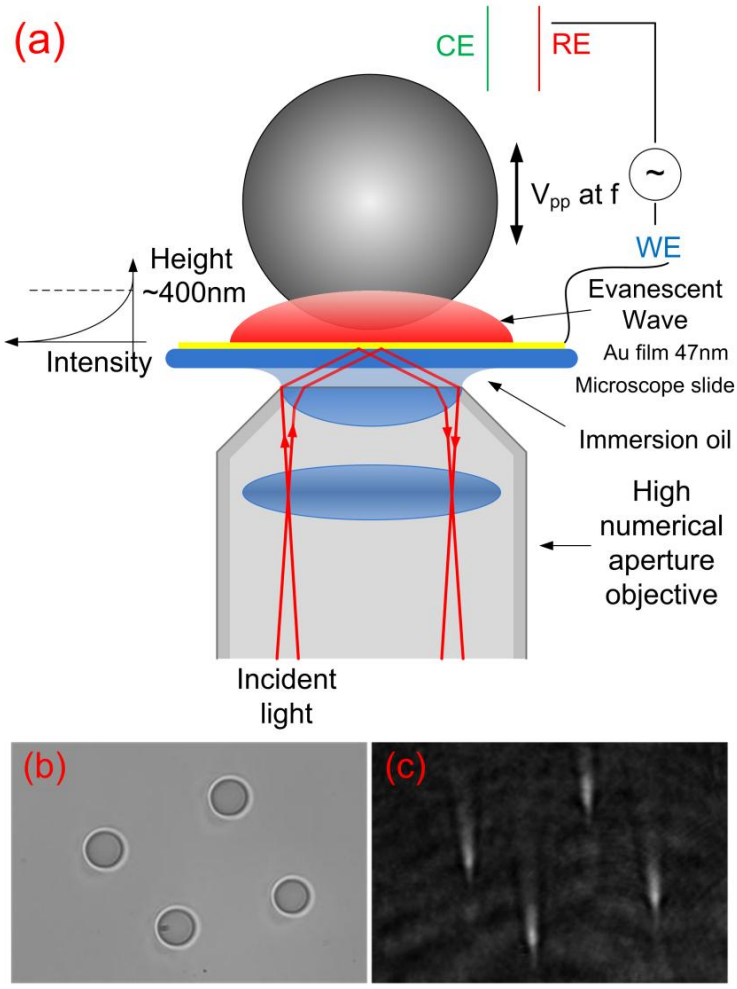

Figure 8.1. Principle of the method and SPR image of floating particles. (a) Schematic diagram of experimental setup. (b) Transmitted image of small particles near a gold surface. (c) Simultaneously recorded SPR image of the small particles. Particle size is 4.74μm and solution is 0.5mM NaF.

In each experiment, 600 μL of 0.5mM NaF solution containing 0.05% (by mass) silica particles was introduced into the solution cell. The particles moved towards the Au film under the influence of gravity, but eventually counter balanced by the electrostatic repulsion between the negatively charged particles and negatively charged Au film, and the equilibrium height of the particles is

determined by the surface charges of the particles and Au surface, and size and mass density of the particles.[133] Figures 8.1b and 1c show the transmitted and SPRM images of 4.74μm silica particles in 0.5mM NaF solution. Each particle in the SPRM image is a bright spot with a very long tail along the propagation direction of the surface plasmon waves. The bright spot is smaller than the actual size of the particle because the evanescent wave associated with surface plasmon waves penetrates into the solution over a distance of about 200 nm, much smaller than the size of the particles, so that only the bottom portion of each particle is imaged by SPRM. The long tail is due to the scattering of the surface plasmon waves by the particle.[135]

8.3 The principle and experiment results

The SPRM image contrast arises from the perturbation of the evanescent wave by the particle. Because the evanescent wave decays rapidly from the Au surface, the image contrast provides a sensitive measurement of the particle height, which is used to determine the surface charge density of small particles with the following procedures. An AC potential modulation was applied to the Au film, and recorded the responses of the particles to the modulation electric field with the SPRM. Figure 8.2a is snapshot of the SPRM video showing individual silica particles (0.05% 4.74μm bare silica particles in 0.5mM NaF, 1 V peak-to-peak, at 20 Hz). Figure 8.2b shows the SPRM responses of a particle and adjacent bare Au region (marked by rectangles in Figure 8.2a). The SPRM intensity of the particle exhibits a large periodic oscillation, due to the change in the particle height as the

charged particle is driven towards and away from the Au surface by the AC electric field (Figure 8.2b). The SPRM intensity of the bare Au region shows a small but measurable periodic response, which is due to the dependence of SPR on surface charge density of the Au film.[43] This effect has been used to determine surface impedance.[43]

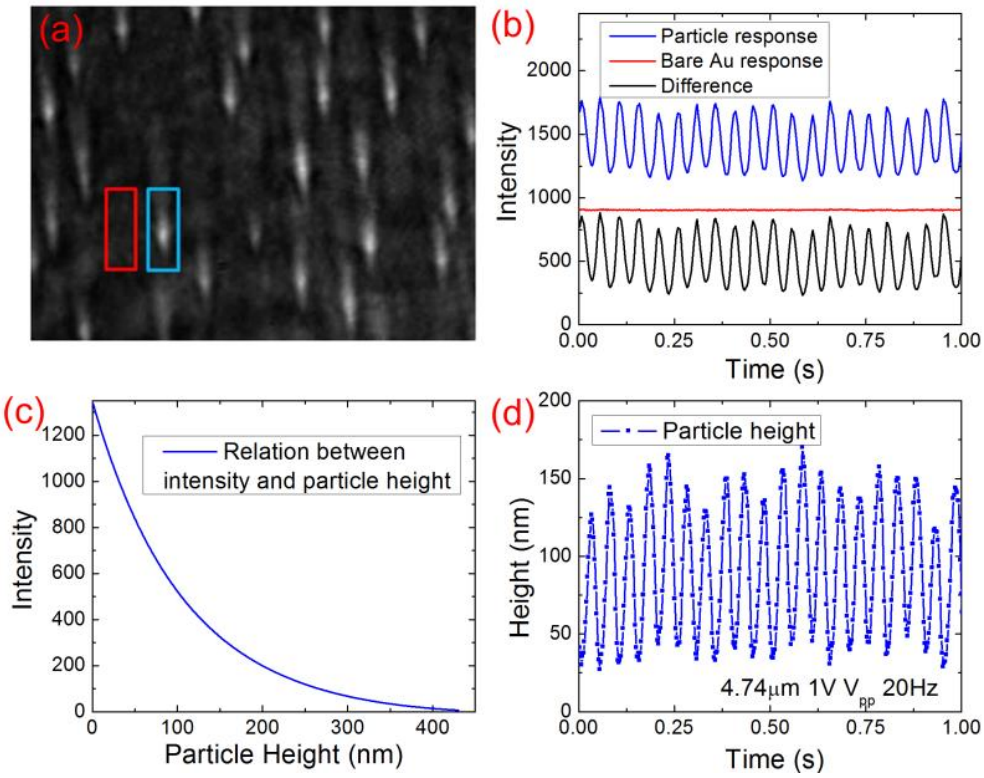

Figure 8.2. Converting SPR signals to particle height. (a) SPR image of 4.74μm particles. Two regions of interest, one containing a particle and one showing background bare Au are marked with a blue and red rectangles, respectively. (b) SPR response (intensity) of the two regions shown in (a). (c) Relationship between the SPR intensity of a particle and particle height. (d) Particle height oscillation.

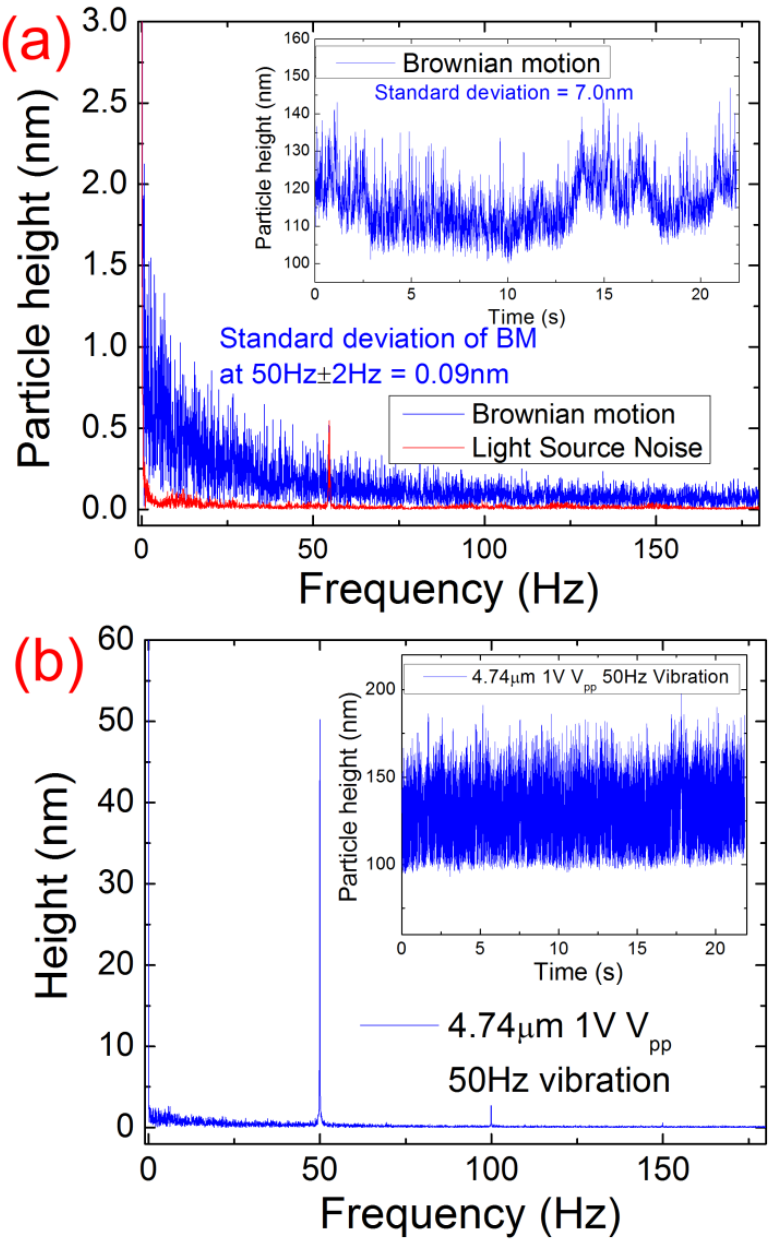

Figure 8.3. FFT of particle height. (a) Fourier Transforms of particle height variation of a 4.74 μm particle due to Brownian motion (blue curve). For comparison, the light source noise is also shown (red curve). Inset: Height variations due to Brownian motion in time domain. (b) Fourier transform of the particle driven into oscillation with an applied potential (1V V_{pp} and 50Hz),

where the sharp peak at 50 Hz is due to the particle height oscillation. The inset of the figure shows the particle height oscillation in time domain.

The relationship between SPRM intensity and particle height can be determined numerically and calibrated experimentally.[133] As shown in Figure 8.2c, the SPRM intensity decays exponentially with the particle height with a decay constant of ~200 nm, providing sensitive measurement of particle height. For example, for a particle located 50 nm away from the Au surface, a change of the particle height by 1 nm leads to 0.58 % intensity change, which can be accurately measured. Using the relationship between SPRM intensity and particle height, the oscillating SPRM intensity shown in Figure 8.2b was transformed into particle height oscillation (Figure 8.2d).

Note that although the oscillating amplitude of the particle height shown in Figure 8.2d is uniform, the equilibrium height, due to the Brownian motion, fluctuates. The inset of Figure 8.3a shows more clearly the random particle height fluctuations due to the Brownian motion. The standard deviation of the particle height due to the Brownian motion is about 7 nm. Although the Brownian motion deserves further study on its own right and the SPRM provides a new tool to facilitate the study, it is an important source of noise in the measurement of surface charge density of small particles. For example, for a particle with equilibrium height of 116 nm (inset of Figure 8.3a), the signal-to-noise ratio is limited to ~17 by the Brownian motion. However, the noise spectrum of the Brownian motion decreases with frequency, so one can reduce the Brownian motion noise by modulating the potential at high frequencies. Figure 8.3a shows

the Fast Fourier Transform (FFT) of the Brownian motion of a 4.74 μm particle. At 50 Hz, the standard deviation of the Brownian motion is only 0.09 nm. Note that the noise spectrum of the light source is also shown in Figure 8.3a, which is much smaller than the Brownian motion noise.

The above noise analysis indicates that AC modulation at high frequencies can significantly reduce the dominant source of noise from the Brownian motion, which will provide a more accurate measurement of particle surface charge density than simple DC measurements. The inset of Figure 8.3b shows the height response of a 4.74 μm to a 50 Hz AC potential modulation (1V peak-to-peak sine wave). The FFT of the height response (Figure 8.3b) shows a sharp peak at 50Hz, due to the height response to the AC potential modulation. The signal-to-noise ratio is as high as 558, which means the height variation can be determined below 0.1 nm. Note that a small peak appeared near 100 Hz, which is due to nonlinear response of the particle height to the applied AC electric field.

Since the Debye length of the 0.5mM solution is very small (~20 nm) compared to particle sizes studied here, the electrophoretic force due to the electric field within the electric double layer can be ignored. Another important consideration is that the solution impedance (~17.2 kΩ) is much larger than the interfacial impedance (~135Ω) due to the double layer charging effect, so most of the applied voltage drop occurs in the solution rather than at the solid-liquid interface. The particle motion caused by the electric field within the solution is focused, which allows me to express the particle velocity in terms of electric field by,[131, 132, 136]

$$v(t) = \frac{\varepsilon_r \varepsilon_0 \xi_{EP} E(t)}{\eta} = \frac{\varepsilon_r \varepsilon_0 \xi_{EP}}{\eta} E_0 \sin(\omega t) \quad (1)$$

where μ, η, ε_r, ε_0, ξ_{EP} , ω, E(t) and E_0 are mobility of particle, dynamic viscosity of solution, dielectric constant of solution, permittivity of free space, zeta potential of particle (due to electrophoresis), angular frequency of the applied electric field, electric field (function of time) and maximum electric field respectively. Because the particle moves vertically only, there is no electroosmotic flow appear, which greatly simplifies the analysis.

The maximum amplitude of oscillation height is given by,

$$D_{AMP} = -\frac{2\varepsilon_r \varepsilon_0 \xi_{EP} E_0}{\eta \omega} = -\frac{\varepsilon_r \varepsilon_0 \xi_{EP} E_0}{\pi \eta f} \quad (2)$$

where f is modulation frequency. The zeta potential of particle can be calculated from,

$$\xi_{EP} = -\frac{\pi \eta f D_{AMP}}{\varepsilon_r \varepsilon_0 E_0} = -4.3825 \times 10^6 \times \frac{f D_{AMP}}{E_0} \quad (3)$$

where E_0 is the maximum electric field amplitude and can be calculated from $E_0 = \frac{i_{max}}{\sigma}$, where i_{max} is the maximum current density and σ is conductivity of solution. Zeta potential of a particle can be easily calculated from Eq. 3. For example, at 50-Hz and 1-V V_{pp}, the particle shown in Figure 8.3b has oscillation amplitude 52.3nm at E_0 = 112.9 V/m. The zeta potential calculated from Eq. 3 is -101.6 mV, which is in excellent agreement with the average zeta potential, -107.2 mV, measured by Zetasizer Nano from Malvern Inc. Knowing the zeta potential, the surface charge of the particle can be calculated with the Smoluchowski

equation.[137] The surface charge of the particle shown in Figure 8.3b is -4.1 x 10^{-13} C.

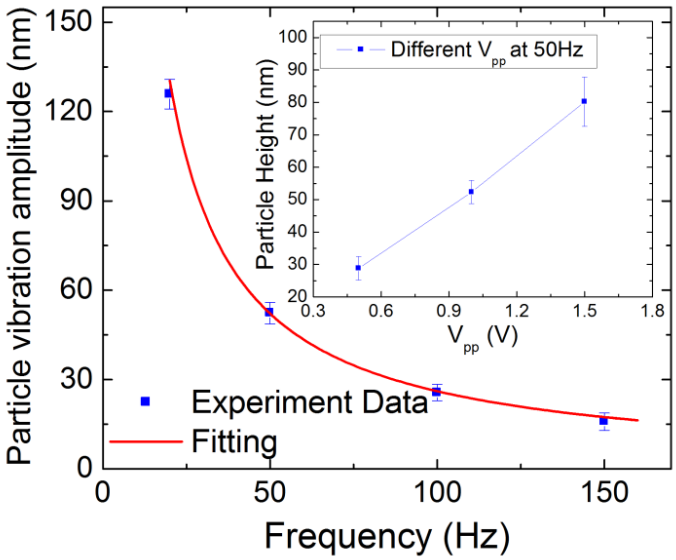

Figure 8.4. Particle vibration amplitude vs frequency. Dependence of the particle height oscillation amplitude with frequency measured experimentally (blue squares) and predicted by the theory (red solid line). Inset: Dependence of particle height oscillation amplitude vs. the amplitude of the applied potential (V_{pp}).

To further confirm the theory described above, the oscillation amplitude of the particle height was measured as a function of frequency and amplitude of the applied potential. As shown in Figure 8.4, the measured amplitude dependence on frequency (blue squares in Figure 8.4) is in good agreement with Eq. 2 (red line). The oscillation amplitude as a function of the applied potential (V_{pp}, inset of Figure 8.4) is also plotted, which shows a linear dependence of the amplitude on the applied potential, also in agreement with the theory.

8.4 Conclusion

In conclusion, a method to measure the zeta potentials and surface charges of individual particles is demonstrated by SPRM. In the method, charged particles near a metal surface are driven into oscillation by apply an AC voltage to the surface, and oscillation amplitudes are accurately determined from the SPRM images. The AC method reduces noises due to the Brownian motion, leading to accurately measurement of the particles. Because many particles can be simultaneously measured with the SPRM, the method could be used for high throughput analysis of particles.

CHAPTER 9

A LABEL-FREE OPTICAL DETECTION METHOD FOR BIOSENSOR AND MICROFLUIDICS

9.1 Introduction

The use of microfluidic or lab-on-a-chip system has shown great promise for many applications, including biomedical research [138], clinical analysis [139] and chemical analysis [140]. A key requirement for any kind of microfluidic systems is a detection method that can quickly and sensitively monitor analytes in the microfluidic channels. Often, indicators, also known as labels, are attached to a sample analyte before experiment to report the presence and movement of the analyte [141]. Although label-based detection methods have played an important role in the development of microfluidic devices, they typically require extra sample preparation steps, and the attachment of the labels may alter the native biological functions of the sample molecules [141]. For these reasons, a label-free method is highly desired for microfluidics and biosensor applications. SPR has emerged as a powerful label-free analysis technique [9, 142]. However, SPR can only detect molecules on or near a surface (within ~200 nm) [143], which is not suitable for typical microfluidic applications that have channel heights much greater than ~200 nm. Another key improvement one wishes to make is the sensitivity of SPR detection, which is necessary for the detection and analysis of low abundance analytes.

In this chapter, a label-free detection method that can overcome the drawbacks of conventional SPR mentioned above is demonstrated. The method allows to generate a series of optical/plasmon modes in a microfluidic channel, including a mode similar to SPR and bulk optical modes that are fundamentally different from SPR. The SPR mode is surface sensitive while the bulk modes are sensitive to entire channel and can detect analytes in the channel 20 times more sensitive than the conventional SPR. The method can be operated either in the SPR mode for studying molecular binding on surfaces or in the bulk optical modes for monitoring analytes in a microfluidic channel.

9.2 Principle and Experiment setup

The principle and experimental setup of the method is illustrated in Figure 9.1(a). The setup consists of two major components, a microfluidic chip and an optical excitation/detection system. The microfluidic chip is formed by binding a bottom substrate and a channel forming top piece. The substrate is a BK7 glass slide covered with 40 nm gold. The top piece, also made of glass, has a microfluidic channel etched on one face which is coated with 100 nm gold. A syringe pump moves sample solution in and out of the channel. The microfluidic piece is placed on a BK7 prism covered with a drop of index matching fluid. A p-polarized beam from a collimated laser diode (670 nm) is incident onto the prism surface and the reflected beam is detected with a CCD camera. Depending on the incident angle, SPR and a series of other optical modes can be generated in the microfluidic channels. As a result, the measured reflectivity vs. incident angle

displays multiple dips (Figure 9.1(b)). The dips shift in angular positions when an analyte, with a refractive index different from the background buffer solution, is present in the channel or binds on the surfaces of the channel, which provides label-free detection of molecules.

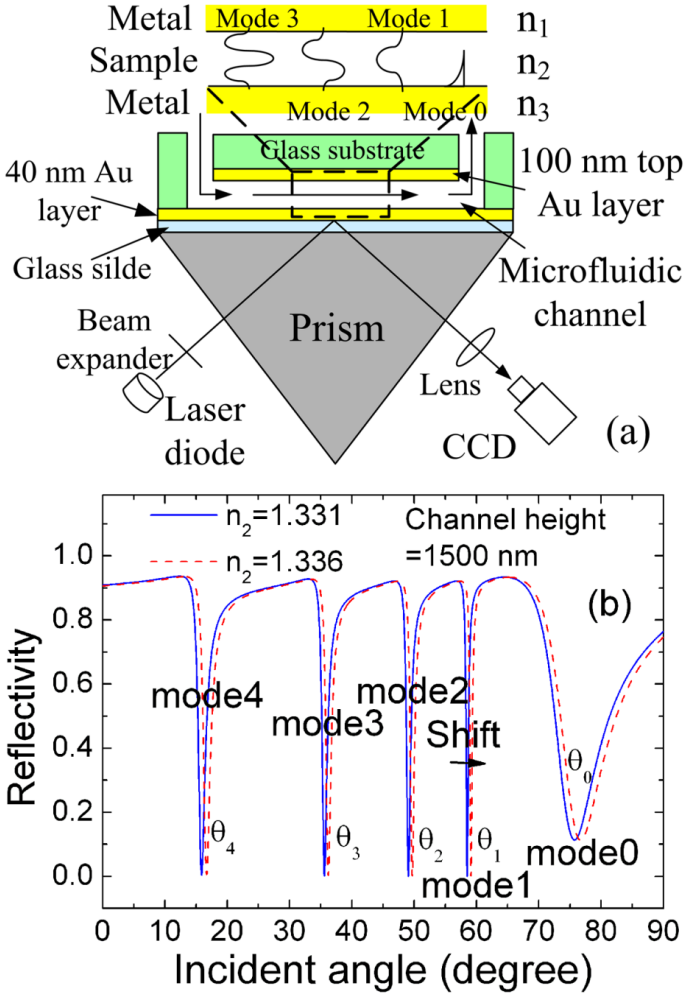

Figure 9.1. Principle scheme and simulated scan angle response. (a) Device structure and experimental setup of the method. (b) Reflectivity vs. incident angle at two different refractive indices. The channel height is 1500 nm.

In order to understand the optical modes, the reflectivity vs. incident angle (Figure 9.1(b)) is calculated by using a stratified medium model[123]. When the

incident angle is greater than a critical angle, total internal reflection occurs and the evanescent wave excites SPR in the gold film, which results in a dip near 76°. The resonance angle is the same as that of the conventional SPR mode created without the Au-coated top surface. This observation and further evidence presented later indicate the mode is similar to the conventional SPR and will be referred to as the SPR mode. As the incident angle is decreased below the critical angle, light couples into the microfluidic channel by bottom Au thin film at some specific angles. This phenomenon appears only when the incident angles satisfy the phase requirement of eigenvalue equation for waveguide modes[2] and generates bulk optic modes. At these bulk modes the light will couple into the microfluidic channel rather than reflect back, resulting in dips in the reflectivity at different angles (θ_1, θ_2, θ_3 …)(Figure 9.1(b)). It is important to note that these modes give rise to dips much sharper than the SPR dip. At a fixed channel height and wavelength, the resonance angles (θ_0, θ_1, θ_2, θ_3…) shift with the change of refractive index inside the channel. By measuring reflectivity at a fixed incident angle near a sharp resonance dip, the angular shift due to the change in the refractive index can be determined, providing a sensitive detection and analysis of analytes in the microfluidic channel.

9.3 Function of top Au layer

The top Au layer is the critical layer in the method. Figure 9.2(a) compares it to the conventional SPR and microfluidic channel without a top Au layer. In the conventional SPR, surface plasma is excited near the bottom metal

surface giving rise to a broad dip near 76 °. The dip overlaps with the SPR mode created with the Au top, strongly suggesting a common origin for the conventional SPR and the SPR mode observed in the present method. If the top layer is not covered with Au, i.e., a transparent top, bulk optical modes can be created only if $n_1<n_2$ and $n_3<n_2$, where n_1, n_2 and n_3 are the refractive indices of the top material, solution in the channel and bottom substrate, respectively.[9] Since solution in the channel is almost always an aqueous solution with refractive index, ~ 1.3316 at 670nm, it is difficult to find a suitable top material to satisfy the second condition, $n_3<n_2$. If only the first condition is satisfied, then most light leaks through the top and the bulk optical modes are poorly defined (red line in Figure9.2(a)). The top Au layer serves, thus, as a "mirror" to reflect light back into the channel and lead to the bulk optical modes well defined at θ_1, θ_2, θ_3....

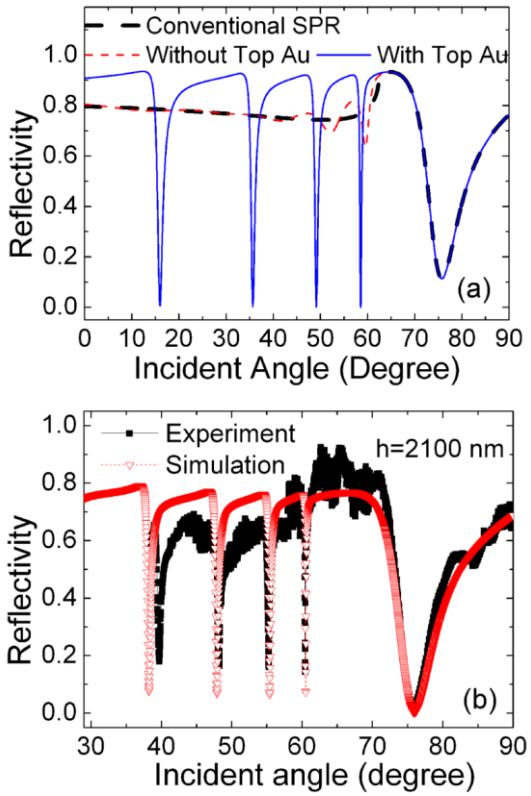

Figure 9.2. Experiment vs simulation results of angle scan. (a) Comparison of the conventional SPR (dashed black line) and present detection method (blue). To illustrate the importance of the top gold layer, the reflectivity of a channel with bare glass (no gold layer) is also shown (dashed red line). The channel height is 1500 nm, bottom Au thickness is 40 nm, and top Au layer is 100 nm. (b) Measured and calculated resonance curves of the bulk optical modes.

The microfluidic channels described above has been fabricated and the reflectivity as a function of incident angle is measured by mechanically scanning the incident angle. Each channel is 50 μm wide and 2100 nm high, which is filled with deionized water (18 MΩ·cm) by a syringe pump. The measured reflectivity indeed shows multiple well-defined dips due to both the SPR and the bulk optical modes. The mode measured near 40 ° is at a slightly smaller angle than the calculated one, which is due to image shift caused by the angle scanning process in our setup. Overall, both the shapes and positions of the dips are in excellent agreement with the calculation (Figure9.2(b)).

9.4 Bulk-sensitive

As mentioned before, the electric field of the SPR mode penetrates into the fluid channel over a distance of ~200 nm,[7] which is small comparing to the channel height (e.g. 2100 nm). This is the reason that the conventional SPR is sensitive to surface binding processes but not suitable for detection of sample molecules filled over the entire channel. Our detection method can be operated in either the SPR mode or in one of the bulk optical modes. When operated in the

SPR mode, this method retains the surface sensitive feature of the conventional SPR. On the other hand, by tuning the angle to one of the bulk optical modes, this method can detect molecules in the bulk of the microfluidic channel. Next, the bulk-sensitivity of the optical modes has been demonstrated in two ways.

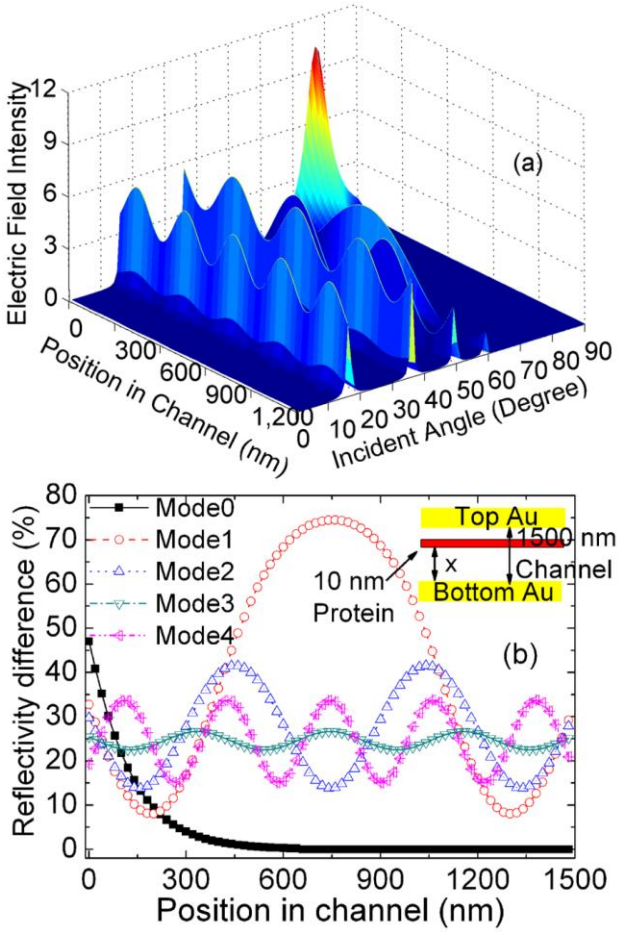

Figure 9.3. Electric field distribution within the channel. (a) Electric field distribution inside a microfluidic channel, where x-axis is position in the vertical direction of the channel which has a height of 1500 nm, y-axis is incident angle of light and z-axis is electric field intensity of TM field. (b) The response of each mode to a probe slab with index of refraction 1.57 and thickness 10 nm located at different heights in the channel.

First, the electric field distributions of the bulk optical modes has been calculated (Figure9.3 (a)). Note that electric field intensity is TM field normalized by incident field intensity ($<E_{tm}>^2/<E_{in}>^2$). Five peaks can be found at different angles, and number of modes and angular positions of each mode matches reflectivity simulation shown in Figure9.1(b). The electric field of the SPR mode is strongest at the surface and decays exponentially into the channel, showing once again its similarity to the conventional SPR mode. The bulk optical modes have electric field largely distributed inside the channel which means they are more sensitive to the bulk than the surface. Second, the response of each mode by placing a 10-nm "protein" layer (n=1.57 [144]) at different distances from the bottom surface is simulated. The presence of the "protein" layer changes the resonance angle of each mode which is detected by measuring the reflectivity fixed near the resonance angle of each mode (Figure 9.3(b)). For the conventional SPR mode, the response is largest when the "protein" layer is located on the surface and decreases exponentially as the "protein" layer moves away from the surface. In contrast, the response of the bulk optical modes display one or multiple broad peaks at the center of the channel, showing that it is most sensitive to molecules inside the channel.

9.5 Sensitivity

Comparing to the conventional SPR, the bulk optical modes have much sharper dips and thus much higher sensitivity. The sensitivity was quantified by using the change in reflectivity, ΔR, caused by relative change in the refractive

index of the solution in the channel ($\Delta n/n$), or $\Delta R/(\Delta n/n)$. The sensitivity is determined by injecting ethanol solutions of various concentrations into the microfluidic channel and measured the reflectivity changes for both the SPR and the 1st bulk optical mode. The ethanol solutions served as a calibration standard since their refractive indices are well known. Figure 9.4(a) shows the reflectivity changes of the SPR mode and mode 1 in response to the injection of 0.01%, 0.05%, 0.1%, 0.2%, 0.5%, and 1%, respectively. As expected the reflectivity change is a linear function of ethanol concentration (Figure 9.4(b)), and the slope provides the sensitivity. The measured sensitivity of the SPR mode is about 29.7 while it is ~587 for mode 1, more than 20 times larger. The sensitivities of the two modes has been calculated, and they are 40.1 and 1027 for the SPR mode and mode 1, respectively. Given the unavoidable errors in the actual channel height and Au film thickness and collimation of the incident light, the agreement between theory and experiment is good.

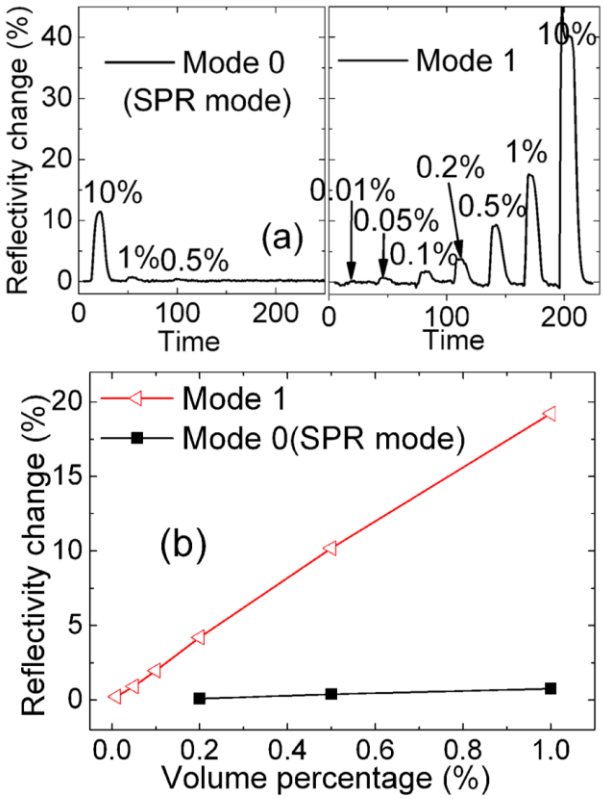

Figure 9.4. Sensitivity measurement and comparison with SPR. (a) Reflectivity response to the injection of ethanol solutions of various concentrations for the SPR mode (mode 0) and mode 1. (b) Reflectivity vs. ethanol concentration for the two modes.

9.6 Conclusion

In conclusion, a label-free optical detection method has been demonstrated for biosensors and microfluidics. It can be operated either in the SPR mode, or in one of the bulk optical modes. The SPR mode is suitable for detecting surface binding events. In contrast, the bulk optical modes are extremely sensitive to the presence of molecules in the bulk of a microfluidic channel, which is particularly attractive for microfluidics devices. The detection principle has been modeled

numerically, fabricated microfluidics devices, and built the optical detection system to confirm the simulation experimentally.

CHAPTER 10

CONCLUSIONS AND PERSPECTIVE

10.1 Conclusions

10.1.1 EC information microscope: PECI technique

Microscope has been developed for more than 400 years, and the invention of STM, AFM and TEM expands the microscope and covers the range from angstrom to millimeter. The goal of the most of microscopic methods is to measure the optical properties or morphology of the sample which does not provide the electrochemical information of the surface.

SECM is a method which can obtain local EC properties of the surface. Microelectrode is used to scan through the surface and current is recorded at same time, therefore the current is measured at each location/pixel individually. This process means if a CV current image of whole surface at 480×640 resolution is measured by SECM, about 300,000 local EC reactions or experiments is needed. Although this can be controlled by computer and software, the whole process is still very slow and low efficiency. Obviously the distance between microelectrode and substrate will affect the measurement result, therefore the complicated control system is needed for SECM. The scanning microelectrode will perturb the reaction because the distance between electrode and substrate is within diffusion length of reaction. The scalability of SECM is not good because the signal (current for here) measured by SECM will scale down with smaller electrode. What SECM measured is current rather than current density.

The fundamental reason that SECM have to face many challenges is because the signal that SECM measured is current. All the electrons transfer or exchange on entire electrode surface will converge to one current and this current is been measured by conventional method. Thus, intrinsically conventional current measurement method does not have spatial capability. To obtain spatial information, a scanning electrode has to be used and this will cause many troubles.

In this thesis, a new principle was proposed to measure the current: instead measuring current by measuring current, the new method measures current by the optical signal which is accompanied with current (EC process). The reason why this principle works is because when EC reaction happens, it is always accompanied with electron transfer and species change (from oxidant to reductant). The reaction products will change the optical signal which for here is refractive index. Therefore, when EC reaction happens, an electric signal is always accompanied with optical signal and they have a fixed relation.

PECI is based on the principle that using optical signal to measure the current, and the process and equation that transfer the optical signal to current is derived. Since the optical method intrinsically has spatial capability, the whole surface's current density can be imaged or seen at one time and current image speed is decided by speed of camera and can be as fast as 100,000 frames per second. PECI method only needs to capture images from the surface, therefore this method is non-invasive and the EC reaction will not be disturbed.

Most important advantage is that PECI method's signal will not decrease when area decreases. It is because what PECI method measured is optical

intensity which is proportional with current density that will not decrease with area. In theory, PECI method will have unlimited scalability, while in reality smaller area will have bigger noise compare with signal which will eventually kill the signal.

In this thesis, several applications have been developed based on PECI method. Trace particles embedded in fingerprint can be detected by PECI while they cannot be distinguished from conventional EC method (Chapter 3). EC reaction and impedance property of graphene has been measured with PECI method and single or double layer graphene's thickness is characterized by SPR (Chpater 4). Spatial capability of PECI method is expanded to square wave voltammetry (SWV) (Chapter 5). PECI is used to image catalytic current of platinum nanoparticle microarray and shows ability for nanoparticle screening and detection (Chapter 6).

10.1.2 A method to measure surface charge density of surface and particle

How to measure charge density of a surface or a particle in the solution is another big challenge. To solve this problem, a method based on SPR is developed in this thesis. The fact that SPR is extremely sensitive to the refractive index change near the surface, therefore it is used to accurately measure the particle height which is floating near the sensing surface due to the equilibrant between gravity and electrostatic repulsion. By measuring the height of the particle, the local surface charge density can be calculated (Chapter 7).

Surface charge density of a particle is measured by the similar principle. A floating particle near the surface was driven by a periodic potential. The height of

the particle is measured by SPR and the FFT results show the amplitude of vibration. At given potential, the vibration amplitude of particle is proportional to the surface charge density of the particle, therefore the particle's surface charge density can be calculated (Chapter 8).

10.1.3 Bulk sensitive detection method

SPR is a great surface sensitive method which can measure the binding happens on the surface. However, some of the applications not only need surface sensitivity, but also bulk sensitivity. For example, microfluidic detection and cell based assay both need bulk sensitivity. To solve this problem, a method which is sensitive to the bulk refractive index change of whole channel (between two surfaces) is developed in Chapter 9. The light shines to top and bottom surface of the channel and the reflected light of two surfaces has interfered with each other. By measuring the interference pattern, the refractive index change in the channel will be detected. The sensitivity of this method is 20 times more than SPR since it detect the whole volume change of the channel.

10.2 Perspective

As demonstrated in this thesis, PECI technique is very useful and can be applied to different applications. In principle, as long as local EC information is needed, PECI technique can be applied to it. Thus, there are huge room it can expand to, for example DNA and protein array detection and cell based detection. More specific, in Chapter 6 PECI has been applied to measure the catalytic reaction current of PtNP, this can be pushed down more to see whether the single

nanoparticle's EC reaction can be measured and imaged by PECI technique which is very useful important.

One of the challenges of PECI method is how to increase the signal. The optical signal (refractive index) change of some of the reaction is not very big because the molecule may only lose or get an electron and it will not change the optical properties of the molecule a lot. If the reaction increases or decreases the proton concentration of the solution, pH indicator could be added into the reaction which will help to improve the signal since pH indicator has big RI change due to the absorption of light.

I believe more and more real applications in EC microscope will begin by applying and improving PECI technique described in this thesis.

REFERENCES

[1] H.Raether, "Surface plasma oscillations and their applications," *Phys. Thin Films,* vol. 9, pp. 145-261, 1977.

[2] W. Knoll, "Interfaces and thin films as seen by bound electromagnetic waves," *Annual Review of Physical Chemistry,* vol. 49, pp. 569-638, 1998.

[3] H.Raether, *Surface plasmons on smooth and rough surfaces and on gratings*. New York: Springer-Verlag, 1986.

[4] J. Homola, *Surface Plasmon Resonance Based Sensors*. New York: Springer, 2006.

[5] A. Otto, "EXCITATION OF NONRADIATIVE SURFACE PLASMA WAVES IN SILVER BY METHOD OF FRUSTRATED TOTAL REFLECTION," *Zeitschrift Fur Physik,* vol. 216, pp. 398-&, 1968.

[6] E.Kretchmann, "Die Bestimmung optischer Kon- stanten von Metallen durch Anregung von Oberfl chenplasmaschwingugnen," *Z Phys.*, vol. 241, pp. 313-324, 1971.

[7] R. J. Green, *et al.*, "Surface plasmon resonance analysis of dynamic biological interactions with biomaterials," *Biomaterials,* vol. 21, pp. 1823-1835, 2000.

[8] A.D.Boardman, *Electromagnetic Surface Modes*: John Wiley & Sons, 1982.

[9] J. Homola, "Present and future of surface plasmon resonance biosensors," *Analytical and Bioanalytical Chemistry,* vol. 377, pp. 528-539, Oct 2003.

[10] C. E. Jordan, *et al.*, "CHARACTERIZATION OF POLY-L-LYSINE ADSORPTION ONTO ALKANETHIOL-MODIFIED GOLD SURFACES WITH POLARIZATION-MODULATION FOURIER-TRANSFORM INFRARED-SPECTROSCOPY AND SURFACE-PLASMON RESONANCE MEASUREMENTS," *Langmuir,* vol. 10, pp. 3642-3648, 1994.

[11] H. Sota, *et al.*, "Detection of conformational changes in an immobilized protein using surface plasmon resonance," *Analytical Chemistry,* vol. 70, pp. 2019-2024, 1998.

[12] S. M. Barbas, *et al.*, "HUMAN AUTOANTIBODY RECOGNITION OF DNA," *Proceedings of the National Academy of Sciences of the United States of America,* vol. 92, pp. 2529-2533, 1995.

[13] J.F.Rusling, *Biomolecular films, Design, Function, and Applications* vol. 111. New York: Marcel Dekker, Inc, 2003.

[14] H. J. Lee, *et al.*, "SPR imaging measurements of 1-D and 2-D DNA microarrays created from microfluidic channels on gold thin films," *Analytical Chemistry,* vol. 73, pp. 5525-5531, Nov 2001.

[15] G. J. Wegner, *et al.*, "Real-time surface plasmon resonance imaging measurements for the multiplexed determination of protein adsorption/desorption kinetics and surface enzymatic reactions on peptide microarrays," *Analytical Chemistry,* vol. 76, pp. 5677-5684, Oct 2004.

[16] D. G. Hanken and R. M. Corn, "Electric fields and interference effects inside noncentrosymmetric multilayer films at electrode surfaces from electrochemically modulated surface plasmon resonance experiments," *Analytical Chemistry,* vol. 69, pp. 3665-3673, Sep 1997.

[17] Y. Iwasaki, *et al.*, "Electrochemical reaction of Fe (CN)(6)(3-)/(4-) on gold electrodes analyzed by surface plasmon resonance," *Surface Science,* vol. 428, pp. 195-198, Jun 1 1999.

[18] S. P. Wang, *et al.*, "Detection of heavy metal ions in water by high-resolution surface plasmon resonance spectroscopy combined with anodic stripping voltammetry," *Analytical Chemistry,* vol. 79, pp. 4427-4432, Jun 15 2007.

[19] S. Wang, *et al.*, "Surface plasmon resonance enhanced optical absorption spectroscopy for studying molecular adsorbates," *Review of Scientific Instruments,* vol. 72, pp. 3055-3060, Jul 2001.

[20] S. Wang, *et al.*, "High sensitivity stark spectroscopy obtained by surface plasmon resonance measurement," *Analytical Chemistry,* vol. 72, pp. 4003-4008, Sep 2000.

[21] S. Boussaad, *et al.*, "High-resolution multiwavelength surface plasmon resonance spectroscopy for probing conformational and electronic changes in redox proteins," *Analytical Chemistry,* vol. 72, pp. 222-226, Jan 1 2000.

[22] X. F. Kang, *et al.*, "A novel electrochemical SPR biosensor," *Electrochemistry Communications,* vol. 3, pp. 489-493, Sep 2001.

[23] J. L. Wang, *et al.*, "Electrochemical surface plasmon resonance detection of enzymatic reaction in bilayer lipid," *Talanta*, vol. 75, pp. 666-670, May 15 2008.

[24] R. Schweiss, *et al.*, "Electropolymerization of ethylene dioxythiophene (EDOT) in micellar aqueous solutions studied by electrochemical quartz crystal microbalance and surface plasmon resonance," *Electrochimica Acta*, vol. 50, pp. 2849-2856, May 5 2005.

[25] S. Kienle, *et al.*, "Electropolymerization of a phenol-modified peptide for use in receptor-ligand interactions studied by surface plasmon resonance," *Biosensors & Bioelectronics*, vol. 12, pp. 779-786, 1997.

[26] http://en.wikipedia.org/wiki/Fick%27s_law_of_diffusion.

[27] A. J. Bard and L. R. Faulkner, *Electrochemical methods : fundamentals and applications*, 2nd ed. New York: Wiley, 2001.

[28] J. C. Imbeaux and J. M. Saveant, "CONVOLUTIVE POTENTIAL SWEEP VOLTAMMETRY .1. INTRODUCTION," *Journal of Electroanalytical Chemistry*, vol. 44, pp. 169-187, 1973.

[29] http://www.waterworld.com/index/display/article-display/357438/articles/water-wastewater-international/volume-24/issue-1/features/korea-explores-sludge-amp-odor-control-alternatives.html.

[30] S. Wang, *et al.*, "High sensitivity stark spectroscopy obtained by surface plasmon resonance measurement," *Analytical Chemistry*, vol. 72, pp. 4003-4008, Sep 2000.

[31] R. Orlowski and H. Raether, "Total Reflection of Light at Smooth and Rough Silver Films and Surface Plasmons," *Surface Science*, vol. 54, pp. 303-308, 1976.

[32] A. J. Bard and L. R. Faulkner, *Electrochemical Methods*, 2nd ed. New York: Wiley, 2001.

[33] A. J. Bard, *et al.*, "Chemical imaging of surfaces with the scanning electrochemical microscope," *Science*, vol. 254, pp. 68-74, 1991.

[34] S. Amemiya, *et al.*, "Scanning Electrochemical Microscopy," *Annu. Rev. Anal. Chem.*, vol. 1, pp. 95-131, 2008.

[35] B. Rothenhausler and W. Knoll, "Surface-Plasmon Microscopy," *Nature*, vol. 332, pp. 615-617, 1988.

[36] J. M. Brockman, *et al.*, "Surface plasmon resonance imaging measurements of ultrathin organic films," *Annu. Rev. Phys. Chem.*, vol. 51, pp. 41-63, 2000.

[37] Q. G. Li and H. S. White, "Interferometric Measurement of Depletion Layer Structure and Voltammetric Data in Concentrated Organic Redox Solutions," *Anal. Chem.*, vol. 67, pp. 561–569, 1995.

[38] G. Flatgen, *et al.*, "Dimensional imaging of potential waves in electrochemical systems by surface-plasmon miscroscopy," *Science*, vol. 269, pp. 668-671, 1995

[39] O. Andersson, *et al.*, "Imaging SPR for detection of local electrochemical processes on patterned surfaces," *Sensors and Actuators B-Chemical*, vol. 134, pp. 545-550, 2008.

[40] A. J. Bard and L. R. Faulkner, *Electrochemical Methods*. New York: John Wiley and Sons, Inc., 1980.

[41] X. N. Shan, *et al.*, "Imaging Local Electrochemical Current via Surface Plasmon Resonance," *Science*, vol. 327, pp. 1363-1366, Mar 2010.

[42] D. G. Hanken, *et al.*, "Surface plasmon resonance measurements of ultrathin organic films at electrode surfaces," *Electroanal. Chem.*, vol. 20, pp. 141-225, 1998.

[43] K. J. Foley, *et al.*, "Surface impedance imaging technique," *Anal. Chem.*, vol. 80, pp. 5146-5151, 2008.

[44] B. Huang, *et al.*, "Surface plasmon resonance imaging using a high numerical aperture microscope objective," *Analytical Chemistry*, vol. 79, pp. 2979-2983, 2007.

[45] M. Zhang and H. H. Girault, "SECM for imaging and detection of latent fingerprints," *Analyst*, vol. 134, pp. 25-30, 2009.

[46] L. A. Pinnaduwage, *et al.*, "A microsensor for trinitrotoluene vapour," *Nature*, vol. 425, pp. 474-474, 2003.

[47] J. Wang, "Electrochemical sensing of explosives," *Electroanalysis*, vol. 19, pp. 415-423, 2007.

[48] H. X. Zhang, *et al.*, "Electrochemical sensor for detecting ultratrace nitroaromatic compounds using mesoporous SiO2-modified electrode," *Anal. Chem.*, vol. 78, pp. 1967-1971, 2006.

[49] N. L. Abbott, *et al.*, "Manipulation of the wettability of surfaces on the 0.1- to 1-micrometer scale through micromachining and molecular self-assembly," *Science*, vol. 257, pp. 1380-1382, 1992.

[50] A. K. Geim and K. S. Novoselov, "The rise of graphene," *Nature Materials*, vol. 6, pp. 183-191, Mar 2007.

[51] K. S. Novoselov, *et al.*, "Electric field effect in atomically thin carbon films," *Science*, vol. 306, pp. 666-669, Oct 2004.

[52] R. R. Nair, *et al.*, "Fine structure constant defines visual transparency of graphene," *Science*, vol. 320, pp. 1308-1308, 2008.

[53] J. S. Bunch, *et al.*, "Electromechanical resonators from graphene sheets," *Science*, vol. 315, pp. 490-493, Jan 2007.

[54] A. P. Yu, *et al.*, "Graphite nanoplatelet-epoxy composite thermal interface materials," *Journal of Physical Chemistry C*, vol. 111, pp. 7565-7569, May 2007.

[55] M. D. Stoller, *et al.*, "Graphene-Based Ultracapacitors," *Nano Letters*, vol. 8, pp. 3498-3502, Oct 2008.

[56] A. K. Geim, "Graphene: Status and Prospects," *Science*, vol. 324, pp. 1530-1534, Jun 2009.

[57] A. H. Castro Neto, *et al.*, "The electronic properties of graphene," *Reviews of Modern Physics*, vol. 81, pp. 109-162, 2009.

[58] K. S. Novoselov, *et al.*, "Two-dimensional gas of massless Dirac fermions in graphene," *Nature*, vol. 438, pp. 197-200, 2005.

[59] Y. Zhang, *et al.*, "Experimental observation of the quantum Hall effect and Berry's phase in graphene," *Nature*, vol. 438, pp. 201-204, 2005.

[60] M. I. Katsnelson, *et al.*, "Chiral tunnelling and the Klein paradox in graphene," *Nature Physics*, vol. 2, pp. 620-625, 2006.

[61] D. A. C. Brownson and C. E. Banks, "Graphene electrochemistry: an overview of potential applications," *Analyst*, vol. 135, pp. 2768-2778, 2010.

[62] X. H. Kang, *et al.*, "Glucose Oxidase-graphene-chitosan modified electrode for direct electrochemistry and glucose sensing," *Biosensors & Bioelectronics,* vol. 25, pp. 901-905, 2009.

[63] Y. R. Kim, *et al.*, "Electrochemical detection of dopamine in the presence of ascorbic acid using graphene modified electrodes," *Biosensors & Bioelectronics,* vol. 25, pp. 2366-2369, 2010.

[64] Z. Y. Zhong, *et al.*, "Nanogold-enwrapped graphene nanocomposites as trace labels for sensitivity enhancement of electrochemical immunosensors in clinical immunoassays: Carcinoembryonic antigen as a model," *Biosensors & Bioelectronics,* vol. 25, pp. 2379-2383, 2010.

[65] X. H. Kang, *et al.*, "A graphene-based electrochemical sensor for sensitive detection of paracetamol," *Talanta,* vol. 81, pp. 754-759, May 2010.

[66] Y. Y. Shao, *et al.*, "Graphene Based Electrochemical Sensors and Biosensors: A Review," *Electroanalysis,* vol. 22, pp. 1027-1036, 2010.

[67] C. E. Banks, *et al.*, "Electrocatalysis at graphite and carbon nanotube modified electrodes: edge-plane sites and tube ends are the reactive sites," *Chemical Communications,* pp. 829-841, 2005.

[68] C. E. Banks and R. G. Compton, "Edge plane pyrolytic graphite electrodes in electroanalysis: An overview," *Analytical Sciences,* vol. 21, pp. 1263-1268, 2005.

[69] T. J. Davies, *et al.*, "Nanotrench arrays reveal insight into graphite electrochemistry," *Angewandte Chemie-International Edition,* vol. 44, pp. 5121-5126, 2005.

[70] R. J. Rice, *et al.*, "QUANTITATIVE CORRELATIONS OF HETEROGENEOUS ELECTRON-TRANSFER KINETICS WITH SURFACE-PROPERTIES OF GLASSY-CARBON ELECTRODES," *Journal of the American Chemical Society,* vol. 112, pp. 4617-4622, 1990.

[71] Y. Liu and M. S. Freund, "Influence of organic solvents on the kinetics of electron transfer and the adsorption at highly oriented pyrolytic graphite," *Langmuir,* vol. 16, pp. 283-286, 2000.

[72] Z. H. Ni, *et al.*, "Graphene thickness determination using reflection and contrast spectroscopy," *Nano Letters,* vol. 7, pp. 2758-2763, 2007.

[73] P. Blake, *et al.*, "Making graphene visible," *Applied Physics Letters,* vol. 91, 2007.

[74] A. C. Ferrari, *et al.*, "Raman Spectrum of Graphene and Graphene Layers," *Physical Review Letters,* vol. 97, 2006.

[75] K. S. Novoselov, *et al.*, "Two-dimensional atomic crystals," *Proceedings of the National Academy of Sciences of the United States of America,* vol. 102, pp. 10451-10453, 2005.

[76] P. Lauffer, *et al.*, "Atomic and electronic structure of few-layer graphene on SiC(0001) studied with scanning tunneling microscopy and spectroscopy," *Physical Review B,* vol. 77, 2008.

[77] Y. Hernandez, *et al.*, "High-yield production of graphene by liquid-phase exfoliation of graphite," *Nature Nanotechnology,* vol. 3, pp. 563-568, 2008.

[78] J. L. Fernandez, *et al.*, "Thermodynamic guidelines for the design of bimetallic catalysts for oxygen electroreduction and rapid screening by scanning electrochemical microscopy. M-Co (M : Pd, Ag, Au)," *Journal of the American Chemical Society,* vol. 127, pp. 357-365, Jan 2005.

[79] C. M. Sanchez-Sanchez, *et al.*, "Imaging Structure Sensitive Catalysis on Different Shape-Controlled Platinum Nanoparticles," *Journal of the American Chemical Society,* vol. 132, pp. 5622-+, Apr 2010.

[80] L. Mellander, *et al.*, "Electrochemical Probes for Detection and Analysis of Exocytosis and Vesicles," *Chemphyschem,* vol. 11, pp. 2756-2763, Sep 2010.

[81] M. Fojta, "Electrochemical sensors for DNA interactions and damage," *Electroanalysis,* vol. 14, pp. 1449-1463, Nov 2002.

[82] S. Amemiya, *et al.*, "Scanning Electrochemical Microscopy," *Annual Review of Analytical Chemistry,* vol. 1, pp. 95-131, 2008.

[83] A. Schulte, *et al.*, "Scanning Electrochemical Microscopy in Neuroscience," *Annual Review of Analytical Chemistry,* vol. 3, pp. 299-318, 2010.

[84] R. Wen, *et al.*, "A New in Situ Optical Microscope with Single Atomic Layer Resolution for Observation of Electrochemical Dissolution of Au(111)," *J. Am. Chem. Soc.*, vol. 132, pp. 13657-13659, 2010.

[85] X. N. Shan, *et al.*, "Imaging Local Electrochemical Current via Surface Plasmon Resonance," *Science*, vol. 327, pp. 1363-1366, Mar 2010.

[86] L. M. Fu and C. H. Lin, "High-resolution DNA separation in microcapillary electrophoresis chips utilizing double-L injection techniques," *Electrophoresis*, vol. 25, pp. 3652-3659, Nov 2004.

[87] J. Wang and S. Thongngamdee, "On-line electrochemical monitoring of (TNT) 2,4,6-trinitrotoluene in natural waters," *Analytica Chimica Acta*, vol. 485, pp. 139-144, Jun 2003.

[88] J. de Sanoit, *et al.*, "Electrochemical diamond sensors for TNT detection in water," *Electrochimica Acta*, vol. 54, pp. 5688-5693, Oct 2009.

[89] R. Naumann, *et al.*, "The peptide-tethered lipid membrane as a biomimetic system to incorporate cytochrome c oxidase in a functionally active form," *Biosensors & Bioelectronics*, vol. 14, pp. 651-662, Oct 1999.

[90] K. J. Foley, *et al.*, "Surface impedance imaging technique," *Analytical Chemistry*, vol. 80, pp. 5146-5151, Jul 2008.

[91] W. Wang, *et al.*, "Single cells and intracellular processes studied by a plasmonic-based electrochemical impedance microscopy," *Nature Chemistry*, vol. 3, pp. 249-255, Mar 2011.

[92] S. P. Wang, *et al.*, "Electrochemical Surface Plasmon Resonance: Basic Formalism and Experimental Validation," *Analytical Chemistry*, vol. 82, pp. 935-941, Feb 2010.

[93] E. Kretschmann, "Determination of Optical Constants of Metals by Excitation of Surface Plasmons," *Zeitschrift Fur Physik*, vol. 241, pp. 313-324, 1971.

[94] T. Deng, *et al.*, "Prototyping of Masks, Masters, and Stamps/Molds for Soft Lithography Using an Office Printer and Photographic Reduction," *Analytical Chemistry*, vol. 72, pp. 3176-3180, 2000.

[95] N. Tian, *et al.*, "Synthesis of Tetrahexahedral Platinum Nanocrystals with High-Index Facets and High Electro-Oxidation Activity," *Science*, vol. 316, pp. 732-735, 2007.

[96] M. E. Stewart, *et al.*, "Nanostructured plasmonic sensors," *Chemical Reviews*, vol. 108, pp. 494-521, Feb 2008.

[97] A. D. McFarland and R. P. Van Duyne, "Single silver nanoparticles as real-time optical sensors with zeptomole sensitivity," *Nano Letters,* vol. 3, pp. 1057-1062, Aug 2003.

[98] P. Strasser, *et al.*, "Lattice-strain control of the activity in dealloyed core-shell fuel cell catalysts," *Nature Chemistry,* vol. 2, pp. 454-460, Jun 2010.

[99] K. A. Willets and R. P. Van Duyne, "Localized surface plasmon resonance spectroscopy and sensing," *Annual Review of Physical Chemistry,* vol. 58, pp. 267-297, 2007.

[100] X. M. Qian, *et al.*, "In vivo tumor targeting and spectroscopic detection with surface-enhanced Raman nanoparticle tags," *Nature Biotechnology,* vol. 26, pp. 83-90, Jan 2008.

[101] J. T. Zhang, *et al.*, "Tailoring light-matter-spin interactions in colloidal hetero-nanostructures," *Nature,* vol. 466, pp. 91-95, Jul 2010.

[102] A. Z. Moshfegh, "Nanoparticle catalysts," *Journal of Physics D-Applied Physics,* vol. 42, Dec 2009.

[103] C. M. Sanchez-Sanchez and A. J. Bard, "Hydrogen Peroxide Production in the Oxygen Reduction Reaction at Different Electrocatalysts as Quantified by Scanning Electrochemical Microscopy," *Analytical Chemistry,* vol. 81, pp. 8094-8100, Oct 2009.

[104] M. H. Huang, *et al.*, "Alternate assemblies of platinum nanoparticles and Metalloporphyrins as tunable electrocatalysts for dioxygen reduction," *Langmuir,* vol. 21, pp. 323-329, Jan 2005.

[105] R. J. Heaton, *et al.*, "Electrostatic surface plasmon resonance: Direct electric field-induced hybridization and denaturation in monolayer nucleic acid films and label-free discrimination of base mismatches," *Proceedings of the National Academy of Sciences of the United States of America,* vol. 98, pp. 3701-3704, 2001.

[106] N. G. Clack, *et al.*, "Electrostatic readout of DNA microarrays with charged microspheres," *Nature Biotechnology,* vol. 26, pp. 825-830, Jul 2008.

[107] J. Sanchez and M. del Valle, "Determination of anionic surfactants employing potentiometric sensors - A review," *Critical Reviews in Analytical Chemistry,* vol. 35, pp. 15-29, 2005.

[108] G. T. T. Gibson, *et al.*, "Potentiometric titration of metal ions in ethanol," *Inorganic Chemistry,* vol. 45, pp. 7891-7902, 2006.

[109] S. H. Xu and M. F. Arnsdorf, "Electrostatic Force Microscope for Probing Surface-Charges in Aqueous-Solutions," *Proceedings of the National Academy of Sciences of the United States of America,* vol. 92, pp. 10384-10388, 1995.

[110] S. D. Campbell and A. C. Hillier, "Nanometer-scale probing of potential-dependent electrostatic forces, adhesion, and interfacial friction at the electrode/electrolyte interface," *Langmuir,* vol. 15, pp. 891-899, 1999.

[111] A. K. Sinensky and A. M. Belcher, "Label-free and high-resolution protein/DNA nanoarray analysis using Kelvin probe force microscopy," *Nature Nanotechnology,* vol. 2, pp. 653-659, 2007.

[112] H. J. Butt, *et al.*, "Force measurements with the atomic force microscope: Technique, interpretation and applications," *Surface Science Reports,* vol. 59, pp. 1-152, 2005.

[113] N. G. Clack and J. T. Groves, "Many-particle tracking with nanometer resolution in three dimensions by reflection interference contrast microscopy," *Langmuir,* vol. 21, pp. 6430-6435, 2005.

[114] C. E. H. Berger, *et al.*, "Resolution in Surface-Plasmon Microscopy," *Review of Scientific Instruments,* vol. 65, pp. 2829-2836, Sep 1994.

[115] X. D. Hoa, *et al.*, "Towards integrated and sensitive surface plasmon resonance biosensors: A review of recent progress," *Biosensors & Bioelectronics,* vol. 23, pp. 151-160, 2007.

[116] H. J. Wu, *et al.*, "Measurement and interpretation of particle-particle and particle-wall interactions in levitated colloidal ensembles," *Langmuir,* vol. 21, pp. 9879-9888, 2005.

[117] H. J. Wu and M. A. Bevan, "Direct measurement of single and ensemble average particle-surface potential energy profiles," *Langmuir,* vol. 21, pp. 1244-1254, 2005.

[118] N. A. Frej and D. C. Prieve, "Hindered Diffusion of a Single Sphere Very near a Wall in a Nonuniform Force-Field," *Journal of Chemical Physics,* vol. 98, pp. 7552-7564, 1993.

[119] J. P. Hsu and B. T. Liu, "Electrical interaction energy between two charged entities," *Journal of Chemical Physics,* vol. 110, pp. 25-33, 1999.

[120] Y. Liang, *et al.*, "Interaction forces between colloidal particles in liquid: Theory and experiment," *Advances in Colloid and Interface Science,* vol. 134-35, pp. 151-166, 2007.

[121] S. H. Behrens and D. G. Grier, "The charge of glass and silica surfaces," *Journal of Chemical Physics,* vol. 115, pp. 6716-6721, 2001.

[122] X. N. Shan, *et al.*, "A label-free optical detection method for biosensors and microfluidics," *Applied Physics Letters,* vol. 92, 2008.

[123] W. N. Hansen, "Electric Fields Produced by Propagation of Plane Coherent Electromagnetic Radiation in a Stratified Medium," *Journal of the Optical Society of America,* vol. 58, pp. 380-390, 1968.

[124] J. N. Israelachvili, *Intermolecular and Surface Forces*, 2nd ed. London: Academic Press, 1991.

[125] P. M. Dove and C. M. Craven, "Surface charge density on silica in alkali and alkaline earth chloride electrolyte solutions," *Geochimica Et Cosmochimica Acta,* vol. 69, pp. 4963-4970, 2005.

[126] K. P. Fears, *et al.*, "Determination of the surface pK of carboxylic- and amine-terminated alkanethiols using surface plasmon resonance spectroscopy," *Langmuir,* vol. 24, pp. 837-843, 2008.

[127] J. W. Zhao, *et al.*, "Determination of surface pK(a) of SAM using an electrochemical titration method," *Electroanalysis,* vol. 11, pp. 1108-1111, Nov 1999.

[128] K. Kim and J. Kwak, "Faradaic impedance titration of pure 3-mercaptopropionic acid and ethanethiol mixed monolayers on gold," *Journal of Electroanalytical Chemistry,* vol. 512, pp. 83-91, Oct 2001.

[129] J. N. Israelachvili, *Intermolecular and Surface Forces*. London: Academic Press, 1991.

[130] S. R. Ian D. Morrison, *Colloidal Dispersions: Suspensions, Emulsions, and Foams* Yew York: John Wiley and Sons, 2002.

[131] S. P. Radko and A. Chrambach, "Separation and characterization of sub-mu m- and mu m-sized particles by capillary zone electrophoresis," *Electrophoresis,* vol. 23, pp. 1957-1972, Jul 2002.

[132] P. H. Wiersema, *et al.*, "CALCULATION OF ELECTROPHORETIC MOBILITY OF A SPHERICAL COLLOID PARTICLE," *Journal of Colloid and Interface Science,* vol. 22, pp. 78-&, 1966.

[133] X. N. Shan, *et al.*, "Measuring Surface Charge Density and Particle Height Using Surface Plasmon Resonance Technique " *Anal. Chem.,* vol. 82, pp. 234-240 2010.

[134] X. N. Shan, *et al.*, "Imaging Local Electrochemical Current via Surface Plasmon Resonance," *Science*, vol. 327, pp. 1363-1366, 2010.

[135] S. Wang, *et al.*, "Label-free imaging, detection, and mass measurement of single viruses by surface plasmon resonance," *Proc Natl Acad Sci U S A,* vol. 107, pp. 16028-32, Sep 14 2010.

[136] H. Bruus, *Theoretical Microfluidics*. New York: Oxford university press, 2008.

[137] A. Sze, *et al.*, "Zeta-potential measurement using the Smoluchowski equation and the slope of the current-time relationship in electroosmotic flow," *Journal of Colloid and Interface Science,* vol. 261, pp. 402-410, May 2003.

[138] D. J. Beebe, *et al.*, "Physics and applications of microfluidics in biology," *Annual Review of Biomedical Engineering,* vol. 4, pp. 261-286, 2002.

[139] E. Verpoorte, "Microfluidic chips for clinical and forensic analysis," *Electrophoresis,* vol. 23, pp. 677-712, Mar 2002.

[140] T. Chovan and A. Guttman, "Microfabricated devices in biotechnology and biochemical processing," *Trends in Biotechnology,* vol. 20, pp. 116-122, Mar 2002.

[141] M. A. Cooper, "Label-free screening of bio-molecular interactions," *Analytical and Bioanalytical Chemistry,* vol. 377, pp. 834-842, Nov 2003.

[142] N. Ly, *et al.*, "Integrated label-free protein detection and separation in real time using confined surface plasmon resonance imaging," *Analytical Chemistry,* vol. 79, pp. 2546-2551, Mar 2007.

[143] M. S. Meyer and G. L. Eesley, "OPTICAL FIBER REFRACTOMETER," *Review of Scientific Instruments,* vol. 58, pp. 2047-2048, Nov 1987.

[144] C. T. Campbell and G. Kim, "SPR microscopy and its applications to high-throughput analyses of biomolecular binding events and their kinetics," *Biomaterials,* vol. 28, pp. 2380-2392, May 2007.